



Politecnico  
di Bari

Repository Istituzionale dei Prodotti della Ricerca del Politecnico di Bari

On the Electrical Aging of the Insulation in PWM-Fed High-Speed Electric Machines: Analysis, Modelling, and Mitigation

This is a PhD Thesis

*Original Citation:*

*Availability:*

This version is available at <http://hdl.handle.net/11589/190884> since: 2020-02-18

*Published version*

<http://hdl.handle.net/11589/190884>  
DOI: 10.6057/poliba/iris/leuzzi-riccardo\_phd2020

*Terms of use:*

Altro tipo di accesso

(Article begins on next page)



Department of Electrical and Information Engineering  
ELECTRICAL AND INFORMATION ENGINEERING  
Ph.D. Program  
SSD: ING-IND/32– POWER ELECTRONIC CONVERTERS,  
ELECTRICAL MACHINES AND DRIVES  
**Final Dissertation**

---

# On the Electrical Aging of the Insulation in PWM-Fed High-Speed Electric Machines: Analysis, Modelling, and Mitigation

---

by  
Leuzzi Riccardo

Supervisors:

Prof. Francesco Cupertino

*Coordinator of Ph.D. Program:*  
*Prof. Alfredo Grieco*

---

*Course n°32, 01/11/2016-31/10/2019*



Department of Electrical and Information Engineering  
ELECTRICAL AND INFORMATION ENGINEERING  
Ph.D. Program  
SSD: ING-IND/32– POWER ELECTRONIC CONVERTERS,  
ELECTRICAL MACHINES AND DRIVES  
**Final Dissertation**

---

# On the Electrical Aging of the Insulation in PWM-Fed High-Speed Electric Machines: Analysis, Modelling, and Mitigation

---

by  
Leuzzi Riccardo

---

Referees:

Prof. Davide Barater

Prof. Alfonso Damiano

Supervisors:

Prof. Francesco Cupertino

---

*Coordinator of Ph.D. Program:*

*Prof. Alfredo Grieco*

---

*Course n°32, 01/11/2016-31/10/2019*



## Abstract

This doctoral thesis represents the completion of a three-year research activity that has been carried out as part of the Ph.D. program in Electrical and Information Engineering, XXXII cycle, of the Polytechnic University of Bari, Italy. The work that is presented in this document addresses some specific aspects of the broader topic of reliability in high-frequency electric drives, that is the early failure of inverter-fed AC machine insulation systems due to the very high  $dv/dt$ 's of modern fast switching converters. A selection of the most important research works that have been published in the literature on this subject is reviewed here and can be found in the reference. These works have greatly contributed to the progression of the research and thesis. Hopefully, the content presented in this document will also add a modest contribution to this topic that is becoming more and more relevant in today electric drive applications.

The background of the thesis, the motivations and ideas laying behind the research activity carried on the topic of insulation aging are presented. The role of electrification in many application areas and the benefits that the transition to cleaner energy forms can bring to the cause of environment and climate preservation are discussed. In this promising energy transition process, high-speed machines and high-frequency power electronics converters are key technologies to enable enormous energy saving and to boost the penetration of more electrical systems in both industry and transportation sectors. The growing market diffusion of high-frequency electric drives is driven by the fast developments in the new generation of power switching devices, which are based on silicon carbide and gallium nitride composites, the so-called wide bandgap semiconductor materials. Thanks to these new materials, which present better properties than silicon with respect to breakdown electric field, electron mobility, and thermal stability, modern power switches can operate at higher commutation frequency, with lower losses and higher junction temperature than previous generations. Alongside with the numerous advantages of high-frequency devices, new issues arise for their practical implementation because of their fast commutation transients at turn-on and turn-off. In fact, the very short rise and fall time of the applied voltage pulses, in the order of tens of nanoseconds, is source of increased electromagnetic interference that can negatively affect the surrounding low-power electronics, common-mode voltage can appear across the shaft of the machine leading to the circulation of currents along the bearings and subsequent mechanical deterioration, and increased stress on the motor turn insulation. The higher electrical stress on the insulation is the cause of partial discharges within the weak spots of the system, small sparks that delaminate the dielectric material, eventually leading to a turn short circuit and to the fault.

The winding insulation system is a fundamental component of any electric machine, functionally required for the operation of the electro-mechanical conversion mechanism. The

breakdown of the insulation inhibits the operation of the machine, which must be re-wound to be put in service again. Due to the high  $dv/dt$ 's in high-frequency power electronic converters, two phenomena occur that can threaten the life duration of motor insulation systems. Voltage waveform reflections along the cable that connects the inverter and the machine produce high overvoltage at the motor terminals when the rise time of the PWM voltage pulses is short. Furthermore, due to the parasitic capacitances of the winding insulation, the distribution of the voltage across the coil is such that, when the pulses are applied to the winding, the first turns are exposed to the higher share of the voltage. Consequently, within the defects of the insulation system, such as air pockets or small clearances, partial discharges are triggered by the electric field exceeding the dielectric strength of the air. Partial discharges are ionic discharge events that modify the physical and chemical properties of the material, making it weaker over time until it cannot sustain the normal field anymore. At this point, the irreversible fault occurs, and the machine must be put out of service. Many studies in the literature have investigated the role of partial discharge on shortening the life of winding insulation systems, and the main effects of PWM voltages on the partial discharge characteristics have been identified.

The main approaches commonly adopted today for the mitigation of the electrical stress on the insulation are the use of inverter output filters, very effective but generally bulky and costly and that often reduce the dynamic performance of the drive, and the combined design of converter and machine to minimize the length of the cables, which has practical limitations in high-speed drives due to the different scaling of the two parts.

There are three main goals of the research activity presented in this doctoral thesis. The first objective is to achieve a better understanding of the effects of electrical aging on motor insulation, to develop a practical method for the estimation of the aging progression through the measure of electrical quantities such as voltage and current. The second goal is the development of accurate and easy-to-tune model of the drive components in the high-frequency domain, to be used for both improving the drive design and performing advanced diagnosis features. The third objective is to investigate possible approaches for the mitigation of the electrical aging in high-speed electrical machines. Two possibilities are taken into consideration to this purpose: the active regulation of the  $dv/dt$  to limit the overvoltage at the motor terminals, and the use of multilevel converters to reduce the voltage stress by increasing the number of voltage levels.

To achieve a deep understanding of the aging phenomenon from a macroscopic point of view, i.e. by mean of easily measurable electrical quantities, a series of electrical aging test have been performed on a group of motors while their characteristics were cyclically measured. The data collected during this aging campaign, together with the experimental setup that has been developed, are presented in the thesis. The data are statistically used to build some indicators of the insulation condition that can be used as an estimation of the aging progression in the

insulation system. The first indicator is obtained through the measure of the machine characteristic impedances at different aging steps, while the second and the third are calculated from the high-frequency response of the phase current when a voltage pulse is applied.

Accurate models of the electric drive system in the high-frequency domain are required to both improve designs from a system point of view and to include advanced predictive diagnosis features in the drive control system. A series of high-frequency motor models are reviewed and analysed in this thesis based on the findings from the electrical aging campaign performed. A first modelling approach is made using a lumped-parameter model of the machine and an automatic identification procedure. To improve both accuracy and model tuning time, a second model is proposed, which is based on the automatic identification of an analytical rational function with the measured data. The fitting algorithm that has been employed is described in the thesis, and results are shown about the achieved accuracy level.

The experimental data collected during the electrical aging tests and the developed high-frequency models of the drive components are used to investigate some possible approaches for the mitigation of the electrical stress on the winding insulation system of electric machines. The first method that is considered is the idea of using the estimation of the winding insulation aging conditions as a feedback for an advance control system for the active regulation of the  $dv/dt$  of the PWM pulses to the purpose of extending the life of the drive while optimizing efficiency and performance. Such a system requires different parts to properly function, an effective estimator, a controller based on an optimization algorithm, and a set of active gate drivers. In this thesis, the idea is explored by simulation with some simplifications. The second overvoltage mitigation approach is to have a multilevel voltage waveform applied to the motor instead of a train of PWM pulses. In this way, the level of the overvoltage applied to the motor is reduced, and so is the electrical stress on the insulation. To this purpose, in this thesis a cascaded H-bridge multilevel converter is compared to a conventional 2-level inverter operating on the same load conditions and with the same overvoltage level at the motor terminals. A simulation model is used to compare the losses, the efficiency, and the thermal requirements in both cases.

*A mia madre.*



«"Forty-two!" yelled Loonquawl. "Is that all you've got to show for seven and a half million years' work?"  
"I checked it very thoroughly," said the computer, "and that quite definitely is the answer. I think the  
problem, to be quite honest with you, is that you've never actually known what the question is."»

– Douglas Adams, *The Hitchhiker's Guide to the Galaxy*

## Ringraziamenti

Per prima cosa, desidero profondamente ringraziare il Prof. Francesco Cupertino per avermi offerto la possibilità di intraprendere e completare il mio percorso di Dottorato, per aver sostenuto le mie idee e per avermi dato l'opportunità di accrescere la mia formazione nell'ambito della ricerca universitaria, sia nei laboratori del Politecnico di Bari che in centri riconosciuti all'estero.

Un sincero ringraziamento va inoltre al Prof. Vito Monopoli e a Rinaldo Consoletti, i consigli dei quali, di natura tecnica e non solo, mi sono sempre stati d'aiuto durante tutti gli anni di Dottorato.

Desidero sentitamente ringraziare anche il Prof. Pericle Zanchetta, il quale mi ha accolto e consigliato durante tutto il mio soggiorno presso la University of Nottingham, permettendomi di portare avanti le mie idee di ricerca e offrendomi numerose occasioni di apprendimento.

Voglio inoltre dire grazie alla mia famiglia, mio padre Vincenzo e mio fratello Gianluca per esserci sempre stati.

Infine, non esistono parole per quantificare il supporto che ho sempre ricevuto, e che tutt'ora ricevo, da parte della mia ragazza, Monica. A lei devo il coraggio e la forza che mi hanno permesso di arrivare alla fine di questo percorso.

# Table of Contents

Abstract .....	ii
Ringraziamenti.....	vii
Table of Contents .....	viii
List of Figures .....	xi
List of Tables .....	xvi
Chapter 1 Introduction.....	1
1.1. Background and Significance of the Topic .....	1
1.1.1. The European environmental action .....	1
1.1.2. The role of electric drives in the industry and transportations sectors .....	2
1.1.3. Increasing the frequency: current trends and practical challenges .....	6
1.2. Motivation and Goals.....	11
1.3. Structure of the Thesis.....	11
1.4. List of Scientific Publications .....	12
1.4.1. Journals: .....	12
1.1.1. Conference proceedings:.....	13
Chapter 2 An Overview.....	14
2.1. Electrical Insulation Systems in AC Rotating Machines .....	14
2.1.1. Types of stator winding construction.....	14
2.1.2. Composition of stator winding insulation systems.....	16
2.2. Phenomenology of Insulation Aging and Failure in PWM-fed AC Drives .....	19
2.2.1. Reflection of voltage waveforms across long cables.....	20
2.2.2. Uneven distribution of the voltage along the coil.....	25
2.2.3. Partial discharges, insulation aging and failure mechanisms.....	27
2.2.4. Effect of PWM characteristics on the properties of partial discharges .....	34
2.3. Common Approaches to Prevent Insulation Aging.....	40
2.3.1. Inverter output filters.....	41
2.3.2. Co-design of power electronics and motor .....	43
2.3.3. Corona-resistant materials.....	44

Chapter 3	Study on the Effects of Electrical Aging on Winding Insulation and Its Estimation	45
3.1.	Description of the Experimental Setup for the Accelerated Aging Test.....	46
3.2.	Methodologies for the Estimation of Aging Effects.....	49
3.2.1.	Estimation through motor high-frequency characteristic impedances .....	49
3.2.2.	Estimation through analysis of high-frequency currents components.....	52
3.3.	Results and Discussion .....	56
3.4.	Publications.....	59
Chapter 4	Modelling in the High-Frequency Domain .....	60
4.1.	Review of the HF Models Proposed in the Literature .....	60
4.2.	Proposed Automatic Modelling Procedure .....	61
4.2.1.	Fitness function definition.....	65
4.2.2.	Form of the harmonic function and boundaries of the search space.....	66
4.2.3.	Generation of the initial population.....	68
4.2.4.	Selection, crossover and mutation operators.....	69
4.2.5.	Local optimization and aging variations .....	70
4.2.6.	Results and Discussion.....	70
4.3.	Simulation of the Overvoltage at Motor Terminals .....	74
4.3.1.	Inverter analytical model .....	74
4.4.	Publications.....	77
Chapter 5	Investigation of Possible Approaches for the Mitigation of Electrical Aging Effects	78
5.1.	Active Aging Control to Extend Drive Life Expectation.....	78
5.1.1.	Structure of the proposed active aging control system .....	78
5.1.2.	Simulation of electrical aging phenomena.....	82
5.1.3.	Simulation results and discussion .....	86
5.2.	Mitigation of the Electrical Stress by Employing Multilevel Converters.....	87
5.2.1.	Hypothesis and conditions for the comparison .....	89
5.2.2.	Loss and thermal model of the devices .....	92
5.2.3.	Results and discussion.....	94
5.3.	Publications.....	96

Chapter 6 Conclusions and Future Work .....	97
Bibliography .....	100

# List of Figures

<b>Fig. 1.1</b> – Total electricity consumption by sector, in Mtoe. [Source: IEA, Key World Energy Statistics].....	3
<b>Fig. 1.2</b> – Greenhouse gas emissions by source sector, EU-28, 1990 and 2017. [Source: European Environment Agency].....	4
<b>Fig. 1.3</b> – More Electric Aircraft concept: electrical energy as the main source to supply different subsystems, from [16]. ....	6
<b>Fig. 1.4</b> – Comparison of physical and electric properties of Si, SiC, and GaN semiconductor materials (left), and ON-state resistance [ $\Omega\text{mm}^2$ ] as a function of the breakdown voltage [V] for Si, SiC, and GaN semiconductor blocking regions (right). ....	9
<b>Fig. 2.1</b> – Photo of a portion of an assembled random-wound stator (a) and of a form-wound stator under construction (b).....	14
<b>Fig. 2.2</b> – Assembled form-wound stator with Roebel bars ready for external connection. ....	16
<b>Fig. 2.3</b> – Cross sections of the insulation system of a random-wound stator (a) and of a form-wound stator (b) to show the different parts of a typical insulation system. ....	17
<b>Fig. 2.4</b> – Example of overvoltage and ringing measured at the motor terminals, 50 ns rise time and 2 m cable. Source: [41]. ....	21
<b>Fig. 2.5</b> – Schematic representation of a variable frequency drive highlighting the inverter, cable, and motor characteristic impedances.....	21
<b>Fig. 2.6</b> – Simplified representation of the voltage reflection phenomenon in non-adapted line. ....	23
<b>Fig. 2.7</b> – Analytical calculation of ringing at motor terminals in the case of non-unit reflection coefficient ( $\rho = 0.75$ , in the example). ....	24
<b>Fig. 2.8</b> – Overvoltage measured at the motor terminals as a function of cable length for different PWM pulse rise times (a), and effect of the application of a second pulse at high frequency (b), from [43]. ....	25
<b>Fig. 2.9</b> – Distribute-parameters high-frequency model of the phase winding of an electric machine (a), and simplified circuit neglecting the inductive low-frequency behaviour. Source: [42]. ....	26
<b>Fig. 2.10</b> – Voltage distribution along the coils with growing value of $CE'CS' \cdot lw$ (a), and experimental voltage drop on the first coil of an electric machine (b). Source: [42]. ....	27

<b>Fig. 2.11</b> – Partial discharge activity within the insulation of a coil in a random-wound motor and examples of damaged insulations after breakdown observed with electronics microscope. Source [60].	29
<b>Fig. 2.12</b> - Development of the partial discharge in the air space between two insulating surfaces (a) and deployment of dipolar space charge in an ellipsoidal void (b).	32
<b>Fig. 2.13</b> – Test setup for the measure of partial discharges in the winding insulation of a low-voltage machine using a winding analyser equipped with PD-coupler (a), and partial discharge activity data recoded after 1000 pulses at 6 kV (b).	33
<b>Fig. 2.14</b> – PWM switching and partial discharge energy distributions (a), and variation of PD energy spectrum with pulse rise time (b). Source: [51].	34
<b>Fig. 2.15</b> – Definition of PD magnitude and occurrence time (a) and example of a phase distribution pattern expressed in terms of measured charge from [52] (b).	36
<b>Fig. 2.16</b> – Relationship between partial discharge inception probability and number of pulses to breakdown with voltage pulse amplitude in typical turn insulation. Source: [53].	37
<b>Fig. 2.17</b> – Average firing voltage (a) and average PD magnitude (b) as a function of the slew rate of the applied voltage pulses. Source: [51].	38
<b>Fig. 2.18</b> – PD magnitude (a) and repetition rate (b) as a function of the rise time of the applied voltage pulses. Source: [60].	39
<b>Fig. 2.19</b> – PD magnitude as a function of the pulse frequency (a) and average PD magnitude correlated with the number of pulses to breakdown (b). Source: [58].	39
<b>Fig. 2.20</b> – Statistics of PD magnitude (a) and repetition rate (b) as a function of the voltage pulse duration. Source: [59].	40
<b>Fig. 2.21</b> – Circuit diagrams showing the structure of a sine-wave low-pass filter in series RLC configuration (a) and of a dv/dt filter in LC connection (b).	42
<b>Fig. 2.22</b> – Example of inverter-motor combined design.	43
<b>Fig. 3.1</b> - Schematic structure of the experimental bench employed for the electrical aging procedure.	46
<b>Fig. 3.2</b> - Photo of the experimental rig used to perform the electrical aging procedure.	46
<b>Fig. 3.3</b> - Flow chart detailing the routine followed for the tests.	47
<b>Fig. 3.4</b> - Experimental overvoltage at motor side (a) and temperature on the motor case during an aging cycle, measured after a few hours from cycle start (b).	48

<b>Fig. 3.5</b> - Connection of the motor to the impedance analyser for the measurement of the common mode and differential impedances (a), and of the parasitic impedance (b). .....	49
<b>Fig. 3.6</b> - Common mode impedance: comparison between healthy and aged insulation state. ....	50
<b>Fig. 3.7</b> - Differential impedance: comparison between healthy and aged insulation state. ....	50
<b>Fig. 3.8</b> - Parasitic impedance: comparison between healthy and aged insulation state.....	51
<b>Fig. 3.9</b> - Schematic timing diagram of the high-frequency current measurement procedure. .	53
<b>Fig. 3.10</b> - Current in phase U measured after applying a voltage step for two different aging states. The detail shows the maximum and standard deviations of the measure. ....	54
<b>Fig. 3.11</b> - Spectrum of the currents for two different aging states and a detail of the frequency range of interest for the calculation of the deviation.....	55
<b>Fig. 3.12</b> - Distribution of the sample data of the high-frequency current, normalized with respect to their mean value.....	56
<b>Fig. 3.13</b> - Evolution of impedance deviation indices with aging time for the three motors under test.....	57
<b>Fig. 3.14</b> - Evolution of current deviation indices with aging time for the three motors under test. ....	57
<b>Fig. 3.15</b> - Evolution of spectrum deviation indices with aging time for the three motors under test.....	58
<b>Fig. 4.1</b> - Per-phase equivalent circuit of the high-frequency motor model used to implement the automatic modelling procedure, proposed in [76]. ....	62
<b>Fig. 4.2</b> - Fitting results of the optimization performed with the model proposed in [76]: common mode impedance magnitude (in dB) and phase (in degrees). ....	63
<b>Fig. 4.3</b> - Fitting results of the optimization performed with the model proposed in [76]: differential mode impedance magnitude (in dB) and phase (in degrees).....	63
<b>Fig. 4.4</b> - Fitting results of the optimization performed with the model proposed in [76]: parasitic mode impedance magnitude (in dB) and phase (in degrees).....	64
<b>Fig. 4.5</b> - Common mode impedance as a function of frequency, expressed as magnitude and phase. The black dashed line refers to the healthy insulation state, the red line to the measure taken after about 50 hours.....	66



<b>Fig. 4.6</b> – Differential impedance as a function of frequency, expressed as magnitude and phase. The black dashed line refers to the healthy insulation state, the red line to the measure taken after about 50 hours. ....	67
<b>Fig. 4.7</b> – Comparison of fitting accuracy between healthy and aged state for the common-mode impedance. ....	71
<b>Fig. 4.8</b> – Comparison of fitting accuracy between healthy and aged state for the differential impedance. ....	72
<b>Fig. 4.9</b> - Comparison of fitting accuracy between healthy and aged state for the differential impedance. ....	73
<b>Fig. 4.10</b> - Fitting accuracy to distinguish between different aging steps (common-mode impedance). ....	73
<b>Fig. 4.11</b> – Equivalent high-frequency circuit of inverter-cable-motor system (per-phase). ....	74
<b>Fig. 4.12</b> - Functional scheme of the analytical converter model. ....	75
<b>Fig. 4.13</b> – Voltage at the motor terminals with a 30-meter-long cable and 70 ns voltage pulse rise time: agreement between measured and simulated data. ....	76
<b>Fig. 4.14</b> – Simulation results: effect of cable length (left) and rise time (right) on the overvoltage and ringing at motor terminals. ....	77
<b>Fig. 5.1</b> - Conceptual scheme of the proposed control system for the Active Aging Control. ...	79
<b>Fig. 5.2</b> - Voltage waveforms at inverter and motor sides (top) and phase current showing the high-frequency transient (bottom). ....	80
<b>Fig. 5.3</b> – Schematic representation of the model employed for the simulation of electrical aging. ....	82
<b>Fig. 5.4</b> - Flow chart of the Active Aging Control simulation model. ....	83
<b>Fig. 5.5</b> - Average $NwQ\alpha$ values as a function of failure time of the specimens aged at two values of the test voltage. Source: [90]. ....	84
<b>Fig. 5.6</b> - Simulation results: trend of the damage growth rate (top), cumulative damage (middle), and ISI (bottom). ....	86
<b>Fig. 5.7</b> - Simulation results: Active Aging Control output in terms of pulse rise time. ....	87
<b>Fig. 5.8</b> – Circuit schematic of the SiC-MOSFET-based 2-level VSI (a) and of the Si-IGBT-based 5-level CHB multilevel converter (b). ....	89

<b>Fig. 5.9</b> – Line-to-line voltage and phase currents for the SiC-MOSFET VSI (a) and for the Si-IGBT CHB multilevel converter (b). .....	90
<b>Fig. 5.10</b> – Simulation circuit for the double-pulse test used for the generation of the LUTs of the SiC-MOSFET and of the IGBT models (a) and example of the turn-on and turn-off waveform for the SiC-MOSFET (b). .....	91
<b>Fig. 5.11</b> - Switching times of the devices as a function of the selected gate resistance: MOSFET (a), IGBT (b). .....	92
<b>Fig. 5.12</b> - Overvoltage on motor side obtained with the VSI (a) and with the CHB (b), and overvoltage factor as a function of the gate resistance compared for the two converters (c). ....	92
<b>Fig. 5.13</b> – Switching energy LUTs calculated from the device spice models: SiC-MOSFET with 17Ω gate resistance (a) and Si-IGBT with 10Ω gate resistance (b). .....	93
<b>Fig. 5.14</b> – Thermal network used for the simulation of the converter thermal behaviour. ....	94
<b>Fig. 5.15</b> – Conduction (star marker) and switching losses (circle marker) of the VSI (blue lines) and of the CHB converter (red lines) as a function of the load current. ....	95
<b>Fig. 5.16</b> – Efficiency of the VSI (blue line) and of the CHB converter (red line) as a function of the load current. ....	95
<b>Fig. 5.17</b> – Mass of the heat sink as a function of the thermal resistance between sink and ambient. The design points for the two converters are indicated as circle markers on the graph. ....	96

## List of Tables

<b>Table 2.I</b> – Comparison of filtering solutions for inverter-fed AC drives. Source: [Shackwhe_1998]. .....	42
<b>Table 3.I</b> – Rated parameters of the motor under test .....	47
<b>Table 4.I</b> – Mean absolute errors between measured and fitted values and healthy and aged data for $Z_{cm}$ and $Z_{dm}$ . .....	72
<b>Table 5.I</b> – Parameters of the Cauer equivalent thermal network of the devices used in the simulations. ....	93

# Chapter 1 Introduction

## 1.1. Background and Significance of the Topic

The Earth's climate has changed throughout history, mostly due to very small variations in Earth's orbit that change the amount of solar energy our planet receives. The current warming trend, however, is cause of significant concern because most of it is extremely likely to be the result of human activity since the 20th century and is proceeding at an unprecedented rate [1]. Ancient evidence found in tree rings, ocean sediments, coral reefs, and layers of sedimentary rocks reveal that current warming is occurring roughly ten times faster than the average rate of ice-age-recovery warming [2]. The planet's average surface temperature has risen about 0.9 °C since the late 19th century, a change driven largely by increased carbon dioxide and other human-made emissions into the atmosphere. The oceans have absorbed much of this increased heat, warming of more than 0.2 °C since 1969. Data from NASA's Gravity Recovery and Climate Experiment show that Greenland and Antarctica have lost significant mass of ice per year between 1993 and 2016. Global sea level has risen about 20 cm in the last century. Since the beginning of the Industrial Revolution, the acidity of ocean waters has increased by about 30%, as a result of humans emitting more carbon dioxide into the atmosphere and hence more being absorbed into the oceans [3].

### 1.1.1. *The European environmental action*

Climate change is the major critical issue of the modern era, a problem of global nature that requires immediate action to at least limit its consequences for humans. To this purpose, in 2007, the European Union (EU) launched the EU 2020 Climate and Energy Package, a set of binding legislation and measures to be adopted by the member countries to fight against climate change. The package identified three key targets aimed at putting Europe on the way to achieve a low-carbon economy: 20% cut in greenhouse gas emissions (from 1990 levels), 20% share of EU energy produced from renewables, and 20% improvement in energy efficiency. In 2014, these targets have been revised upwards as part of the EU 2030 Climate and Energy Framework, which will substitute the previous package starting from 2021. The new goals are set to 40%, 32%, and 32.5%, respectively (with revision clauses by 2023). Lately, on November 2018, the European Commission presented a long-term strategic vision “*for a prosperous, modern, competitive and climate-neutral economy by 2050*” [4], demonstrating a serious and continuative commitment of Europe to the environmental cause.

During the last decade, many efforts have been made to achieve the 2020 goals. Based on the latest figures, the EU is on track to meet its 20% targets for 2020. Greenhouse gasses emissions have been reduced by 22% between 1990 and 2017. According to the 2017/2018 reports, a 17.5% share of renewables in the energy production has been reached, with the latest projections showing that a level between 18.1% and 20.7% can be expected for 2020 with currently

implemented and planned renewable energy policy initiatives. The energy efficiency target seems to be the most difficult to achieve. Data from Eurostat in April 2019 have shown that the primary energy consumption in 2017 was 5.3 % above the 2020 targets, with a growing trend. If energy consumption continues to increase in the coming years, the EU will not reach its 2020 target. The EU needs to further intensify efforts to deliver energy savings in the short term [5].

### *1.1.2. The role of electric drives in the industry and transportations sectors*

In this scenario, power electronics, electric machines and drives are key technologies to reach the ambitious climate and energy targets that have been set for the near future. The recent advances in this field of technology, in fact, have the potential to make a difference in a wide range of sectors, from energy-production to industry and transportation, and are promising to address all the three main goals of the EU 2030 Framework. Fast-switching, low-losses semiconductor devices and more advanced power electronics converter topologies are key elements to increase the share of energy produced from renewable energy sources. They are promising for the efficient and reliable operation of the production plants and for their integration with the power grid according to the strict power quality requirements [6]. Advanced converter features and integration with Information Technology (IT) will also enable in the future an overall improvement of the power grid operation, regarding both transmission efficiency and reliability [7].

Based on the latest key world energy statistics from IEA [8], the industry sector is today responsible for almost 45% of the global electrical power consumption (Fig. 1.1), with 70% of the energy being processed by motors and drives. Enormous energy savings and energy efficiency improvements can be achieved in this field thanks to the advances in variable frequency drive (VFD) technology. In every industrial plant there are processes of some form that require adjustments to either meet normal operation requirements or achieve optimal performance. In many cases, these adjustments are still performed with mechanical or hydraulical actuators, which are often inefficient and waste both energy and material. With the recent developments in power semiconductor and converters, the diffusion of electric VFDs in a wide range of industrial applications has started growing. The advantages offered by VFDs include operation at non-synchronous speeds and wide continuous regulation range, improved process performance and efficiency, energy savings, and reduction in operation cost. Savings are provided by VFDs in two ways. Directly by consuming less power (e.g., in the case of centrifugal loads, whose power consumption is proportional to the cube of the speed), and indirectly by improving the quality of the production process (high steady-state and dynamical performance allow for less raw material to be wasted and for higher final product quality). Furthermore, the reduced mechanical stress and wear increase plant life and reduce maintenance time and costs. Two other important advantages of converter-fed motors are worth mentioning. First, the inherent soft-starting capability can be used to limit the high in-rush current, which is typical of induction motors at starting, thus saving the associated energy, eliminating the effects on the

supply side, and avoiding the intense stress on mechanical systems. Second, system complexity is reduced in all those applications that require reverse operation of the machine, which would need additional commutators to swap the phases to change the direction of motion. Regenerative breaking is also a useful feature for some applications.

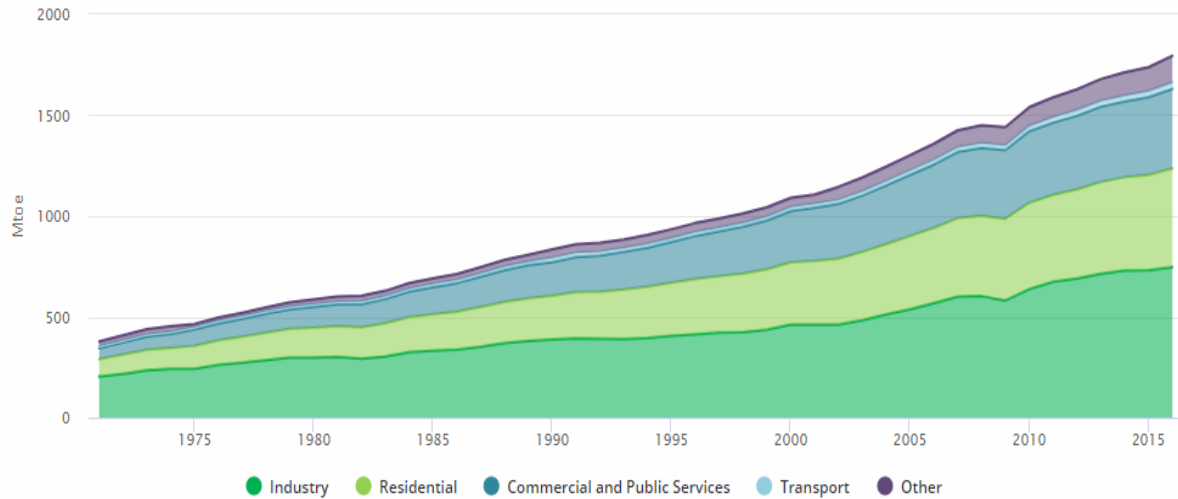


**Fig. 1.1** – Total electricity consumption by sector, in Mtoe. Source: IEA, Key World Energy Statistics.

The drawbacks of VFDs are generally related to the added encumbrance, their cooling requirements, and their relatively high initial investment. Alongside these practical aspects, which are generally considered in the cost-benefit evaluation phase, some other technological factors may be worth considering when buying a VFD. These factors are directly related to the voltage and current harmonics that are produced by the switching of the devices in pulse-width modulation (PWM) power electronics converters, and whose order and magnitude strictly depends on the commutation frequency of the semiconductor devices. Mechanical vibration and acoustic noise are due to the interaction of converter harmonics with the machine laminations. These issues may or may not represent a problem, depending on factory environment requirements and specific country legislation. Low order voltage harmonics (e.g., 5<sup>th</sup>, 7<sup>th</sup>, 11<sup>th</sup>, 13<sup>th</sup>) cause the circulation of current harmonics, which are only limited by the machine leakage inductance. These harmonics in turn produce additional losses in the stator and rotor windings, and the final effect is an increase in the motor temperature, so that a de-rated operational condition can be reached at the same temperature allowed for the nominal case. Hence, in the design phase, the motor needs to be over-sized accordingly [9]. Other than load-side harmonics, a converter also injects harmonics on the grid side. Such harmonics pollute the electric grid and can cause power quality or even stability problems if their levels are too high. The practices and requirements that a customer must meet for grid-side harmonics control in AC drives are generally defined by the technical standards. The most common solutions are described in [10], and generally determine an increase in the drive investment between 20% and 100%. All the afore-mentioned technical issues are directly related to the switching frequency at which the converter is set to operate. In fact, as the switching frequency increases, the produced harmonics

are shifted towards the high-frequency (HF) side of the spectrum, reducing in magnitude accordingly. Therefore, acoustic noise, vibrations, motor de-rating, and grid-side harmonic injection become less and less of a concern.

After the power-production industries, the transportation sector accounts for a large share of world's energy resources and it is responsible for a notable percentage of the pollutant emissions caused by the combustion of fossil fuels. For environment protection, a global transformation of the transportation sector towards low-carbon emissions and more efficient energy utilization will require significant improvements in the on-board energy production and consumption systems [11], [12].

Conventional vehicular transportation is based on internal combustion engine (ICE) propulsion systems, which uses petroleum products. In Europe, the transportation sector is responsible of about 25% of total greenhouse gasses emissions, as shown in Fig. 1.2. Moreover, according to the latest projections, the number of vehicles in operation is set to increase from 700 million to 2.5 billion units in the next 50 years. With the projected growth of CO<sub>2</sub> emissions, the importance of addressing fuel efficiency in both road and air transport is crucial for the environment. In order to meet the EU 2030 targets, novel concepts and technical innovations are being applied to all transportation systems to make them more energy-efficient, reliable, and safe with low or zero emissions at an affordable cost. The current common trend is to substitute the conventional petroleum-based propulsion systems with electric- or hydrogen-based solutions, fully or partially. The key role in this ambitious electrification trend is played by power electronics and electric drives.

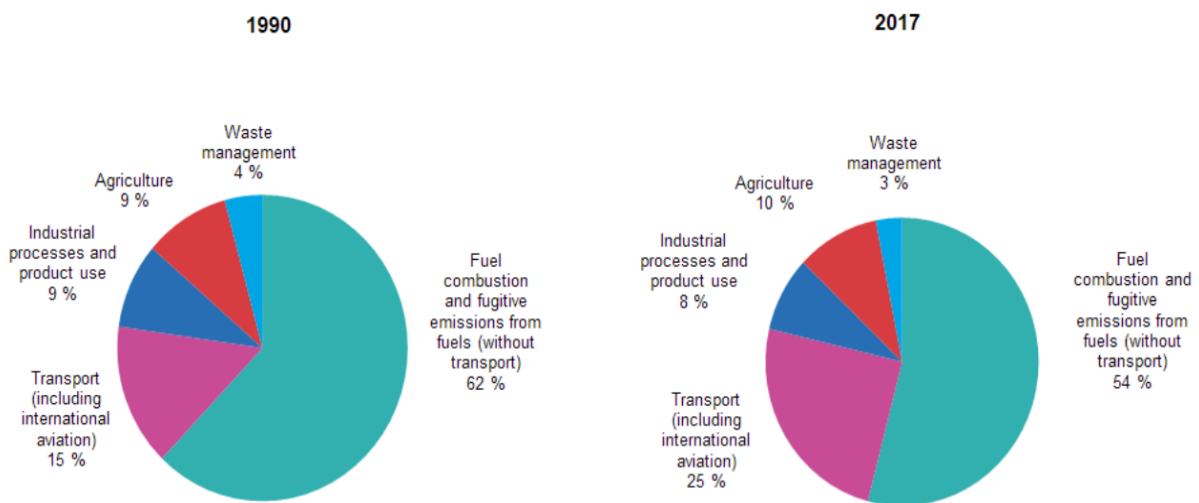


**Fig. 1.2** – Greenhouse gas emissions by source sector, EU-28, 1990 and 2017. Source: European Environment Agency.

In the last decade, electric vehicular technology has experienced a substantial growth in the market and it is today considered a sustainable alternative to conventional ICE systems. Electrification technologies in the vehicle sector can be broadly classified depending on their main energy source [13]:

- Battery electric vehicles (BEVs);
- Hybrid electric vehicles (HEVs);
- Plug-in hybrid electric vehicles (PHEVs);
- Fuel-cell vehicles (FCVs).

HEVs are gradually starting commercialization and are capturing a good market share, whereas FCVs are still under development and will require some time to reach acceptable levels of safety, reliability, and cost for the market stage. Despite the relevant research efforts of the last years, batteries are today the major limitation to the diffusion of pure electric vehicles. This energy source alone it is not able to achieve both long duration for long car trips and peak power when the vehicle needs it. However, the current trend is the hybridization of energy sources as a durable and sustainable alternative. A well-designed hybrid energy system can achieve a higher level of reliability, durability, and efficient power utilization with respect to single-source systems. Therefore, the next generation of electrified vehicles will most likely be made by PHEVs, as the current interest demonstrated by both industry and research institutes for the development of charging systems and infrastructures let perceive [14]. All considered, the role of power electronics in this field is central. Converters are needed to incorporate different components and provide compatibility for proper coordination among them to meet vehicle's requirements in all driving profiles. Among the features that power electronics converter can easily perform in this field there are [15]:

- easy voltage conditioning (interfacing two voltage levels, regulating the frequency, and converting between DC and AC)
- continuous regulation in a wide speed and power range, high efficiency
- high precision and accuracy when used to control electronic actuators and valves
- fast dynamic performance of both propulsion and auxiliary systems
- integration of diagnosis and sensing techniques to improve reliability and safety.

In the aerospace transportation field, the penetration of electric system technologies has lately started to grow faster than in the past, certainly thanks to the increased attention that this area of application has received from governments and environment control agencies. The great technological advancements of the last decades will soon enable hybrid or full-electric propulsion in small commercial airplanes, as some recently developed prototypes testify. An ambitious challenge has also been launched from NASA to promote development of cutting-edge technology in various engineering fields to enable the flight of large hybrid electric commercial airplanes. Today, the electrification trend in aerospace is a concept that is commonly referred to as More Electric Aircraft (MEA). The main energy source for subsystems on large aircrafts are the gas turbines that are primarily used to generate the thrust needed to propel the plane. They must also be designed to provide the power to supply the other on-board loads. In a conventional aircraft, from the main engines are derived four types of energy. Electrical power is used to supply avionics, lighting, in-flight entertaining systems, etc.



Pneumatic systems used for cabin pressurization, air-conditioning, and de-icing are fed by the energy obtained from part of the turbine high-pressure gas derived by bleeds. Hydraulic energy is the main form used for the flight control systems and auxiliaries, while mechanical systems are used mainly as service for the main engine. Having four separate power systems is an inherently inefficient design, and substantial weight and efficiency improvement can be achieved by using one single power source for all systems. Due to its flexibility and easiness of control, electrical energy has prevailed on the others in the MEA concept [16]. In Fig. 1.3, an electric generator connected to the gas turbine is used to produce the electric power required for supplying all the other on-board systems. The aim of MEA is to reduce operating cost, fuel consumption, and the environmental impact of future air transportation. The elimination of the pneumatic systems, for example, removes the need of bleed air systems, leading to a significant enhancement of the efficiency of the turbine. The substitution of the mechanical and hydraulic systems will drastically reduce equipment weight on the plane, thus improving fuel efficiency during flight. Furthermore, electric systems can offer features of flexibility in the design, efficient energy transformation, and advanced diagnostic options [17].

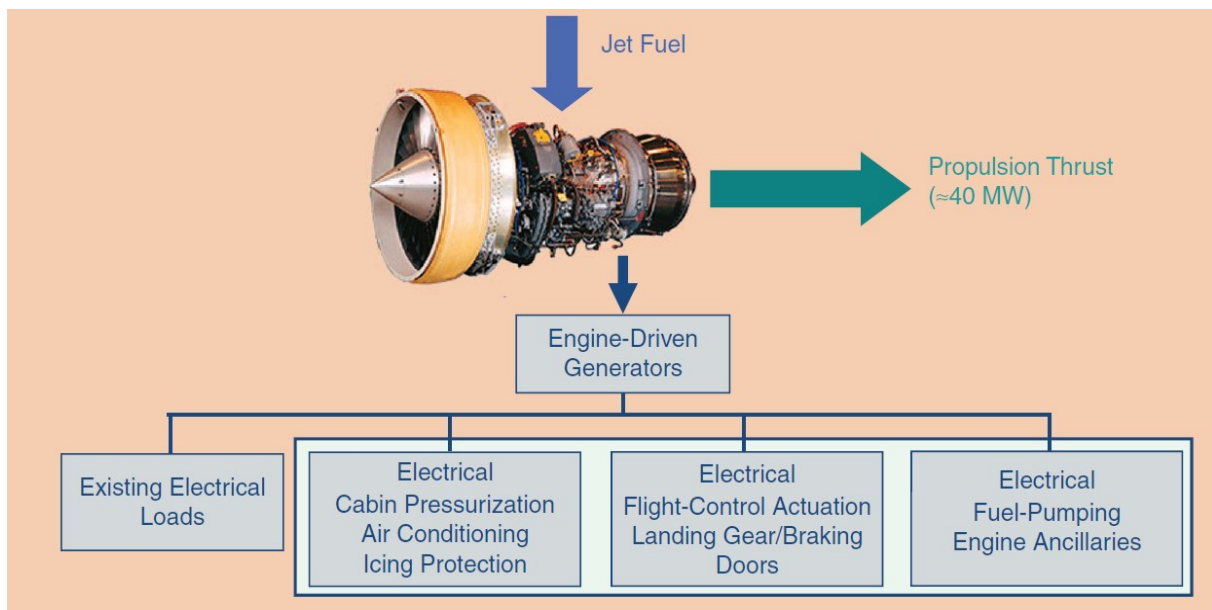


**Fig. 1.3** – More Electric Aircraft concept: electrical energy as the main source to supply different subsystems, from [16].

### 1.1.3. Increasing the frequency: current trends and practical challenges

In general, the main requirements for electric drives and power electronics converters are high reliability, availability, and durability, low cost (including investment, operation, and maintenance), limited encumbrance and weight, good steady-state and dynamic performance, wide speed range, high efficiency at different operative conditions, adequate mechanical robustness, ease of maintenance and repair, compliance with technical standards (e.g., electromagnetic compatibility EMC, power-quality, acoustic noise, etc). The priority of these features highly depends on the nature of the specific application. In ground transportation

applications, for example, overall system weight and efficiency over a wide speed range are of the utmost importance since they are directly connected to the energy consumption during the driving profile. A small drive volume is also important to improve its integration within the drivetrain and to improve mechanical stiffness. Cost is very important because it affects the market position of the product. Reliability is also crucial to ensure safety for the driver and reduce maintenance cost over time, while low acoustic noise and vibrations are considered for passenger comfort. Reliability and system weight/volume are critical requirements in the aerospace industry, as for the need to implement additional features such as predictive diagnosis and fault tolerance. The standards in this field are stricter than in the industry sector, especially regarding EMC and product certification. Efficiency, system complexity, and cost are then also considered [18]. Determining the industry priority is not possible a priori, due to the existing wide range of different industrial applications. Availability, durability, and ease of maintenance are generally a priority due to their impact on the continuous operation of the production line, and certainly the system cost is usually a key factor in play.

A common trend in many novel applications of electric drives is the high level of integration and system optimization. In this scenario, any solution to increase compactness and reduce the part count is highly desirable, and in the field of electric drives many advantages can be obtained by increasing the rotational speed of electric machines and the switching frequency of the power electronics. The advantages of adopting high-frequency converters and drives are multiple for many application fields [19]-[21]. The first key benefit is the reduction of the machine size and weight for the same rated power [22]. Electric machines, in fact, scale proportionally to the torque they can produce, being the latter proportional to the current flowing in the conductors and to the magnetic flux in the iron laminations. Since the power is the product of the torque and the rotational speed of the shaft, for the same power a faster machine requires lower torque, and thus is smaller. Therefore, the required amount of copper and iron is also smaller, which in turn reduces the production cost (good for higher market penetration and faster return of investment) and the weight (e.g., lower energy consumption in transportation). A more compact electric machine greatly improves system integration, leading to further cost reduction, increased product reliability, and improved quality of service and maintenance. The high-speed of the machine is then desirable because it adds flexibility in the optimization of the process: the compressors, the pumps, and the gas-turbines can be reduced in size, the quality of the product increases in cutting and milling processes, flywheels can be used to store energy. The gearbox to adapt the speed of the machine shaft to the mechanical load can be eliminated in many applications, leading to great improvements in efficiency, compactness of the system, cost, ease of manufacturing and maintenance, lower acoustic noise, increased mechanical stiffness and reduced wear [19].

High-speed electric machines have a high fundamental frequency, being this proportional to both the mechanical speed and the number of pole pairs. As an example, a 48,000 rpm, 2 pole pairs electric machine will require the converter to supply a voltage waveform with a

fundamental frequency of 1600 Hz. To be stably controlled, the drive control frequency must be much higher than the frequency of the electrical quantities [23]. Digital control systems generally apply the control action synchronously with the PWM carrier, i.e. either at the same frequency or at a frequency that is double the switching frequency. Therefore, to properly operate a high-speed machine, high-frequency switching is required. As a rule of thumb, the ratio of the switching frequency to the fundamental frequency should be larger than 10. In the previous example, the fundamental frequency of the motor was 1600 Hz, by considering a frequency ratio of 10 this means that the semiconductor devices should be able to operate at more than 16 kHz to achieve acceptable control performance. Modern silicon-based Insulated-Gate Bipolar Transistors (IGBTs) for medium power ratings can switch up to about 15-20 kHz, higher frequencies can only be achieved in certain low-current applications. However, the main technological limitation for IGBTs is the slow turn-off caused by their bipolar-carrier nature that makes so that more time is required to extract all the charge carriers at turn-off [24].

The need for high-power-density devices operating at higher frequency has been interesting both the industrial and the academical research for quite a long time. Silicon-based devices are not able to meet the fast switching requirement of modern high-speed high-power-density applications. It is for this reason that in the last 20 years the technology of wide bandgap (WBG) semiconductor materials, such as silicon carbide (SiC) and gallium nitride (GaN), have been attracting considerable attention. Their wide bandgap energy, which is more than three times higher than silicon (Si), allows these devices to operate at elevated temperatures, while retaining little leakage current. The larger breakdown strength for a given blocking voltage of SiC and GaN results in smaller devices with respect to their Si counterparts of the same ratings. Consequently, the storage of minority carriers is reduced, leading to a reduction in the switching losses and thus an increase in the switching frequency. Some of the properties that make SiC and GaN semiconductors highly attractive for power electronics applications are strongly dependent on the wide bandgap [24]. These main properties are compared in Fig. 1.4(left) with those of Si. In particular, the high-frequency behaviour and limits of WBG devices are determined by the *critical electric field* and the *saturated drift velocity*. The former quantifies the energy that the material can sustain before an avalanche of ionized carriers occurs in the semiconductor. The critical electric field is proportional to a power of the bandgap energy ( $E_g$ , in eV) [25]

$$K \cdot 10^5 \cdot E_g^n \quad (1.1)$$

The values of the parameters  $K$  and  $n$  are:  $K = 2.38$ ,  $n = 2$  for SiC,  $K = 1.73$ ,  $n = 2.5$  for GaN, and  $K = 2.5$ ,  $n = 0.75$  for Si. Due to their higher bandgap, SiC and GaN materials achieve ten times higher critical fields than Si, which allow for power devices to be designed with thinner, highly doped drift region for the same blocking voltage. The specific ON-state resistance, an important parameter that determines the device conduction losses, is also positively affected by the higher bandgap and by the increasing in the doping of the drift region: the specific ON-state resistance of WBG devices can be 350 times smaller than that of Si-devices [26]. Fig 1.4(right)

compares the ON-state resistance versus breakdown voltage limits for Si, SiC, and GaN semiconductors. The fact that the devices can be made thinner and more highly doped means that SiC and GaN devices are faster during commutation and thus can operate at higher frequency than Si devices. The second property, the saturated drift velocity, determines the frequency limits of power devices and the range of most efficient use. The HF capability of the material is, in fact, directly proportional to the material drift velocity, which is about double that of Si ( $10^7 \text{ cm} \cdot \text{s}^{-1}$ ) for WBG materials ( $2 \div 2.2 \cdot 10^7 \text{ cm} \cdot \text{s}^{-1}$ ). A higher drift velocity allows charge in the depletion region to be removed faster; therefore, the switching losses and the reverse recovery current are smaller, and the reverse recovery time is shorter.

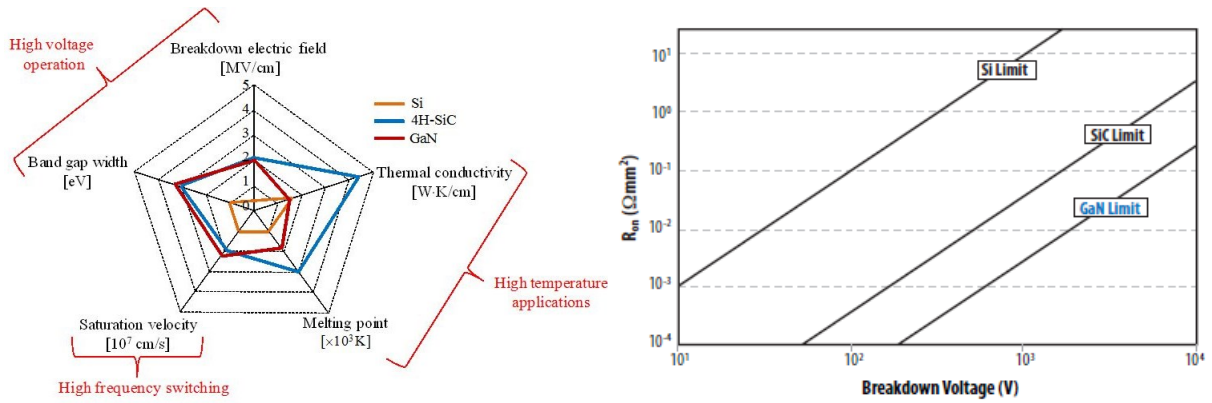


**Fig. 1.4** – Comparison of physical and electric properties of Si, SiC, and GaN semiconductor materials (left), and ON-state resistance [ $\Omega\text{mm}^2$ ] as a function of the breakdown voltage [V] for Si, SiC, and GaN semiconductor blocking regions (right). Source: [25].

The main practical advantages of WBG devices in power electronics application are the increased efficiency due to the lower losses, and the lower harmonics content due to HF switching, which also brings numerous advantages for the drive in terms of lower acoustic noise, better quality of grid-side power, and higher machine performance. As for high-speed machines, high-frequency power electronics allow for a considerable reduction of equipment weight and volume, especially because of the higher integration of power modules and because passive components dimensioning (i.e., capacitors, magnetics) scales inversely proportional to the frequency.

Today, SiC-MOSFET technology is becoming more and more mature, higher voltage and current ratings are becoming available from different manufacturers, making this product ready to be implemented in high-power-rating applications. GaN technology has also seen major advancements during the past years, and today the first 650 V product lines of High Electron Mobility Transistors (HEMTs) are approaching the market. Despite the great advantages that the WBG technology is bringing to power electronics in a growing range of applications, the fast switching behaviour and the high commutation frequency of SiC- and GaN-based semiconductor devices also introduce several new issues that are critical for drive reliability. These issues are mainly dependant on the very short turn-on and turn-off times of the devices in PWM applications, i.e. on the  $dv/dt$  of the voltage applied by the power converter to the load. Three main effects are directly related to the high  $dv/dt$  [9]:

- Increased electro-magnetic interference (EMI)
- Circulation of bearing currents and premature mechanical failure
- Increased electrical stress and premature insulation failure

EMI is defined as an unwanted electrical signal that produces undesirable effects in a control system, such as communication errors, degraded equipment performance and malfunction or non-operation [27]. All PWM converters can cause EMI with the equipment in their vicinity. However, this issue is particularly enhanced when switching speed increases. EMI noise can be both radiated and conducted. The former is easier to confine by appropriate shielding, however, high frequency conducted noise can become relevant and difficult to manage in those systems employing the new fast switching devices. Common-mode (CM) noise is a form of EMI that is induced on signals with reference to the ground, caused by the capacitive coupling of the system component to ground. This CM noise can become particularly intense in high voltage systems (e.g. medium voltage drives) and when long cables are used to connect the converter and the load, due to the increased parasitic capacitances. Many studies in the literature have investigated the EMI emissions of different converter topologies and devices [28], developing simulation models to assist the designer in early development of the system [29], or have proposed solutions to attenuate or compensate the emissions [30].

Rotating machines have three sources of shaft voltage: electromagnetic induction (due to small dissymmetry of the air-gap magnetic field), electrostatic coupling from internal sources (e.g., caused by charge accumulation on the rotor due to ionized air passing through the cooling fan), and electrostatic coupling from external sources, such as PWM inverters [31]. The high-frequency pulse train supplied by a PWM inverter makes so that high  $dv/dt$ 's are impressed across the stator neutral to ground (motor case) at high repetition rate. Due to parasitic capacitance between the machine parts, a portion of this waveform is also present on the machine shaft, which in turn causes the circulation of a current in the bearing of a magnitude dependent on the impedance of the path, generally very low [32], [33]. The circulating current mechanically damages the bearing of the machine, leading to premature failure.

The third issue that is caused by the high  $dv/dt$ 's in high-frequency PWM drives is the early winding insulation failure in the electric machine due to increased partial discharge (PD) activity. The two main phenomena that are responsible for this effect are the voltage reflections across the cable connecting the inverter and the motor that cause overvoltage at the motor terminals, and the uneven distribution of the applied voltage within the coils of the AC winding of the motor. The resulting increased electrical stress on the stator winding insulation system produces a sustained partial discharge activity that may quickly degrade the material and develop in an early irreversible failure. The literature regarding this phenomenon will be reviewed in Chapter 2 of this thesis, being this the main research topic of the doctoral activity detailed in this work.

## 1.2. Motivation and Goals

Considering the many benefits that the increasing penetration of high-frequency power electronics and high-speed drives can produce in industry, transportation and, in turn, environment, the need for technical solutions to mitigate the  $dv/dt$ -related issues is more pressing than ever. The basic phenomenological aspects of these problems have been studied for years; however, practical and easy-to-implement solutions have not been totally identified yet. In Chapter 2 of this doctoral thesis, the main phenomenology of insulation aging will be discussed, and some of the currently employed mitigation approaches will be described. A relevant knowledge gap that has been only recently approached by researchers is about the observable behaviour of an electric machine undergoing aging. What are the measurable effects of insulation degradation? Is it possible to develop estimation methods of the insulation condition that can be performed online and without the use of special, expensive laboratory equipment? Data of this kind could be profitably used to develop, for example, a cloud-based database to implement advanced prognostic and diagnostic features in industrial plants, in an industry 4.0 scenario. Furthermore, they could be of great help for designers to optimize various aspects of both machine and converter from a systemic point of view. Other than for prognostic maintenance applications, the information derived from an estimation of the machine insulation condition could be used actively with the purpose of lengthening the life expectancy of the drive, increasing the mean time between failures (MTBF) and ensuring better availability and reliability. The basic idea is to use the information about the aging progression, estimated through the online measure of electrical quantities, as a feedback for a multi-objective optimization control algorithm, appointed of selecting the best operating condition of the converter with the purpose of maximizing both drive performance and service duration, while satisfying the required mission profile.

What has been described above are the main motives and ideas that drove the research work that has been carried over for the last three years, as part of the Ph.D. program in Electrical and Information Engineering that this thesis is the conclusion of. The main goals of this research are to study the electrical aging phenomenon in electric machine fed by PWM inverters, to develop an online method for the estimation of the progression of aging, and to investigate possible solutions for its mitigation. This doctoral thesis presents the steps that have been taken and the results that have been achieved toward the goals that were set.

## 1.3. Structure of the Thesis

This doctoral thesis is organized as described below. Chapter 2 gives the reader an overview of the topic, focusing on the structure of modern electric machine insulation systems, discussing the main phenomena that are responsible for early insulation aging and failure, and reviewing the main literature works that, in the last decades, have focused on the study of the partial discharge phenomena and on their correlation with the voltage waveform produced by power

electronic converters. The focus of the research covers three main sub-topics, which are addressed in each chapter of the thesis. Chapter 3 presents a study on the electrical aging phenomenon investigating the possibility of estimating the insulation degradation via easily measurable electrical quantities, such as voltage and currents. In Chapter 4, the problem of modelling the drive system in the high-frequency domain is addressed for design and diagnosis purposes. An automated modelling approach is proposed for the machine high-frequency behaviour based on a genetic optimization routine. Coupled with the inverter and cable equivalent high-frequency circuits, this model can be used to simulate the phenomena that cause insulation aging. Furthermore, the proposed model can also consider the parametric variations induced by electrical aging according to the data presented in Chapter 3. In Chapter 5, two possible approaches are investigated to mitigate the electrical aging progression in high-speed machines insulation systems. On the one hand, the idea is proposed of actively controlling the switching behaviour of the power devices in the converter in response to the estimation of the aging state of the machine. This idea is investigated through simulation, using the models developed in Chapter 4, other than a PD-aging model based on statistic data from the literature. Finally, conclusions are drawn in the last chapter of this thesis.

## 1.4. List of Scientific Publications

### 1.4.1. Journals:

1. F. Cupertino, R. Leuzzi, V. G. Monopoli, and G. L. Cascella, "Design procedure for high-speed PM motors aided by optimization algorithms," in *MDPI Machines*, vol. 6, n. 5, 2018.  
doi: 10.3390/machines6010005
2. F. Cupertino, R. Leuzzi, V. G. Monopoli and G. L. Cascella, "Maximisation of power density in permanent magnet machines with the aid of optimisation algorithms," in *IET Electric Power Applications*, vol. 12, no. 8, pp. 1067-1074, 2018.  
doi: 10.1049/iet-epa.2017.0874
3. R. Leuzzi, P. Cagnetta, S. Ferrari, P. Pescetto, G. Pellegrino and F. Cupertino, "Transient overload characteristics of PM-assisted synchronous reluctance machines, including sensorless control feasibility," in *IEEE Transactions on Industry Applications*, vol. 55, no. 3, pp. 2637-2648, May-June 2019.  
doi: 10.1109/TIA.2019.2897969
4. R. Leuzzi, V. G. Monopoli, L. Rovere, F. Cupertino and P. Zanchetta, "Analysis and detection of electrical aging effects on high-speed motor insulation," in *IEEE Transactions on Industry Applications*. (Early access).  
doi: 10.1109/TIA.2019.2929013

### ***1.1.1. Conference proceedings:***

2. R. Leuzzi, P. Cagnetta, F. Cupertino, S. Ferrari and G. Pellegrino, "Performance assessment of ferrite- and neodymium-assisted synchronous reluctance machines," *2017 IEEE Energy Conversion Congress and Exposition (ECCE)*, Cincinnati, OH, 2017, pp. 3958-3965.  
doi: 10.1109/ECCE.2017.8096693
3. R. Leuzzi, P. Cagnetta, S. Ferrari, P. Pescetto, G. Pellegrino and F. Cupertino, "Analysis of overload and sensorless control capability of PM-assisted synchronous reluctance machines," *2017 IEEE Workshop on Electrical Machines Design, Control and Diagnosis (WEMDCD)*, Nottingham, 2017, pp. 172-178.  
doi: 10.1109/WEMDCD.2017.7947743
4. R. Leuzzi, V. G. Monopoli, L. Rovere, F. Cupertino and P. Zanchetta, "Effects of electrical ageing on winding insulation in high-speed motors: analysis and modelling," *2018 IEEE Energy Conversion Congress and Exposition (ECCE)*, Portland, OR, 2018, pp. 6886-6892.  
doi: 10.1109/ECCE.2018.8558376
5. R. Leuzzi, V. G. Monopoli, F. Cupertino and P. Zanchetta, "Active ageing control of winding insulation in high-frequency electric drives," *2018 IEEE Energy Conversion Congress and Exposition (ECCE)*, Portland, OR, 2018, pp. 1-7.  
doi: 10.1109/ECCE.2018.8558257
6. R. Leuzzi et al., "High-speed machines: typologies, standards, and operation under PWM supply," *2018 AEIT International Annual Conference*, Bari, 2018, pp. 1-6.  
doi: 10.23919/AEIT.2018.8577297
7. Riccardo Leuzzi, Vito Giuseppe Monopoli, Francesco Cupertino, and Pericle Zanchetta, "Comparison of two possible solution for reducing over-voltages at the motor terminals in high-speed AC drives," *21st European Conference on Power Electronics and Applications (EPE)*, Genova, 2019. (To be published).
8. Riccardo Leuzzi, Vito Giuseppe Monopoli, Francesco Cupertino, and Pericle Zanchetta, "Automated HF modelling of induction machines considering the effects of aging," *2018 IEEE Energy Conversion Congress and Exposition (ECCE)*, Baltimore, MD, 2019. (To be published).
9. J. Loncarski, V. G. Monopoli, R. Leuzzi, and F. Cupertino, "Operation analysis and comparison of T-type NPC Si IGBT and SiC MOSFET inverter-based high-speed drives," *45<sup>th</sup> Annual Conference of IEEE Industrial Electronics Society (IECON)*, Lisbon, Portugal, 2019. (To be published).



## Chapter 2 An Overview

### 2.1. Electrical Insulation Systems in AC Rotating Machines

The stator of an electric machine is made of three main components: the copper conductors, the magnetic core, and the insulation. Both copper and ferromagnetic material are the active parts of the stator since they permit the machine operation by allowing a path for the current and the magnetic flux to flow, respectively. The more the amount of these materials, the higher the machine torque. The insulation is instead considered to be a passive component, meaning that it does not help to produce a magnetic field or guide its path. From a design point of view, it increases the machine size, weight, and cost and reduces efficiency without helping to produce any torque. However, the insulation has the primary functional purpose of preventing short circuits between conductors or to ground. Without insulation, the conductors would be electrically in contact one another or with the grounded stator core, causing a failure. Additionally, the insulation is required to feature good thermal properties to let the proper dissipation of the heat produced from the  $I^2R$  losses in the conductors, and adequate mechanical properties to hold the conductors tightly in place and to prevent vibrations.

#### 2.1.1. *Types of stator winding construction*

Three basic types of stator winding constructions exist for electric machines in all the power ranges from a few watts to hundreds of MW [34]:

- Random-wound stators
- Form-wound stators using multiturn coils
- Form-wound stators using Roebel bars

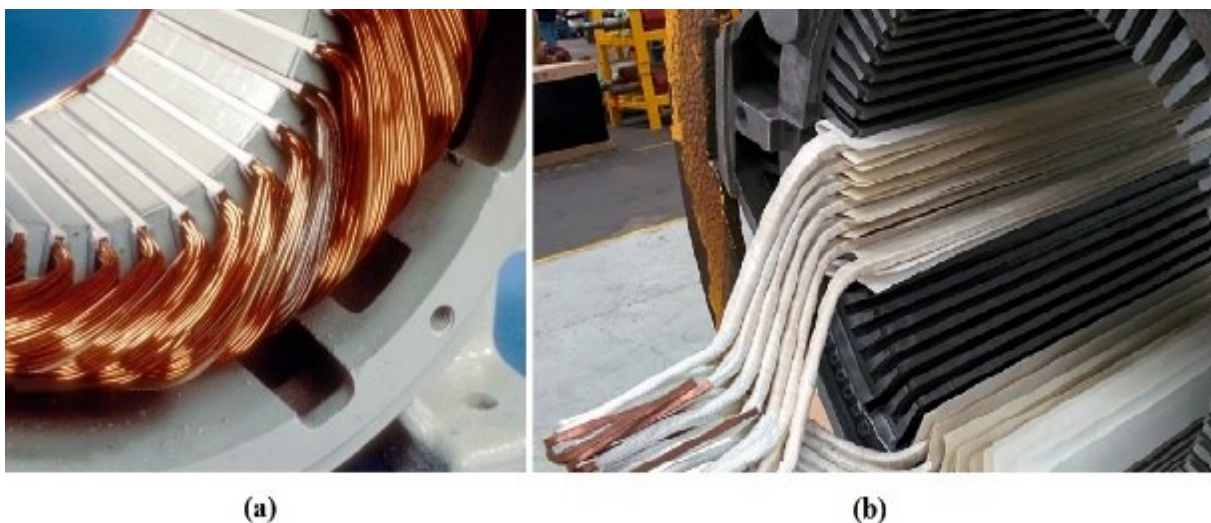


**Fig. 2.1** – Photo of a portion of an assembled random-wound stator (a) and of a form-wound stator under construction (b). Source: web.

Random-wound stators (Fig. 2.1a) are generally used for machines rated less than several hundred kW. They consist of round insulated copper wires that are continuously wound, by hand or using an automatic winding machine, through the slots of the stator core to form a complete coil. The coils are then connected in series according to the design schemes of the winding. At each loop, the wires are, in principle, randomly placed inside the slot, so that each conductor can be adjacent to any other wire of the slot independently of the electric potential difference. For example, a turn that is connected to the phase terminal could be placed against a turn that is operating at low or no voltage. In this latter case, the insulation material that separates them is subjected to the entire phase voltage. This is the reason why this type of construction is only limited to machines operating at voltages below 1 kV, otherwise the thickness of the insulation would be inefficient and impractical.

Form-wound stators (Fig. 2.1b) are used in machines that operates at voltage levels above 1 kV, typical of high-power-rating applications up to 50-100 MW, among which large generators are accounted. In this type of construction, the winding is made of pre-formed insulated coils that have been assembled before the insertion in the stator slots, according to the winding scheme of the design. The coils usually consist of 2 to 12 turns made of several sub-conductors called strands, formed as copper bars shaped according to the slot dimensions and insulated one each other. The turns of the whole coil are stacked one over the other at each loop, and then each coil is connected in series to the others to form the phase winding. This type of construction ensures that each turn in a coil is adjacent to another turn with the smallest possible voltage difference to minimize the thickness of the insulation that separates them. In a form-wound 3-kV stator winding with 10 coils of 10 turns each, for example, the maximum voltage between adjacent turns is 30 V, instead of the full 3 kV voltage that would have been possible in a random-wound structure. In very large machines (e.g. the generators in power production plants) a whole pre-formed coil become difficult to insert without the risk of mechanically damaging both the coil and the iron core during the process. For this reason, the coil is “*split*” in two halves that can be more easily inserted and that are then electrically connected only on the stator external periphery. These halved coils are commonly named as Roebel bars (Fig. 2.2).

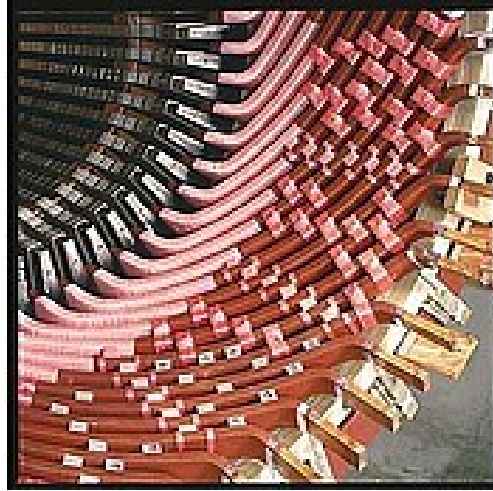


**Fig. 2.2** – Assembled form-wound stator with Roebel bars ready for external connection. Source: web.

### **2.1.2.      *Composition of stator winding insulation systems***

The stator winding insulation system of an electric machine contains several components to ensure that electrical short circuits do not occur, that the heat from the conductor is extracted and transmitted to the heatsink (the iron core), and that the conductors are held in place and do not vibrate during operation. Three basic parts form any insulation system:

- Strand insulation
- Turn insulation
- Groundwall insulation

Generally, in random-wound stators the strand insulation and the turn insulation are identified in a single component. Some manufacturers combine the strand and the turn insulations also in form-wound stators. This approach eliminates some manufacturing steps and increase the copper utilization factor of the slot, thus improving the power-volume ratio of the machine and its efficiency. However, practical experience has demonstrated that the average life expectation of machines that are manufactured this way is usually much shorter than those built with separate insulation components [35]. In high-voltage systems, where form-wound stator construction is employed, additional components may be required, such as stress-relief coatings and end-winding-support elements. The schematic representation of the insulation system for a random-wound stator and for a form-wound stator are shown in Fig. 2.3a and Fig. 2.3b, respectively.

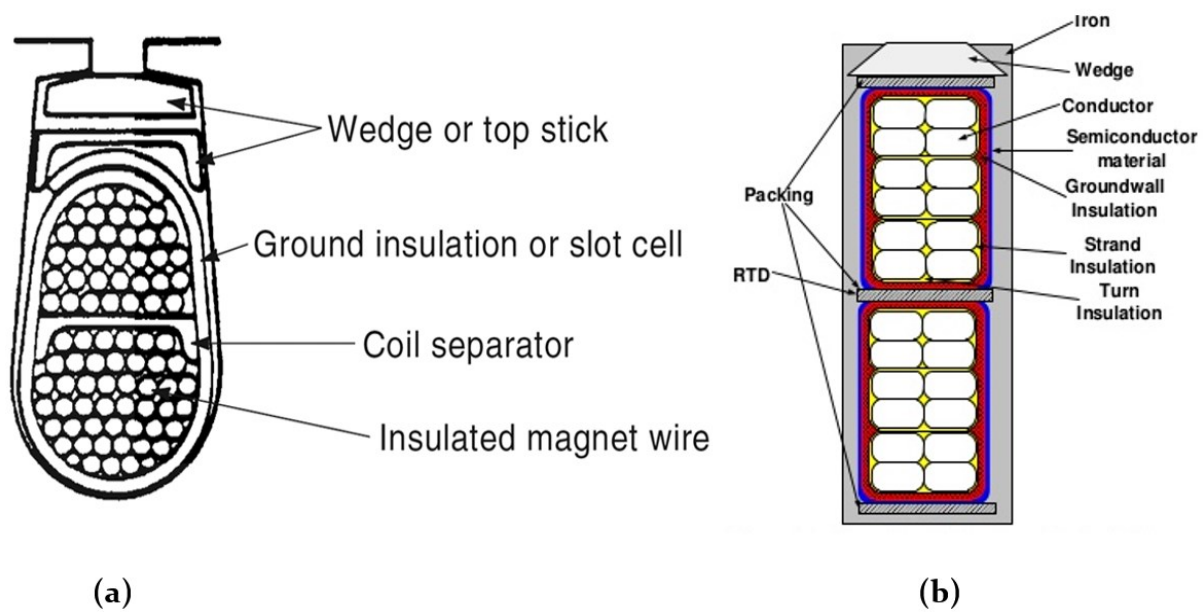


**Fig. 2.3** – Cross sections of the insulation system of a random-wound stator (a) and of a form-wound stator (b) to show the different parts of a typical insulation system. Source: [34].

Form-wound machines usually employ separate strand and turn insulation. Dividing a turn in parallel strands is often a necessity dictated by both mechanical and electrical reasons. From the mechanical point of view, a conductor that is big enough to carry the whole phase current has a relatively large cross-section, therefore it is stiff and difficult to either bend or form into the desired bar shape. Employing smaller strands makes it easier to manufacture. From an electrical point of view, there are mainly two reasons for stranding. On the one hand, in large conductors the current tends to flow on the periphery of the conductors rather than in the central portion, a phenomenon that is called *skin effect* and that results in additional conductor losses, which contribute to overheat the conductors making it more difficult to extract the heat. The second reason is that larger conductors are more susceptible to varying magnetic fields leaking from the main flux in the core and crossing the slot perpendicularly to the conductor path. This varying flux will produce the circulation of eddy current within the cross-section of the conductors, resulting in increased losses and heat generation. By employing strands with lower cross-section, both the skin effect and the parasitic currents are drastically reduced, improving copper utilization, efficiency, and thermal management. The strand insulation has the purpose of electrically separating the strands from one another. The voltage difference across this insulation layer is less than a few tens of volts, therefore it is usually very thin. Since this insulation part is in contact with the active conductors, where the heat from the conduction losses is produced, the strand insulation must exhibit very good thermal properties to let the heat to flow from the copper to the stator iron. The strands are connected in parallel, therefore a short circuit between a few wires is not the cause of a total winding failure: the stator winding losses will increase in the shorted strands creating a local temperature increase. Some

manufacturing measures may be taken when building new stators to prevent early shorts and lengthen the life of the winding.

The turn insulation must prevent short circuits between two turn of a coil. In the case of a short circuit, the shorted turns act as the secondary winding of an autotransformer, making a very large current flow in the faulted turns that causes a rapid local temperature increase in the winding, which melts the insulation material and quickly develop in a phase-to-ground fault. At this point the winding is irreversibly damaged and requires re-winding to be operated again. Therefore, turn insulation is functional to the proper operation of an electric machine. In random-wound stators, the worst-case scenario is a voltage across the turn insulation being as high as the phase-to-neutral voltage (in single-layer windings) or as the phase-to-phase voltage (in double-layer windings). In this latter case, however, it is common manufacturing practice to put an extra dielectric dividers or wedge to separate the two phases within one single slot, thus adding a thicker layer of insulation. The turn insulation of random-wound stators is usually relatively thin because the rated voltage of most machines is below 600 V. However, in the case the motor is fed by a PWM inverter (as it will be discussed in Section 2.2), the voltage level on the winding insulation can be superior to the design limits, giving rise to premature aging or failure mechanism.

In form-wound stators, the voltage across the turn insulation is essentially the total voltage between phase terminal and neutral point divided by the total number of turns of the phase. This results in a limited voltage difference across each turn, so that the turn insulation thickness can be minimized. Manufacturers must take great care to ensure that each coil of the winding is the same and that each turn has the same inductance. The turns are, in fact, a voltage divider for the phase voltage, thus only if their impedance is the same the phase voltage is uniformly distributed across the coils. Inverter operation, however, may introduce distortion in the transient distribution of the voltage along the coils increasing the electrical stress on the turn insulation also.

The groundwall insulation has the purpose to separate the copper conductors from the stator iron core, which is grounded. A failure of this insulation layer is usually detected by a ground fault relay that excludes the machine from service. For a long service life of the machine, the groundwall insulation must satisfy rigorous electrical, thermal, and mechanical requirements. In random-wound stators, in its basic form, the groundwall insulation is the same as the turn insulation, dimensioned to sustain the full phase voltage between the phase terminals and neutral point. Generally, additional sheets of insulating material are inserted both to increase the separation of the coils from the iron core and to keep the conductor tightly in place in the slot and in the end-winding portion. Thermally and mechanically speaking, the requirements of this insulating sheets are less stringent than those of the strand/turn insulation.

In form-wound systems, the groundwall insulation must be considerably thicker because it must sustain the whole rated phase voltage between the conductors and the ground. In theory, the coils connected to the neutral point have a much lower insulation requirement than those

connected to the phase terminal, therefore it could be possible to adopt different insulation thickness for the various portions of the slot. However, to avoid additional design and manufacturing complexity and other possible asymmetries in the magnetic behaviour of the machine, the common practice is to keep uniform groundwall insulation. A good practice can be to switch the external electrical connection of the coils of the machine after a certain amount of time in order to take advantage of the lower voltage of the turns adjacent to the neutral point, with the purpose of lengthening the service life of the insulation. In form-wound machines, the groundwall insulation is the main path of heat transmission from the copper to the stator core. For this reason, to prevent excessive copper temperatures this layer should have the best possible thermal properties. To increase its thermal conductivity, it is essential to avoid the formation of air pockets within the dielectric bulk, which would lower the dielectric strength of the material making it more susceptible to break. Finally, the groundwall insulation layer requires good mechanical properties to avoid that the conductors vibrate or move during normal operation. In fact, as a result of the interaction of the two magnetic fields generated by the currents flowing in the top and bottom copper bars in each slot, large magnetic forces act on the conductor itself. These magnetic forces are proportional to the square of the current and to the inverse of the distance between the bars. In 50 Hz sinusoidal systems the amplitude of the magnetic force oscillates at a frequency of 100 Hz, causing the bar to vibrate [34]. If the groundwall insulation is full of air pockets, the conductors may be free to vibrate and bang against the dielectric material or one another, leading to insulation abrasion and damage. As depicted in Fig. 2.3b, the groundwall insulation of form-wound stators also comprehend a semi-conductive coating that is used as stress-relief layer to avoid the inception of partial discharges in the air clearances between the coil and the grounded iron core. With a sufficiently low resistance, this coating is essentially at ground potential because of its contact with the core. Therefore, the voltage difference across the clearance is near to zero and PDs cannot incept. Another method to avoid this phenomenon is to adopt a manufacturing process called vacuum pressure impregnation (VPI) that consist in filling the air gaps with epoxy or polyester resins, thus theoretically eliminating the need for the stress-relief coating. A similar approach is also often used for random-wound motors, where the full stator is immersed in a resin bath in vacuum to make the epoxy to fill possible gaps. The resin also acts as a glue to help improve the mechanical stiffness of the stator winding.

## **2.2. Phenomenology of Insulation Aging and Failure in PWM-fed AC Drives**

The first reports of failure in electric systems due to the voltage harmonic distortion introduced by power electronic converter date back to the 1950s, when the British Rail linked the increased failure rate of power cables to the converters used to supply the traction motors [36]. The research in this field, however, only started in the 1980s, when the first generation of fast switching transistors became available on the market. In 1992, a paper by Persson [37] was

among the firsts to recognize that voltage surges from PWM inverters using IGBTs caused random-wound machines to fail due to gradual aging of the stator turn winding insulation. IGBT- and MOSFET-based PWM converters produce voltage square waves with rise fronts from 2-3 to tens of  $\text{kV}/\mu\text{s}$ , with repetition frequencies up to tens of kHz. Modern WBG devices are quickly invading the scene, and will soon further increase these operating conditions, with their capability to commute at more than 100 kHz and with turn-on and turn-off times in the order of ns. These improvements in power electronics technology offer many advantages in terms of efficiency and performance. However, the reliability of electric equipment, such as motors and generators, is strongly challenged by the increased number of registered early failures. The causes of these premature failures could be many, from the intrinsic aging accelerated by solid state components via electro-mechanical fatigue, to the faster thermal degradation of the insulation due to local overheating caused by the higher frequency. However, the research in the last years has demonstrated the major role of the voltage waveform generated by power electronic converters [38].

### ***2.2.1. Reflection of voltage waveforms across long cables***

The voltage waveform supplied by a modern PWM power electronics converter is made of a train of repetitive pulses with very fast rise and fall fronts. The number and width of these voltage pulses depend on the switching frequency of the converter and on the modulation technique, respectively, while their steepness is related to the turn-on and turn-off dynamic of the semiconductor devices and to the DC-link voltage level. Significant voltage oscillations and overshoots have been observed at the terminals of motors fed by PWM inverters in the presence of high  $dv/dt$  switching and relatively long cables [39], [40]. According to the transmission line theory, when a steep voltage pulse propagates along a non-adapted transmission line, i.e. a line that is not terminated on its characteristic impedance, a reflection phenomenon may occur. As shown in Fig. 2.4, the direct consequence of the voltage waveform reflection is that increased voltage peaks and ringing appear at the end of the line [41].

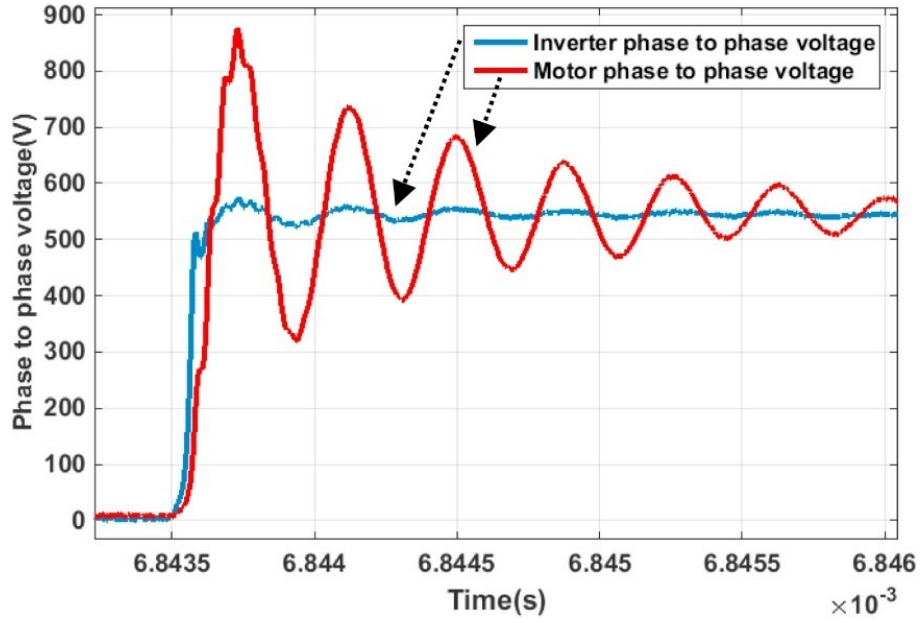


**Fig. 2.4** – Example of overvoltage and ringing measured at the motor terminals, 50 ns rise time and 2 m cable. Source: [41].

Let us consider a typical VFD consisting of a three-phase voltage source inverter (VSI), an AC motor, and a connecting cable of a certain length,  $l$ . A schematic representation of the system is depicted in Fig. 2.5, where the cable characteristic impedance is indicated as  $Z_{cb}$ , the inverter output impedance as  $Z_{inv}$ , and the motor input impedance as  $Z_{mot}$ .

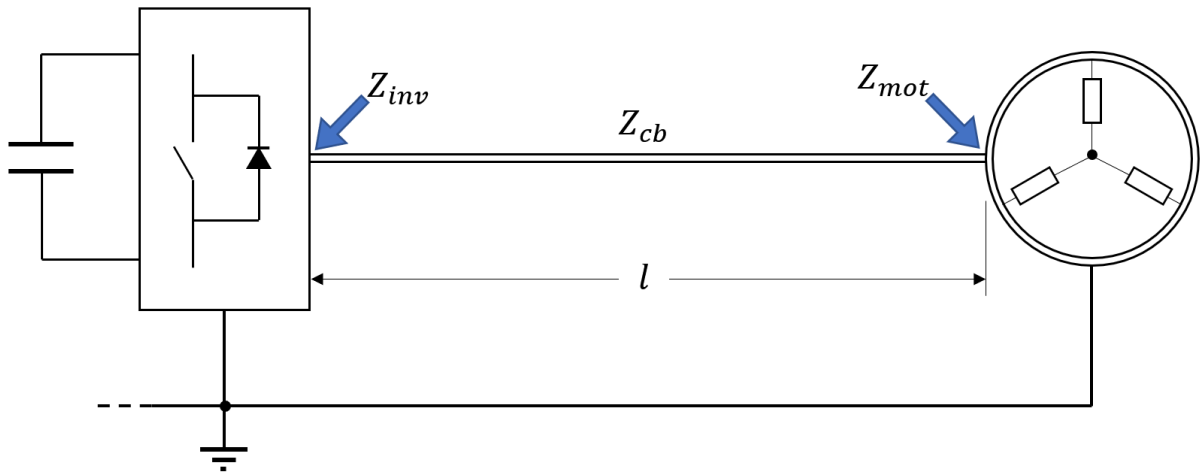


**Fig. 2.5** – Schematic representation of a variable frequency drive highlighting the inverter, cable, and motor characteristic impedances.

In the following, the term “steep voltage pulse” will be used in reference to a pulse of voltage with a rise time (i.e., the time required for the voltage to build up to the DC-link level), that has the same order of magnitude of the wave propagation time along the cable. Under this condition, in fact, the voltage reflection phenomenon become significant. The waveform propagation time ( $t_p$ ) can be calculated knowing the length of the cable and the propagation speed of the voltage



along it ( $v$ ). The propagation speed is a function of the cable per unit inductance  $L_{cb}$  and capacitance  $C_{cb}$ .

$$L_{cb} = \frac{\mu_0}{2\pi} \ln\left(\frac{2a}{d}\right) \quad (2.1)$$

$$C_{cb} = \frac{2\pi \cdot \varepsilon_0 \varepsilon_r}{\ln\left(\frac{2a}{d}\right)} \quad (2.2)$$

Where  $d$  is the conductor diameter and  $a$  is the distance between two conductors. Combining (2.1) and (2.2) the propagation velocity is obtained:

$$v = \frac{1}{\sqrt{L_{cb} C_{cb}}} = \frac{1}{\sqrt{\mu_0 \varepsilon_0 \varepsilon_r}} \quad (2.3)$$

In (2.3),  $\mu_0$  is the magnetic permeability of vacuum,  $\varepsilon_0$  is the electric permittivity of air, and  $\varepsilon_r$  is the relative permittivity of the propagation medium, which in this case is the cable. Assuming a value of the relative permittivity of 4, typical of the insulation material used in cable manufacturing, the propagation speed is about 150,000 km/s (about half of that of the light in vacuum). The propagation time is then

$$t_p = \frac{l}{v} \quad (2.4)$$

The propagation time is directly proportional to the length of the cable and to the square root of the per unit cable parameters. The longer the cable, the longer the propagation time. If the cable has a length of 10 m, for example, the propagation time is equal to 0.67  $\mu$ s, which is of the same order of magnitude of the rise time of modern semiconductor devices.

When a voltage waveform that is propagating along a line reaches a point of discontinuity of the medium, such as the connection between the cable and the motor, part of it is reflected towards the source. The ratio of the reflected wave to the incoming wave is called reflection coefficient ( $\rho$ ).

$$\rho = \frac{u_{ref}}{u_{inc}} = \frac{Z - Z_{cb}}{Z + Z_{cb}} \quad (2.5)$$

Referring to the schematic representation of the phenomenon in Fig. 2.6, one can calculate both the positive reflection coefficient (wave reflected at motor terminals), considering that the impedance of the motor is much higher than that of the cable ( $Z_{mot} \rightarrow \infty$ )

$$\rho_{mot} = \frac{Z_{mot} - Z_{cb}}{Z_{mot} + Z_{cb}} \approx 1 \quad (2.6)$$

and the negative reflection coefficient (wave reflected at the inverter terminals), with the inverter impedance being negligible with respect to that of the cable ( $Z_{inv} \rightarrow 0$ )

$$\rho_{inv} = \frac{Z_{inv} - Z_{cb}}{Z_{inv} + Z_{cb}} \approx -1 \quad (2.7)$$

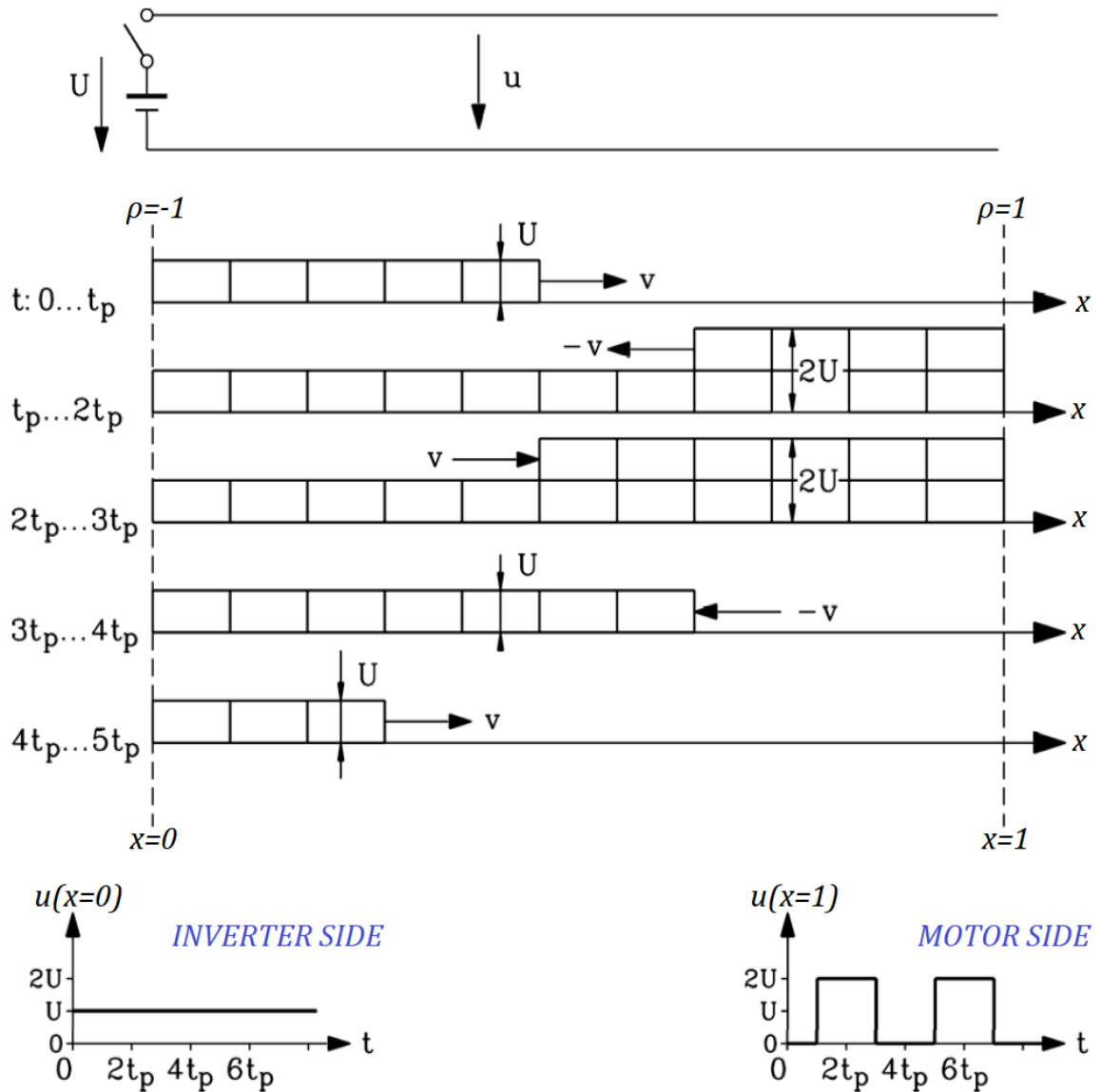


**Fig. 2.6** – Simplified representation of the voltage reflection phenomenon in non-adapted line. Source: [42].

At the time  $t = 0$ , the inverter applies a voltage pulse of magnitude  $U$  that is propagated to the motor terminals in a time equal to  $t_p$ . Here, the waveform is reflected with  $\rho = 1$ , therefore the new wave sums to the previous and the amplitude becomes  $2U$  propagating towards the inverter. After  $t_p$  the new wave reaches the start of the line, where the reflection coefficient is  $-1$ . The new reflecting wave with amplitude  $-U$  cancel the previous one, so that the voltage remains constant at the inverter side. At the time  $t = 3t_p$ , the reflected voltage reaches the motor again.

This time, however, the propagating voltage is negative, thus the reflected wave has amplitude  $+U$  and the voltage at the motor terminals reaches zero. The same phenomenon repeats again after a time of  $4t_p$ . As a result, the inverter voltage remains constant, but at the motor side an oscillation is created between no-voltage and 2 times the DC-link voltage. This oscillation, or ringing as it is usually referred to as, has a frequency of  $1/4t_p$ , which therefore it is only dependant on the cable parameters and length. In the example, the worst case has been assumed for the reflection coefficient of the motor, furthermore, the cable has been modelled as a lossless line ( $R = 0, G = 0$ ). In a real application, the waveform is affected by the damping of the cable and the reflection coefficient at the motor side is lower than 1. Consequently, the ringing is damped after each period until the steady-state voltage equal to the DC-link voltage is reached, according to the transient of a second-order system (Fig. 2.7).

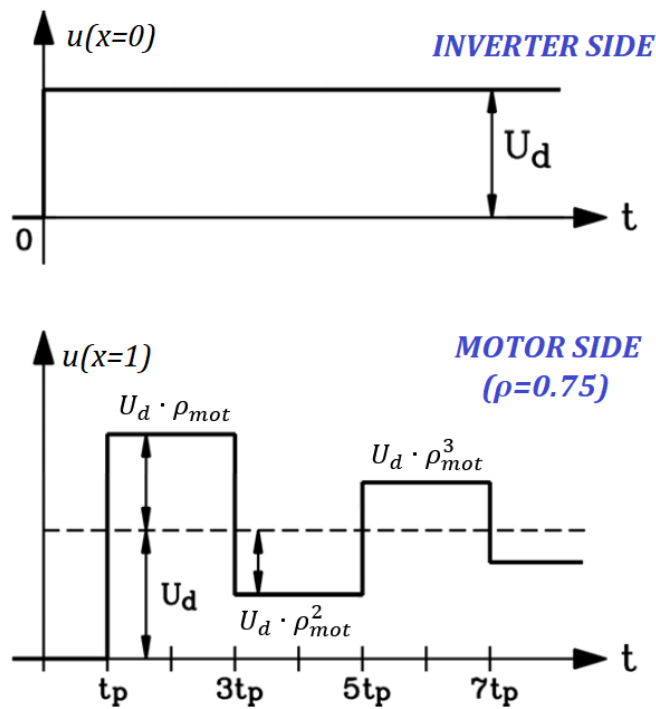


**Fig. 2.7** – Analytical calculation of ringing at motor terminals in the case of non-unit reflection coefficient ( $\rho = 0.75$ , in the example). Source: [42].

While the cable characteristic impedance is almost independent on the current flowing in it, the motor impedance can vary depending on its size.  $Z_{mot}$  is somehow proportional to the frequency and to the leakage inductance of the machine, which is proportional to the square of the number of turns of the winding. At a given rated voltage, the number of turns usually decreases with the motor size. Therefore, the motor input impedance decreases with the increased motor size [42]. This is particularly relevant when applied to high-speed machines, which reduce their frame size for a given rated power as the nominal speed increases. As a result, a high-speed motor will present a higher impedance, thus the resulting reflection coefficient will be closer to unity and the overvoltage at its terminals will be higher.

As seen in the previous examples, the overshoot at the motor terminals when voltage reflections occur can reach up to 2times the applied inverter voltage, i.e. the DC-link voltage. The steepness of the voltage pulses supplied by the converter with respect to the cable length play a key role in determining the effective overvoltage in practical applications. For a given voltage rise time ( $t_r$ ), a critical cable length exists that leads to full voltage overshoot:

$$t_r = 2t_p = \frac{2l_{cr}}{v} \Rightarrow l_{cr} = \frac{vt_r}{2} \quad (2.8)$$

For example, if the voltage rise time in a modern VSI application with 540 V on the DC-bus is 70 ns, then the critical cable length ( $l_{cr}$ ) is 5.25 m, that is, with a cable longer than 5.25 m the voltage applied on the motor at each PWM pulse will be about 1080 V. Shorter cables will avoid the voltage on the motor to reach the worst case, however there will be still a voltage higher than the one on the inverter side [38]. Fig. 2.8a shows a plot of the overvoltage measured at the machine terminals as a function of the cable length, for different pulse rise times, the devices that technologically allow the achievement of that steepness are indicated [43]. In [43], another possible phenomenon is described for those cases where the switching frequency is high enough that the inverter applies a second pulse before the transient of the previous pulse is over. Rise time has a lesser impact on this effect, which is illustrated in Fig. 2.8b.

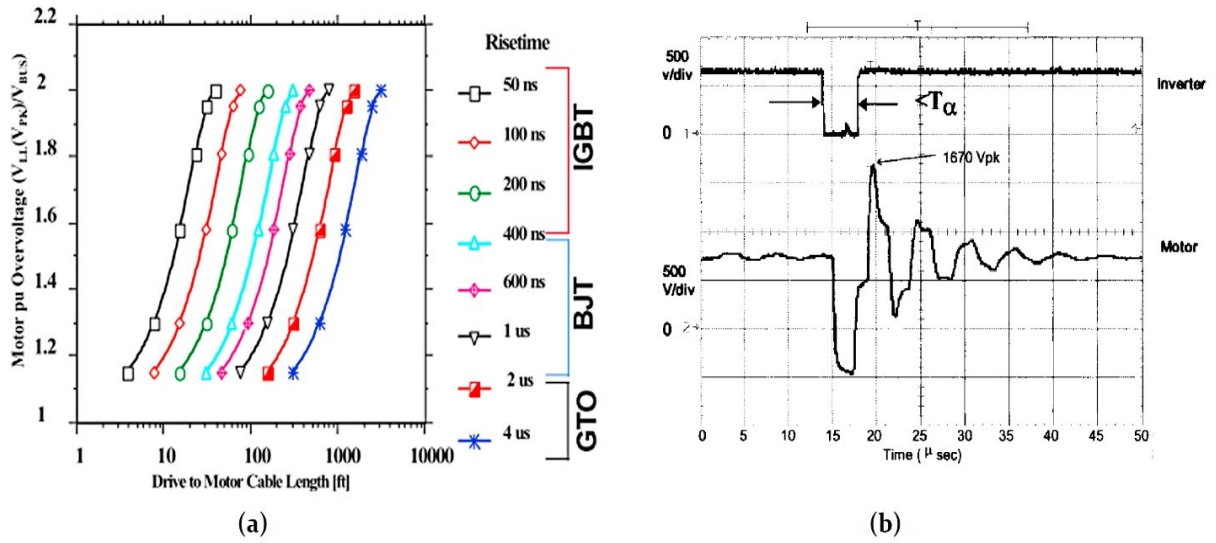


**Fig. 2.8** – Overvoltage measured at the motor terminals as a function of cable length for different PWM pulse rise times (a), and effect of the application of a second pulse at high frequency (b), from [43].

### 2.2.2. Uneven distribution of the voltage along the coil

The voltage applied to the phase winding of an electric machine is not instantaneously divided to all the coils as in an ideal pure-resistive voltage divider circuit. Instead, a transient is triggered when the pulse is applied due to the machine parasitic capacitances. To take this effect into account, a distributed HF model of the winding must be used, as that shown in Fig. 2.9 [42].

The series inductance of the turn  $\Delta L$  can be neglected at high frequency since the value of the reactance at high frequency tends to infinite (open circuit). In the figure,  $\Delta C_E$  and  $\Delta C_S$  are the capacitance between conductor and stator iron (grounded) and between the two conductors of adjacent turns, respectively. By indicating the spatial point along the coil as  $x$  and the differential increment as  $dx$ , the simplified circuit looks like the one in Fig. 2.9b. Here,  $C'_E$  and  $C'_S$  are defined in p.u. according to (2.9) and (2.10), where  $N_s$  is the number of turns per winding and  $\Delta x$  is the length of the turn (i.e., winding length is  $l_w = N_s \cdot \Delta x$ ).

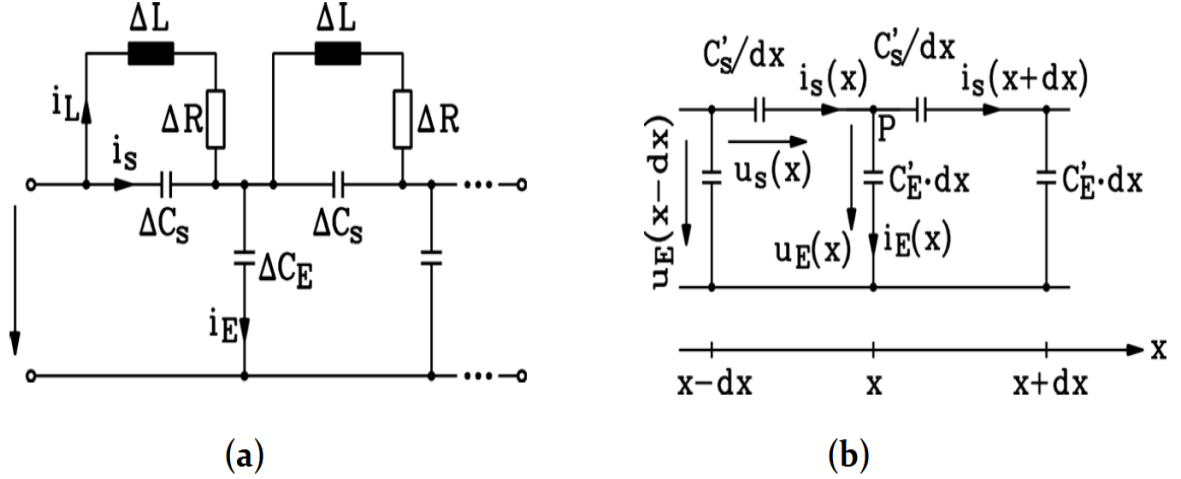


**Fig. 2.9** – Distribute-parameters high-frequency model of the phase winding of an electric machine (a), and simplified circuit neglecting the inductive low-frequency behaviour. Source: [42].

$$\Delta C_E = \frac{C_E}{N_s} = \frac{C_E}{l_w} \cdot \Delta x = C'_E \cdot \Delta x \quad (2.9)$$

$$\Delta C_S = C_s N_s = C_s \frac{l_w}{\Delta x} = \frac{C'_S}{\Delta x} \quad (2.10)$$

In order to calculate the electrical transient of the distribution of the voltage along the winding, the differential equation (2.11) must be solved.

$$\begin{cases} \frac{d^2 u_E(x)}{dx^2} - \frac{C'_E}{C'_S} u_E(x) = 0 \\ u_E(x=0) = U_d \\ u_E(x=l_w) = 0 \end{cases} \quad (2.11)$$

Leading to:

$$u_E(x) = U_d \frac{\sinh(\sqrt{C'_E/C'_S} \cdot (l_w - x))}{\sinh(\sqrt{C'_E/C'_S} \cdot l_w)}, t = 0 \quad (2.12)$$

From the result in (2.12) it can be deduced that the voltage distribution transient along the turns of the phase winding is dependent on the parasitic capacitances introduced by the insulation system of the winding itself. For higher values of the ratio  $C_E'/C_S'$ , and for longer windings, during the first instants after the application of a voltage pulse the first turn experiences the lion's share of the full voltage, even the 55-65% as observable in Fig. 2.10.

In [44] a multiconductor lossy transmission line model is employed to calculate the interturn electrical stress when the above-described phenomena occur, and the experimental results confirm the simulation results. According to the authors, the maximum interturn voltage sensibly varies with the rise time of the applied pulse and is almost independent, for a given winding structure, on the length of the connection cable. Furthermore, the interturn voltage is uniformly distributed for pulse rise times longer than 100 ns.

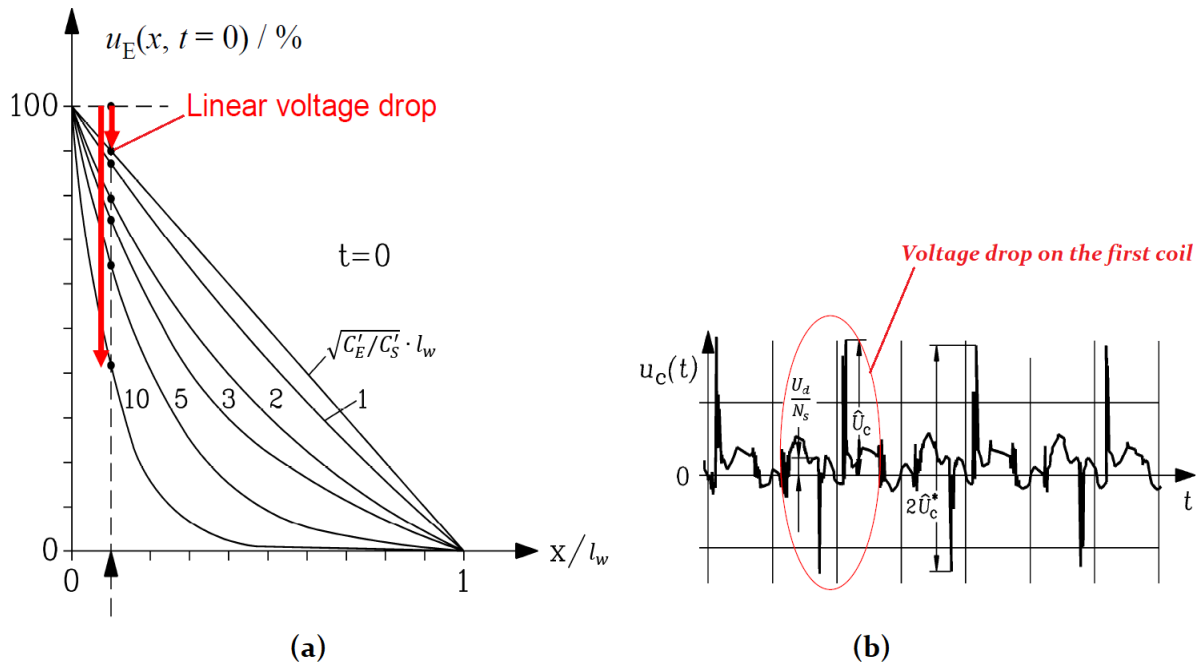


**Fig. 2.10** – Voltage distribution along the coils with growing value of  $\sqrt{C_E'/C_S'} \cdot l_w$  (a), and experimental voltage drop on the first coil of an electric machine (b). Source: [42].

### 2.2.3. Partial discharges, insulation aging and failure mechanisms

The two previously discussed phenomena are recognized as the main causes of the increased electrical stress on the winding insulation system of inverter-fed electric machines. With the increasing switching frequency and fast commutation transients of modern semiconductor devices, the risk of early insulation failure is also growing. This had never been a concern for low-voltage random-wound machines before the introduction of VFDs. Even in this case, failure due to insulation breakdown was rare in drives employing the first generation of semiconductor devices (e.g., SCRs and GTOs) due to their low  $dv/dt$ 's and the low commutation frequency. With the advances in WBG semiconductor devices, however, the turn-on and turn-off times of the devices are becoming shorter and shorter (tens of nanoseconds), so that a cable length of 3-4 m

is enough to reach the maximum voltage magnification at the motor terminals. The increasing switching frequency of the PWM waveforms of modern converters may also contribute to increase the overvoltage by a factor higher than two [43]. Moreover, these steep voltage transients on motor side may produce an unbalanced distribution of the voltage along the coils, so that during the first instants after the application of each PWM pulse, the first turns are exposed to the major share of the peak voltage.

The direct consequence of the high frequency trend in electric drives technology is that the level of electrical stress that the insulation is called to withstand becomes much higher than the design specifications. Therefore, the probability that partial discharges incept within the weak spots of the insulation systems greatly increases, affecting system reliability, availability, cost, and sometimes safety. The weak spots of an insulation system are usually air pockets, also called voids or cavities, that form during the stator winding manufacturing process. Although many techniques exist to reduce imperfections and void within a winding (e.g. VPI), the formation of cavities cannot be prevented completely. The insulation of form-wound stators is designed to have additional elements to cope with partial discharge suppression, such as PD relief coatings, however, this is not the case for low-voltage motors, where the dimensional and space utilization constraints are more demanding or the cost has to be kept at a minimum. Partial discharges are small sparks that ignite in the air pockets of an insulating material, they have generally a quite short duration and are not visible to the human eye. However, due to the high repetition rate of the PWM pulses, PDs are continuously triggered and extinguished, causing delamination and erosion of the insulation enamel and eventually leading to the final breakdown. When an insulation fails, a large short-circuit current starts flowing between two adjacent conductors, the additional heat that is produced cannot be dissipated quickly, therefore the temperature rise locally. Soon, the rest of the insulation material melts due to the high temperature and some conductors come in direct contact with the stator iron, causing an irreversible fault. The ground fault protection intervenes by excluding the machine from service. To put the machine in service again, the stator winding must be re-winded, with the associated manufacturing costs and the economic losses deriving, for example, from closing a production line. In safety critical applications, such as automotive or aerospace, an early failure could pose severe risks for the life of passenger and other peoples. Therefore, current technical standards in those fields require the certification of products and systems under very high levels of reliability and availability.

In Fig. 2.11, some examples of damaged insulation after breakdown due to total discharge are depicted. The term “total discharge” is usually used to refer to the high-intensity discharge that provoke the insulation breakdown. It can be observed in the pictures that the contact area between the two conductors is most likely the place where the final spark occurs. The perimeter of the contact area, in fact, is where a cavity has more chances to form, and thus is the weakest spot in the system. This is especially true when round-cross-section conductors are employed, since the curvature makes it difficult to obtain insulation continuity in the overall winding. In the uppermost picture in Fig. 2.11 the light radiated from an area of the winding during intense

PD activity is shown by using some light-sensitive equipment. The stator depicted in the picture has not been immersed in the resins to fill the air pockets in the windings, thus it is more susceptible to the inception of numerous and intense PDs.

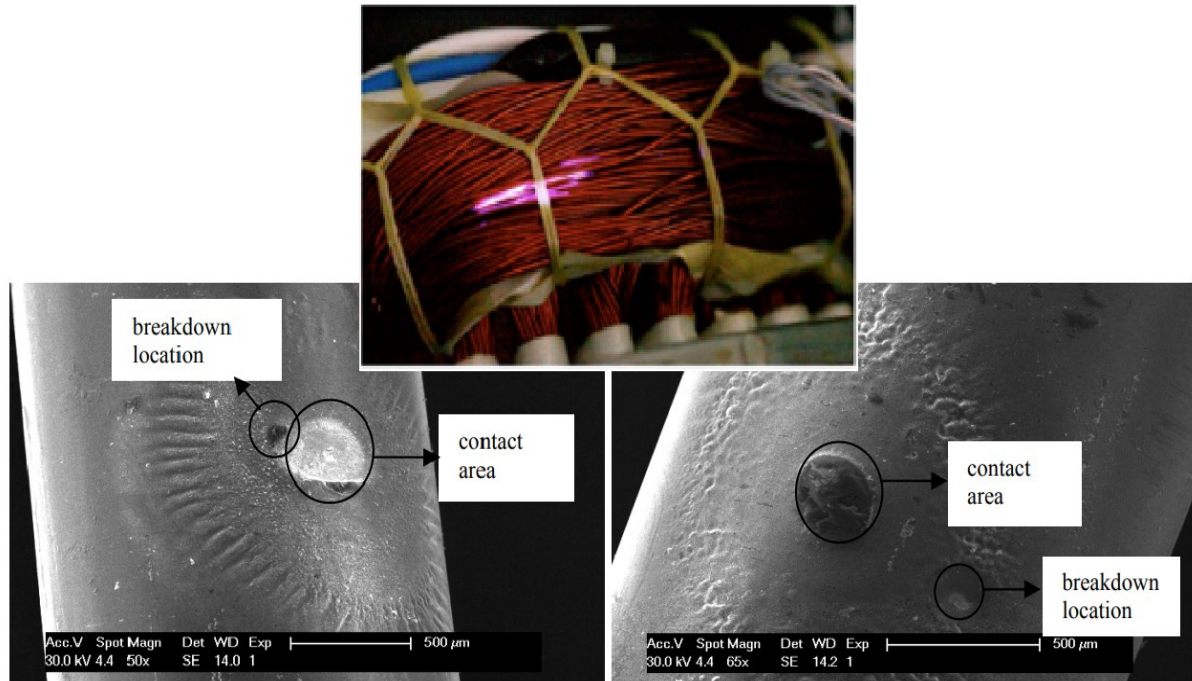


**Fig. 2.11** – Partial discharge activity within the insulation of a coil in a random-wound motor and examples of damaged insulations after breakdown observed with electronics microscope. Source [60].

Many studies in the scientific literature have been conducted in the past years aiming at understanding the partial discharge phenomenon and at developing analytical models based on their physic nature. A comprehensive description of the main physical phenomena leading to the inception and development of partial discharges in gases and gas-insulation surfaces, such as the air contained within the defects in the insulation, was given by Niemeyer in [45]. Here, the various possible defect shapes are modelled and classified according to the geometrical dimensions that are relevant for the description of the PD phenomenon. The effects of the defect geometry on the inception conditions and on the development of the discharge are then investigated to propose a generalized model taking the defect shape into account with dimensionless form factors. Furthermore, the paper proposes an analytical model for the statistical features of partial discharges, for the charge distribution caused in the cavity by the PD event, and for the memory effect associated with it. The model is validated in [46], where the evolution in time of the discharge activity is also studied. The complete description of the physical phenomenon of the ionic discharges in gas insulation, although it certainly is an interesting topic, is outside the scope of this doctoral thesis, which is focused on the macroscopic effects of the insulation aging that are measurable or that can be estimate through the measure of electrical quantities. In this thesis, only the basic principles that govern the phenomenon are



covered, such as the conditions for the inception of a discharge and the role of the space charge deployed by a PD event in their measurement and insulation aging.

The inception of partial discharges in an air pocket of the insulation between two conductors is essentially driven by the electric field across the defect, which is enhanced by the geometry of the defect itself and by the existence of the charged particles released during previous PD events. In the literature, these charged particles are commonly referred to as *space charge*. Considering the simple model of two infinitely long conductor plates separated by a bulk of dielectric material with thickness  $d$ , the electric field across the insulation resulting from the application of a voltage  $V_0$  between the plates is given by

$$E_0 = \frac{V_0}{d} \quad [V/m] \quad (2.13)$$

A spherical defect of radius  $r$ , filled with air, is now assumed to be present within the insulation bulk. The defect shape somehow distorts the electric field across the air pocket, intensifying it. Further field enhancement may occur if space charge exists on the void surface due to previous discharges. The enhanced field across the void ( $E$ ) can then be calculated as the sum of two contributions according to (2.14), where the dimensionless factors  $f(r, \varepsilon_r)$  and  $g(r, \varepsilon_r)$  are used to take into account the distortion introduced by the defect properties.  $\varepsilon_r$  is the relative permittivity.

$$E = E_a + E_q = f(r, \varepsilon_r) \cdot E_0 + \frac{q_s}{g(r, \varepsilon_r) \cdot \varepsilon_0 r^2} \quad (2.14)$$

In (2.14),  $E_a$  is the contribution to the defect field from the applied voltage, while  $E_q$  is the additional term due to the presence of the space charge  $q_s$ . In the following, the enhanced electric field  $E$  will be simply referred to as electric field, implying that it represents the effective electric field across the defect.

For the inception of a partial discharge across the air void, two conditions are necessary. First, a starting electron must be present on the surface to trigger the ionic avalanche process that constitutes the body of the discharge. Secondly, the electric field across the defect must exceed the dielectric strength of the material within the defect, i.e. air. The initial electron can be generated either via volume ionization mechanisms (e.g., an ionic radiation that excites an electron in the air volume may “free” it from its molecular bonds) or surface detachment mechanisms (such as the excitement of an electron in the valence band of the dielectric molecules at the gas-surface interface). Regardless of the specific mechanisms involved, the key concept is that the availability of the first electron determines the statistical properties of the partial discharge activity, such as inception delay, repetition rate, phase distribution with respect to the applied voltage waveform, etc. These properties will be discussed in the following paragraphs. If a starting electron is available, the second condition for the inception is that the electric field within the defect exceeds the critical field strength of the material. For air at

ambient temperature, atmospheric pressure, and low humidity the value of the critical field is about 3 kV/mm. The higher the pressure of the gas, the higher the value of the critical field. For example, in large hydrogen-cooled generators operating at pressure around 300 kPa, the dielectric strength is about 9 kV/mm. Typical insulation materials used in electric machines, such as polymer or epoxy resins with a relative permittivity between 3.7 and 4.0, the critical field is in the order of hundreds kV/mm, more than 100 times the value for air. It is for this reason that partial discharges are more likely to occur in air pockets created within the insulation, weak spots of the system whose number should be minimized during the manufacturing process.

Fig. 2.12a shows a schematic drawing of the development process of a partial discharge, starting from an initial electron available at the surface of the insulating material and culminating with the deployment of the space charge at the defect walls. When the critical field in the defect is exceeded, the field is strong enough to accelerate the first available electron in the same direction of the applied field. During his path towards the positive electrode, the electron collides with the air molecules and transfers some of its kinetic energy to other electrons, which in turn are excited and accelerated. As a result, an avalanche is incepted by this collision-ionization mechanism. At this point, the partial discharge is self-propagating through the defect in the direction of the field, extending up to the opposite surface. The electrons that are transferred with the discharge and deposited on the surface of the void leave behind positively charged molecules (holes) at the starting surface, as illustrated in Fig. 2.12b. This charge separation process creates an electric dipole in the cavity that produces an electric field opposite to the one at the beginning of the discharge. Across the void, the total field collapses to a residual value until most of the space charge is either absorbed by the material or decays. The delay introduced by the time required for the space charge decay is called space charge memory effect because, during the time it stays in place the space charge constitutes the memory of the PD event in two ways, by contributing to the potential difference across the defect and by being source for some of the mechanisms of first electron generation.

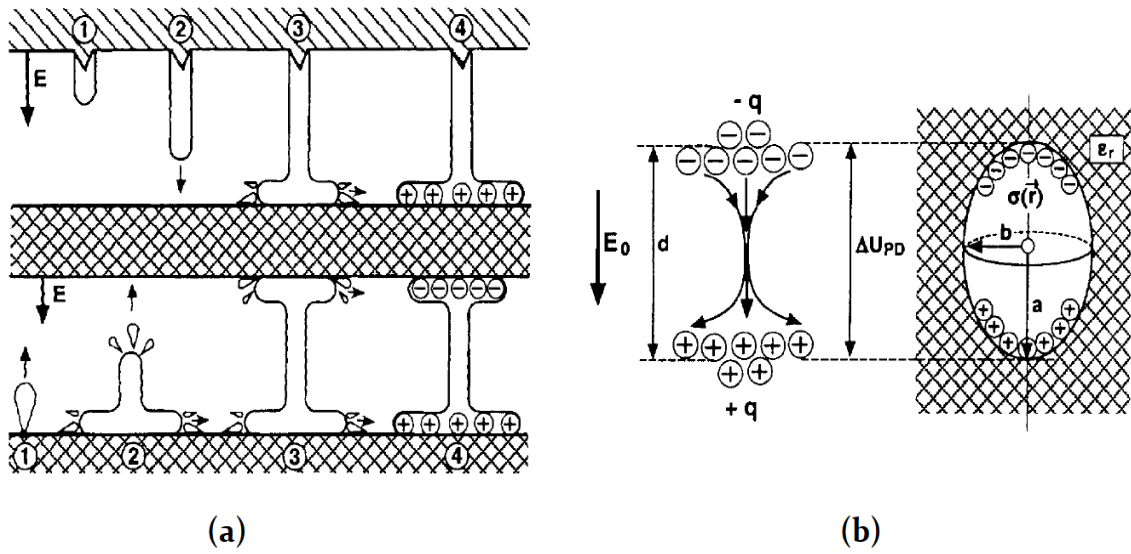


**Fig. 2.12-** Development of the partial discharge in the air space between two insulating surfaces (a) and deployment of dipolar space charge in an ellipsoidal void (b). Source: [45].

In [45], a relationship is given that relates the space charge deployed by a PD event to the voltage drop  $\Delta V_{PD}$  across the defect and to the geometry of the defect itself (through dimensionless factor  $g$ ):

$$q = \pm g \pi \epsilon_0 r \Delta V_{PD} \quad (2.15)$$

This charge is defined as the “true” physical charge that has flown through the partial discharge. This charge has been found to control the damage that the PD induces in the insulation material and therefore it is responsible for insulation aging. The role of space charge in accelerating the insulation aging is very well discussed in a comprehensive survey written by Montanari [47], where the author discusses the most recent theories and modelling approaches that correlates the space charge to partial discharge inception and to insulation aging and failure mechanisms.

Other than having been recognized as a key factor in insulation aging, the space charge is also important for partial discharge detection and measurement. In fact, the dipolar charge distribution deployed by a PD event induces charges on the conductors near the location of the PD. These induced charges cause a signal to travel from the defect location to the conductor terminals, where a measuring device can be connected. If the transmission of the signal from the defect location to the measurement equipment is lossless and the signal is properly conditioned, then the measured charge coincides with the induced charge, and the information can be used to give a measure of the intensity of the PD event. The model proposed in [45] gives an equation to correlate the induced charge with the true charge, giving a useful link between a measurable quantity and the real PD magnitude. Fig. 2.13 shows the partial discharges occurring in the stator winding of a random wound machine acquired during a high-voltage test campaign. The equipment that has been employed for the test is the MTC2 Winding Analyzer from Schleich, a surge tester for motor insulation evaluation that is provided with a PD-coupler and

a filter for PD measurement. The coupler is directly connected to the terminals of the machine, then a series of high-voltage surges are applied to the winding. The signals acquired at each pulse are then filtered and shown on the screen. However, modern PD measuring systems are not based on the direct measure of induced charge at the terminals of conductors, despite some equipment can still be found by some manufacturers. The most common approach to the measure of partial discharges is the use of an ultra-high-frequency (UHF) antenna pointed in the direction of the PD source (e.g., a crossed wire sample being tested, a coil, or an entire stator). The reason can mainly be found by thinking to the purpose that drives the measures that need to be performed today. Due to the well-recognized effects of PWM voltage waveforms on the insulation of electric machines, in fact, recent technical standards have been extended to comprehend specific regulations for testing insulation systems under repetitive voltage pulses [48], [49]. However, high-frequency switching produces EMI in the MHz and GHz ranges of the spectrum. In [50], the authors have found that switching disturbance has significant energy distribution below 500 MHz and that the energy distribution above 500 MHz increases as the rise time becomes shorter. UHF antennas, if designed properly, can achieve superior sensitivity with respect to direct measure approaches, and are thus the preferred measurement devices for PD testing. Fig. 2.14 from [51] shows the energy distribution of both switching disturbance and PD signal, highlighting the requirement of proper filtering to isolate the phenomenon.

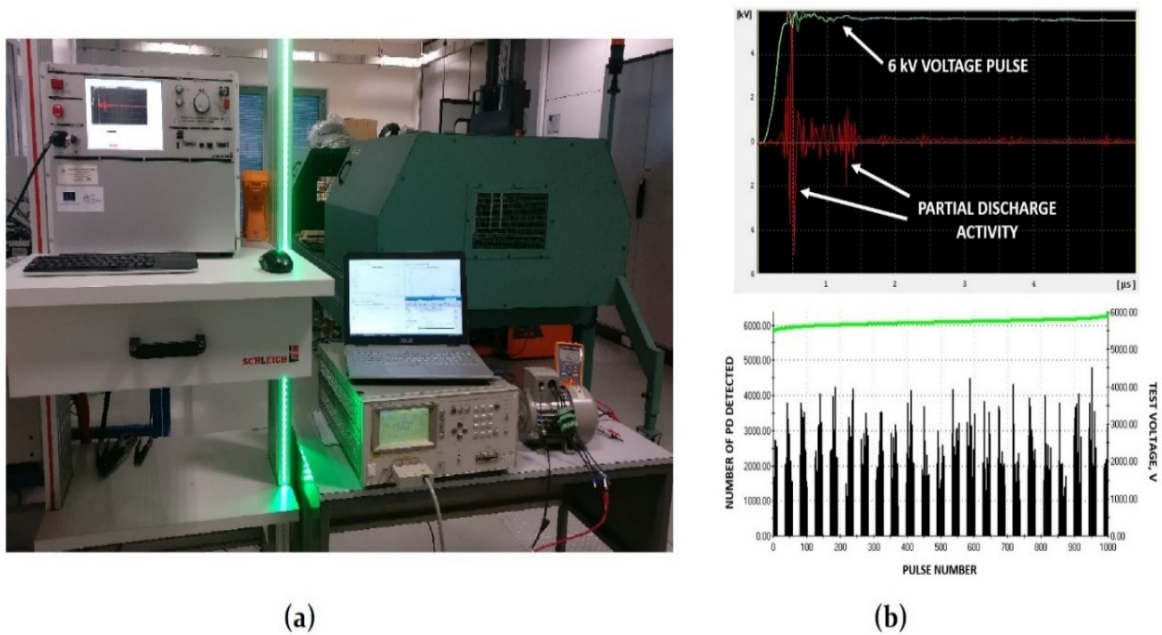


**Fig. 2.13** – Test setup for the measure of partial discharges in the winding insulation of a low-voltage machine using a winding analyser equipped with PD-coupler (a), and partial discharge activity data recorded after 1000 pulses at 6 kV (b).

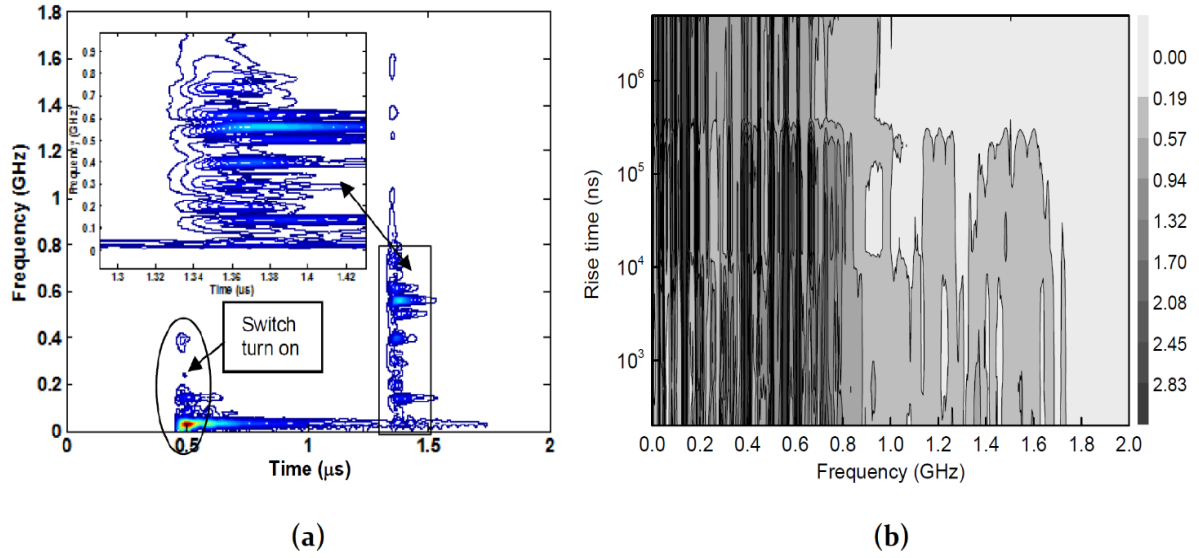


**Fig. 2.14** – PWM switching and partial discharge energy distributions (a), and variation of PD energy spectrum with pulse rise time (b). Source: [51].

#### 2.2.4. Effect of PWM characteristics on the properties of partial discharges

In this section, the main quantities and properties that can be used to describe the partial discharge activity in a winding insulation system are defined and then, according to the latest studies in the field, they are discussed in reference to the effects that the PWM characteristics have on them.

To fully characterize the PD activity occurring in an insulation system, the quantities listed below are defined in the technical standards and in the scientific literature. Current standards mainly focus on the definition of the PD inception and extinction properties to assess the goodness of an insulation. According to [48] the following are defined:

- *Partial discharge inception voltage (PDIV)*: is the minimum peak-to-peak voltage at which at least one PD event is registered, when the voltage is gradually increased until the first PD is registered.
- *Repetitive partial discharge inception voltage (RPDIV)*: is the minimum peak-to-peak voltage at which PD events are registered with a repetition rate of one or more every two voltage pulses.
- *Partial discharge extinction voltage (PDEV)*: is the maximum peak-to-peak voltage at which no more PD events occur, when the voltage is gradually reduced starting from the PDIV value.
- *Repetitive partial discharge extinction voltage (RPDEV)*: is the maximum peak-to-peak voltage at which PD events occur with a repetition rate of one or less every two voltage pulses.

Other than by its inception and extinction voltage levels, the intensity of PD activity can be quantified through the measurable characteristics of the single discharge. The following quantities are commonly used in the scientific literature to this purpose:

- *Magnitude*: is the measured amplitude of a single PD pulse expressed in volts or coulombs that gives a quantitative information of the intensity of a discharge event (Fig. 2.15a).
- *Delay time or occurrence time (PDOT)*: is the time interval measured between the instant of application of the voltage pulse (or the instant at which the voltage inverts its polarity, for bipolar pulses) and the first occurrence of a PD event within the same electrical period of the applied voltage waveform (Fig. 2.15a). It is mainly related to the statistical features of the PDs and to the memory effect of the space charge.
- *Repetition rate*: is the number of PD pulses counted within a single semi-period of the applied voltage waveform, it is another parameter that quantifies the intensity of the PD activity.
- *PD phase distribution pattern*: a graphical representation of the measured amplitude of each detected PD pulse with respect to the phase angle of the applied voltage waveform. This type of plot proves to be very useful to correlate the occurrence of PD events to the applied voltage. An example of this type of useful representation is shown in Fig. 2.15b from [52].
- *Firing voltage*: is the instantaneous voltage level at which the PD event actually occurs after a certain delay. The firing voltage has been found to have a direct influence on the magnitude of the partial discharge pulse, the higher the firing voltage, the more intense the PD.

Many recent studies have investigated the effects produced on PDs by various signals, especially PWM-type voltages. Most of the experiments reported in the literature is performed on specifically built laboratory samples consisting of two twisted insulated wires, with one or more point of contact. By employing such a system under test, the location of the occurring PD events can be easily controlled, and their properties accurately measured. The testing voltage waveform is applied across the sample by a high-voltage generator, which usually has some regulation capabilities in terms of pulse amplitude, duration, frequency, and rise time. The measurement systems are then connected to the sample or pointed in its direction in the case of UHF antennas. Proper filtering accessories are employed to isolate the frequency components of interest, and the results are recorded with a computer or a data logger. Short-circuit protections are also part of the system, to prevent damage to the equipment when the sample undergoes electric breakdown.

A PWM voltage waveform can be considered as a series of square wave pulses which duration is calculated by the comparison between a carrier signal, generally a triangular or sawtooth waveform at a certain frequency, and a modulating signal. The carrier signal controls the

switching frequency of the semiconductor devices, while the modulating signal determines the duration of each pulse. To achieve a certain level of control of the test conditions, the duration of the pulses is usually kept the same for all the pulses, i.e., a train of square wave pulses is used to investigate the effects on PDs. The main characteristics of a pulse that have a relevant impact on the properties of PD events are its amplitude, frequency, rise and fall times, and lastly its duty cycle, or better the duration of the pulse. Furthermore, distinguishing between unipolar and bipolar pulses is also important as evidenced by Kaufhold *et al.* in [53], where the probability of PD inception and the number of pulses to breakdown as a function of the pulse amplitude are compared for both unipolar and bipolar pulses. Bipolar pulses prove to be much more severe for the insulation to withstand, as evinced from the results in Fig. 2.16. In fact, for the type of insulation and materials investigated in the study, the probability of PD inception is about unity at 1.25 kV for bipolar pulses, while at least 1.5 kV are needed to reach 1% in the unipolar case. Similar results have been obtained in [54] and [55], where the PDIV of twisted-pair samples is investigated under both unipolar and bipolar pulses. The procedure employed by the authors in the latter study is to repeat the tests on the same sample many times in order to assess the variation of the inception voltage and of the PD characteristics as a function of the time under stress.

In the following, the effects of rise time, frequency, and duration of square-wave pulses on the properties of PDs and on life duration of insulation are discussed. The results summarized here can be mainly found in [56]-[62] where the role of PWM-type voltage waveforms on the aging mechanism is investigated from a statistical point of view taking into consideration different configurations and stress conditions.

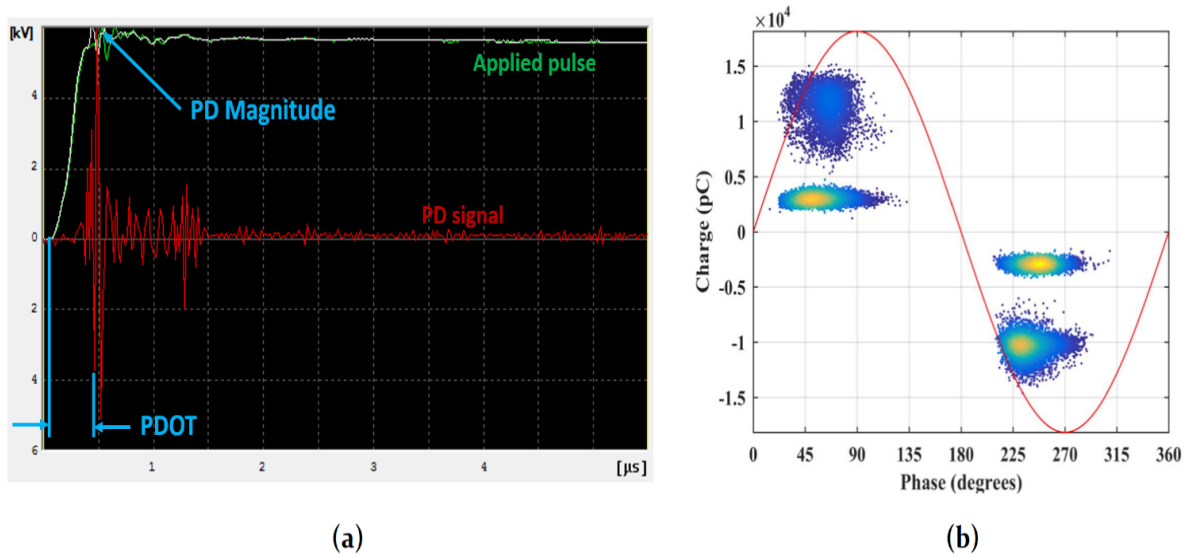


**Fig. 2.15** – Definition of PD magnitude and occurrence time (a) and example of a phase distribution pattern expressed in terms of measured charge from [52] (b).

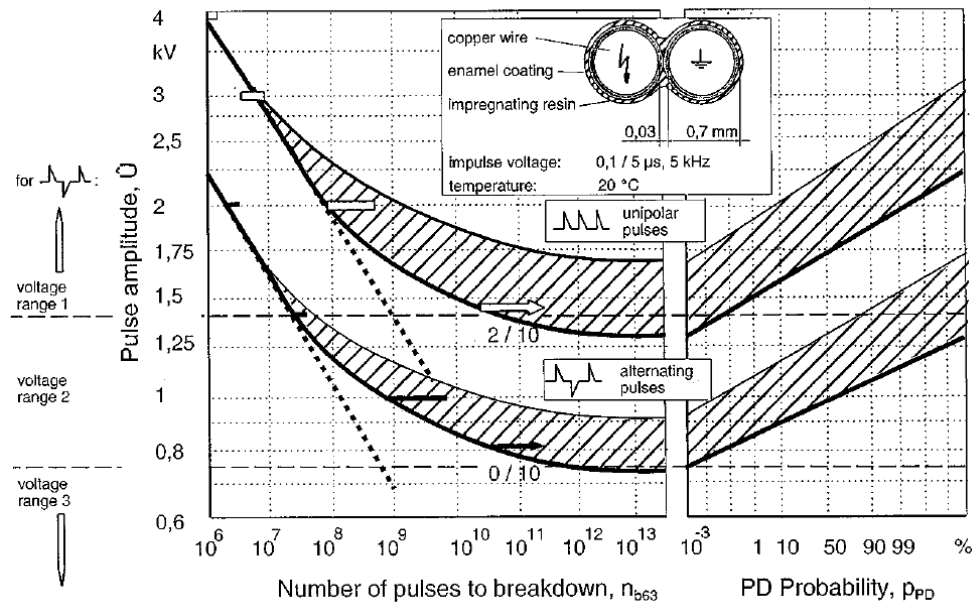


**Fig. 2.16** – Relationship between partial discharge inception probability and number of pulses to breakdown with voltage pulse amplitude in typical turn insulation. Source: [53].

### Effect of rise time

Pulse rise time can be defined as the time required for the voltage to grow from 10% to 90% of its full value. As deeply discussed in Section 2.2.1, the rise time of PWM pulses has a key role in determining the intensity of the overvoltage at the motor terminals by controlling the behaviour of the voltage waveform transmitting along the cable. When investigating how the rise time affects the characteristics of PDs, however, the effective voltage build-up time should be considered, i.e. the time required for the voltage applied directly to the motor to reach its full value, eventually the latter may be the full magnified voltage level. Sometimes, the voltage slew rate is used in place of the rise time as testing parameter. This substitution helps normalizing the results by introducing the dependency on the voltage magnitude in the equation.

The studies presented in the literature confirm, in general, that the shorter the rise time (i.e., the higher the slew rate), the larger the magnitude of the PD events. In particular, it has been found that both the firing voltage and the PD magnitude tend to increase with the slew rate following a linear trend in the logarithmic scale (Fig. 2.17), indicating the existence of a tendency to saturation with decreasing rise time. Slew rate, then, seems to act as a driver for higher firing voltages, which in turn lead to the inception of larger PD magnitudes. The explanation for the saturated trend is commonly associated with the stochastic nature of the mechanisms behind the generation of the first electron of the discharge. For high slew rates, the value of the firing angle tends to approach the voltage maximum level, so that PDs tends to occur on the flat part of the voltage square wave. Since PD magnitudes depend on the firing voltage at which they are incepted, this suggest why both firing voltages and PD magnitudes have a tendency to saturate. The same happen when the PDOT increases. However, by further studying the dependence of



PD magnitude on firing voltage it has been found that after a certain value, the relationship become more than linear. This phenomenon has been experimentally observed in [63]: PDs occurring at higher voltage tend to have lower residual fields, therefore the induced charge tends to increase, reflecting also on the peak value of the measured PD pulse.

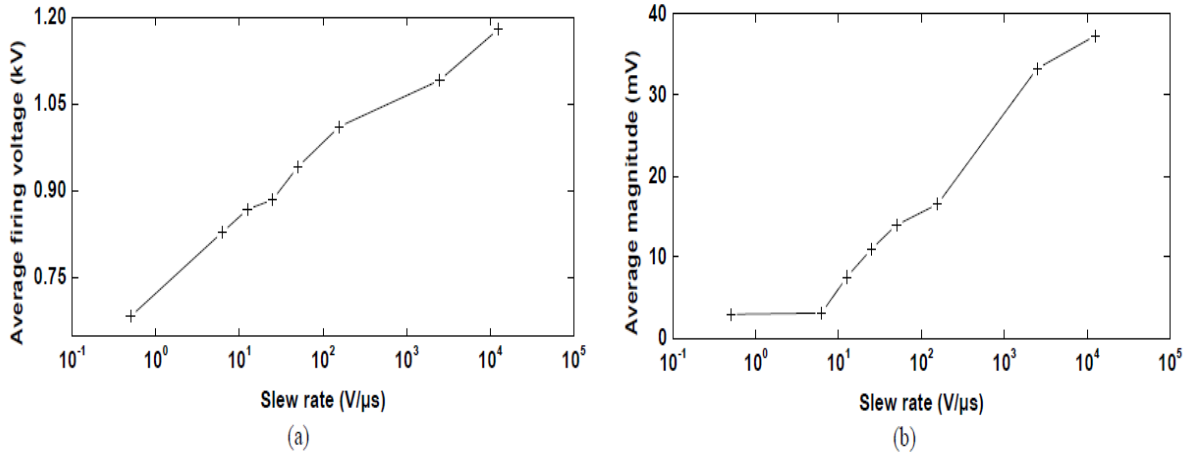


**Fig. 2.17** – Average firing voltage (a) and average PD magnitude (b) as a function of the slew rate of the applied voltage pulses. Source: [51].

The effect of rise time on the inception characteristics of PD has been investigated in many papers. However, the results are conflicting, some showing a positive trend, some depicting a negative trend, while others simply do not find any correlation. Speaking about repetition rate, however, some interesting findings help broadening the knowledge on the subject. With sinusoidal and long rise times, a certain number of low-intensity PD events occur in the insulation, but, when the pulse rise time is lower than 1 μs, then only one event occurs, of larger magnitude. Fig. 2.18 depicts the trend of PD magnitude and repetition rate as a function of pulse rise time. Considering that a rise times shorter than 1 μs is today the state of the art with modern power electronics, it can be assumed that each PWM pulse with a voltage level high enough incepts no more than one single discharge.

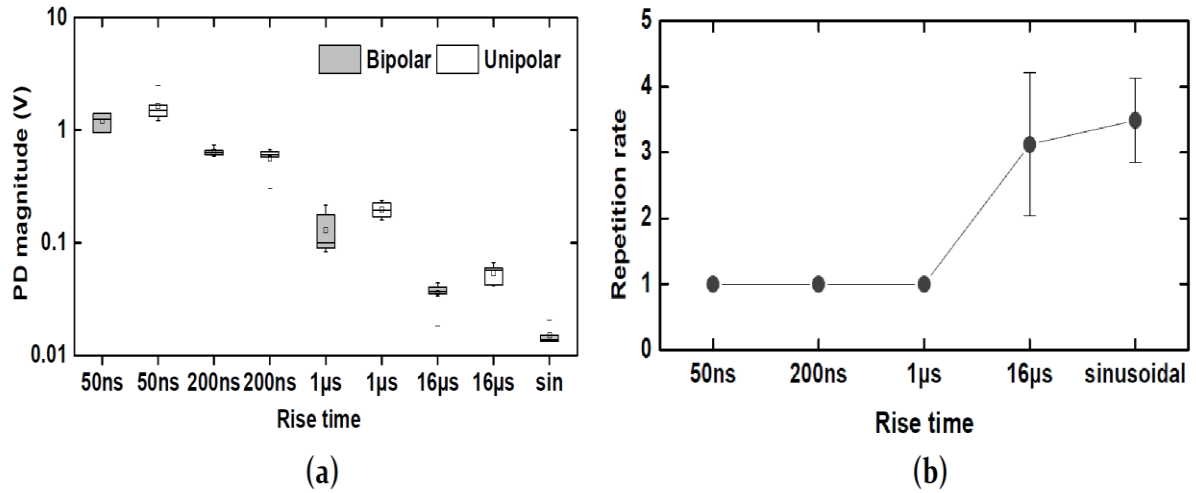


**Fig. 2.18** – PD magnitude (a) and repetition rate (b) as a function of the rise time of the applied voltage pulses. Source: [60].

### Effect of frequency

Fig. 2.19 shows that by increasing the frequency of the pulses, the PD magnitude and the PDOC tend to decrease. This can be explained by the fact that the higher the frequency, the shorter the pulse duration, and thus the more the amount of space charge that is still present within the defects due to the previous PD events. Consequently, the presence of space charge could favour the generation of initial electrons for a new avalanche to start at lower values for firing voltage, and thus with lower PD magnitude. The increasing in the number of discharges per second, however, is harmful for the insulation, so that even if the magnitude of the PD events is lower, their number will lead to a consistent amount of damage for the winding insulation. The studies presented in the literature are limited to frequency values of 2-5 kHz, while the effects of higher values that are more common in modern power electronics converters have not been investigated yet.

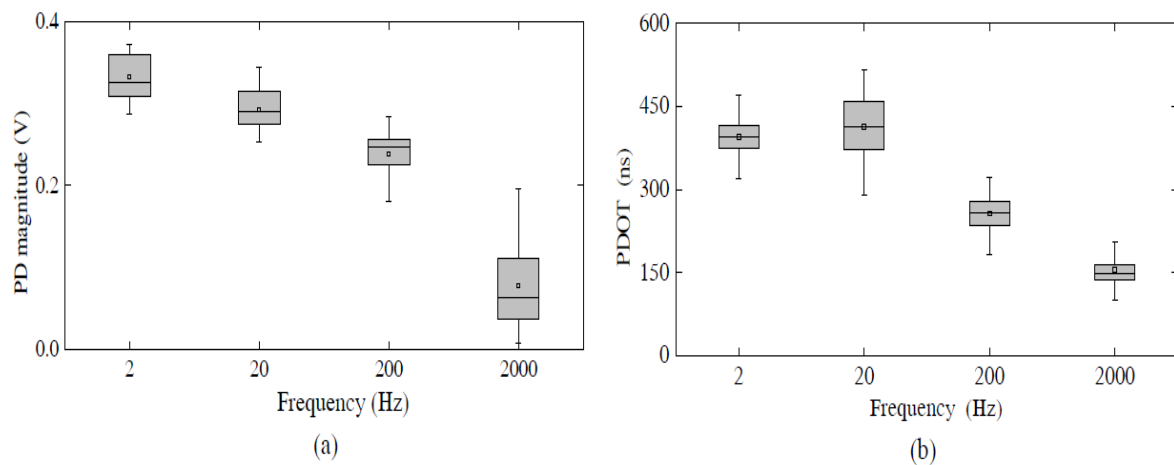


**Fig. 2.19** – PD magnitude as a function of the pulse frequency (a) and average PD magnitude correlated with the number of pulses to breakdown (b). Source: [58].

### ***Effect of pulse duration (duty cycle)***

The duration of a voltage pulse has an influence on the PD activity within the insulation. According to the findings in [59], when the duration is too low no PD are detected because the voltage on-time is not long enough to allow for the injection of initial electrons for the development of the discharge. The PDs seem to start around a pulse duration of 4-6  $\mu\text{s}$ . The PD magnitude increases as the duration become larger, up to a plateau around 100  $\mu\text{s}$ , shown in Fig. 2.20. The same behaviour is observable for the repetition rate, which is expressed in the figure as the probability of inception of a PD as a function of the pulse duration. According to the study, the value of 100  $\mu\text{s}$  seems to be a critical duration value, below and above which PD present different statistical features. This duration value could be the time needed to initiate steadily PD events at the test voltage, i.e. after this value one or more PD events can be observed at each voltage pulse, leading to relatively stable PD magnitude and PDOT. The conditions of the test performed in [59] that produced the above-discussed result are 2.7 kV peak-to-peak bipolar voltage, 50 Hz frequency, and 1  $\mu\text{s}$  rise time. Although these values are far from practical inverter operating conditions, they can prove useful to understand the phenomena governing the statistical features of partial discharges.

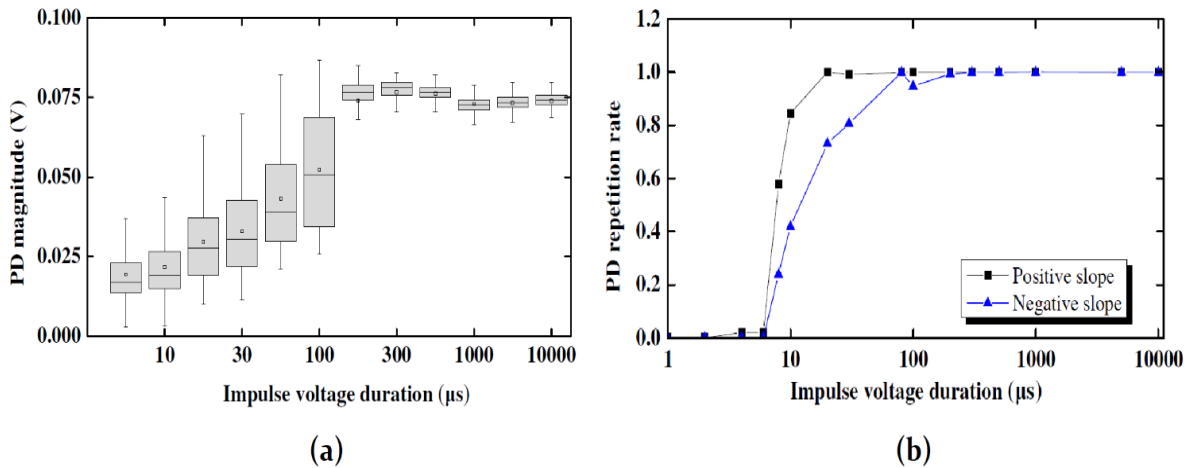


**Fig. 2.20** – Statistics of PD magnitude (a) and repetition rate (b) as a function of the voltage pulse duration. Source: [59].

### **2.3. Common Approaches to Prevent Insulation Aging**

As discussed earlier, the reliability problem in modern inverter-fed electric machine insulation is becoming more and more of a concern in many drive applications. Since the introduction in the market of the first switching devices, the need for up to date procedures to cope with this phenomenon has been demanding the periodic revision of the technical standards on the topic. Although many aspects are still not covered by current standards, numerous steps ahead have been done toward this objective. Insulation systems are classified according to their “PD-free” requirement, and prescriptions for the design and materials to be used are given

accordingly. Different testing procedures and methodological approaches for insulation life expectation assessment are proposed and still under improvement with the help of the scientific community. In practical application of electric drive and power electronic systems, meanwhile, different approaches have been employed to reduce the risk of insulation failure. The most common methods are briefly discussed in this Section, also focusing on the drawbacks that limit their use in certain types of application.

### **2.3.1. Inverter output filters**

A largely diffused solution to the problems related to the high  $dv/dt$ 's of modern drives is the use of filtering systems connected between the power electronics and the motor. A certain number of inverter output filters are commonly used in various applications, and more are still proposed in the scientific literature. The main types are listed below:

- Output line reactor: adding a series line reactor between the inverter and the motor increases the rise time of the voltage waveform. However, its benefits are not straightforward since the connection is beneficial only if the cable is relatively short; with long cables, the reactor may have no effect on reducing the overvoltage, but the peaks will last longer, increasing PD probability. Furthermore, the reactor may add resonance modes that can be harmful in certain operating conditions.
- Sine-wave filter: sine-wave filters are combinations of R, L, and C elements with a resonance frequency above the converter switching frequency. They can achieve nearly sinusoidal line-to-line voltage and remove current ripple. They are usually bigger than other types of filters and can drastically affect drive performance. An example of a sine-wave circuit is illustrated in Fig. 2.21a.
- $dv/dt$  filter (or PWM filter):  $dv/dt$  filters are LC circuits, such as the one shown in Fig. 2.21b, which are designed to reduce the steep slope of the PWM voltage pulses. The resonance frequency of the LC circuit is chosen to be above 2 times the switching frequency of the converter. They are ideal for high-performance applications.
- RC filter at motor terminals: at high frequency, the capacitor behaves as a short circuit absorbing the HF components caused by the steep  $dv/dt$ . Wave reflection is not caused by the filter if the value of the resistance is chosen equal to the impedance of the cable. Usually the additional losses can be limited since the current flows only during the rising and falling flanks of the voltage. The benefits, however, are limited and the losses may be higher at high switching frequency.
- Common-mode reactor: the capacitive current produced by the steep PWM pulses can be reduced by installing a common-mode reactor. Such a choke has proven effective in reducing the peak value of the homopolar leakage current, but not in reducing its mean and RMS values. Its presence in the zero-sequence circuit increases the impedance of this network and must be properly designed depending on application requirements.

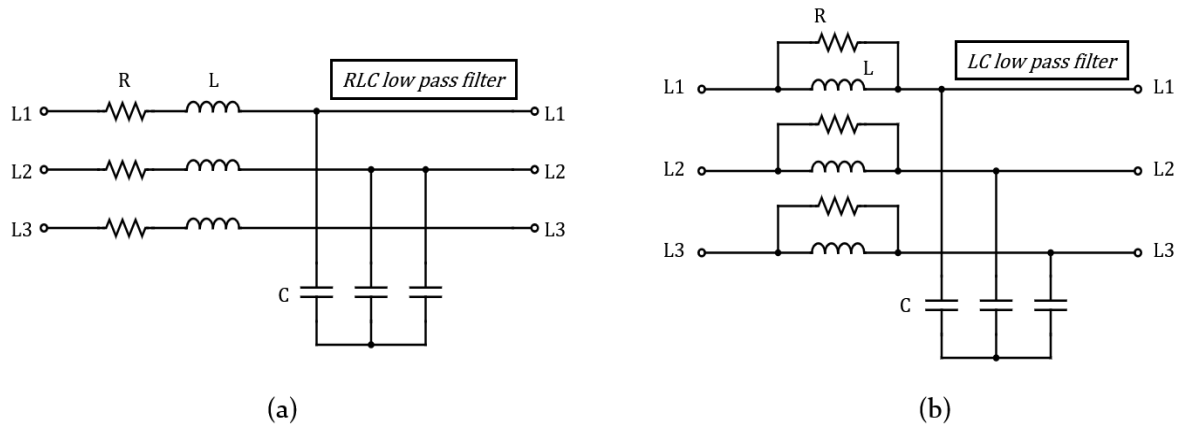


**Fig. 2.21** – Circuit diagrams showing the structure of a sine-wave low-pass filter in series RLC configuration (a) and of a  $dv/dt$  filter in LC connection (b).

A comparison between sine-wave filters and  $dv/dt$  filters in terms of their beneficial effects on drive performance is made in [64] and reassumed in Table 2.I. The authors conclude in the analysis that, while not using inverter output filters is impractical for most applications, sine-wave filters are the best choice for drives, with  $dv/dt$  filters being suitable only when fast dynamic performance is required.

**Table 2.I** – Comparison of filtering solutions for inverter-fed AC drives. Source: [Shackwhe\_1998].

<i>Effect</i>	<i>No filter</i>	<i><math>dv/dt</math> filter</i>	<i>sine-wave filter</i>
<i>Motor <math>dv/dt</math></i>	High	Acceptable	Low
<i>Motor insulation</i>	Must be increased	Normal	Normal
<i>EMC</i>	Very high	Low	Very low
<i>PWM carrier at motor</i>	100%	100%	Low
<i>Motor audible noise</i>	High	Slightly decreased	Decreased
<i>Motor derating</i>	Approximately 13%	Approximately 3%	None
<i>Torque response</i>	Fast	Fast	Slower
<i>Motor cost</i>	Typically, +10%	No extra cost	No extra cost

The use of inverter output filters to reduce the stress on motor insulation has some consequences on the performance and cost of the drive:

- Increased weight and volume of the system
- Increased cost
- Additional losses and voltage drop
- Derating of power switches due to current circulation between filter components and DC-link
- Derating of motor dynamic performance due to the delay introduced by the filter
- Potential auto-excitation of induction motors
- The resonance frequency of the filter needs be carefully considered in designing the drive control system

Furthermore, it is worth mentioning that, in order to achieve compensation of different phenomena (i.e. lower motor stress, EMI, common-mode current circulation, etc.) different filter topologies are required, and installing many different filters is unpractical for an electric drive. Alternatively, simpler filter structures require complex control features to be added to be used effectively on a multi-purpose way.

### ***2.3.2. Co-design of power electronics and motor***

To avoid the installation of long cable between the motor and the inverter, and thus drastically limit the overvoltage problem at motor terminals, a common approach mainly diffused in industry is the so called “co-design” of inverter and motor, consisting in combining both systems in a compact solution, with very short cable length (Fig. 2.22). Among the advantages of this solution are the high compactness, the very short cable length, and the optimization of the combined design of the drive, with no necessity for extra inverter installation and plug-and-play feature. However, some limitations and drawbacks may limit the application of this solution in many applications.



***Fig. 2.22 – Example of inverter-motor combined design.***

First, the different scaling of inverter and motor makes it difficult to use this approach for high-speed machines. While electric machines scale with the torque, in fact, converter size is proportional to the power. Low-speed motors are relatively large with respect to power, then the integration of the converter is easy. High-speed machines, however, remain small if the speed is increased with the power, so that the converter integration is not straightforward. Furthermore, positioning the converter on top of the motor makes it subject to increased vibrations and heat exposure, so that further measures need to be taken to preserve reliability, but increasing size and cost.

### *2.3.3. Corona-resistant materials*

Over the past years, manufacturers have developed new insulation materials to cope with the increased stress induced by power electronics converters. These new materials are designed with the intent to be more resistant to the effects of repeated partial discharge activity and increase the life of the winding. They are commonly referred to as “corona-resistant” material, from the name that is sometime incorrectly given to partial discharges (corona is, in fact, only a subtype of discharge, which is visible due to radiation emission in the visible spectrum). These materials are obtained by mixing inorganic composites with common organic insulation materials that are commonly used for direct-on-line motors. The efficacy of corona-resistant material has been studied in [65] in comparison with a standard polyamide-imide material, showing lower PDIV values and longer life under different temperature values. Modern standards suggest the use of organic-inorganic insulation materials for inverter-fed electric machines. The main drawback is, however, the increased cost of the machine. The effectiveness of these materials in withstanding the stress in systems based on WBG semiconductor devices has not been tested extensively yet.

## Chapter 3 Study on the Effects of Electrical Aging on Winding Insulation and Its Estimation

In the previous chapter, the main phenomena that are responsible of partial discharge inception, and the main aging mechanisms in PWM-fed motor insulation systems have been introduced. In a nutshell, high switching frequency and  $dv/dt$ 's may reduce drive reliability by shortening the lifetime of the insulation, which is a concern in all those fields where availability is of the utmost importance, for either safety (e.g. aerospace or ground transportation areas) or economic reasons (e.g. industry).

In this scenario, the aim of this research is twofold. On the one hand, it aims at studying the effects of high-frequency, steep PWM voltage waveforms on the degradation of the winding insulation system of random-wound AC motors. On the other hand, the possibility of aging estimation through the measure of easily obtainable electrical quantities is investigated by developing and comparing three aging indicators. The novel contribution consists in the original approach to this kind of study. The methods of analysis employed in the literature in this field, in fact, can be roughly classified into two types. A first group of papers focuses on the analysis of the microscopic effects that are produced by PDs on very simple systems (i.e., either twisted magnetic wires or insulation bulks with appositely-made defects of known geometry), in which a single discharge event can be more easily observable and its physical and chemical features measurable [66], [58], [46]. On the other hand, a second group of works presents the analysis of macroscopic effects that are observable in more complex systems (i.e., from single high-voltage motor bars to entire random-wound coils or stators), but only investigates the effects of thermal aging [67], [68]. Finally, [69] propose an off-line analysis method that is tested through the simulation of the aging of the machine. None of the previous works has carried out an analysis of the macroscopic effects produced on complex systems, such as random-wound motor windings, by electrical aging. This chapter of the thesis presents the results of an accelerated electrical aging campaign on three random-wound motors showing how it can affect some macroscopic quantities. The aim in this study is not to bring the system to final breakdown, but to investigate the role of the phenomena discussed in the previous chapter in a realistic application, such as that of a low-voltage AC motor fed by high-frequency PWM voltage pulses. To this purpose, different methods are adopted to study the consequences of such steep PWM waveforms on the health status of a random-wound winding. In particular, since the parasitic capacitive nature of the winding insulation is predominant to the inductive behaviour of the machine in the high-frequency domain, the presented approaches focus on the HF characteristics of the machine. The first method analyses the variation of the HF characteristic impedances of the machine under test (MUT). A second approach focuses on the observation of the HF components of the phase current and its frequency spectrum. The advantages and downsides of the different approaches are then highlighted to compare the capability to detect the progressive damage caused on the motor winding insulation by the aging campaign.



### 3.1. Description of the Experimental Setup for the Accelerated Aging Test

The machines that have been tested for this study are three identical low-voltage, general-purpose induction motors, with random-wound stator construction. The rated parameters of the motors are listed in Table 3.I. A schematic representation of the rig used for the accelerated aging experiments is depicted in Fig. 3.1. A picture of the experimental setup is shown in Fig. 3.2.

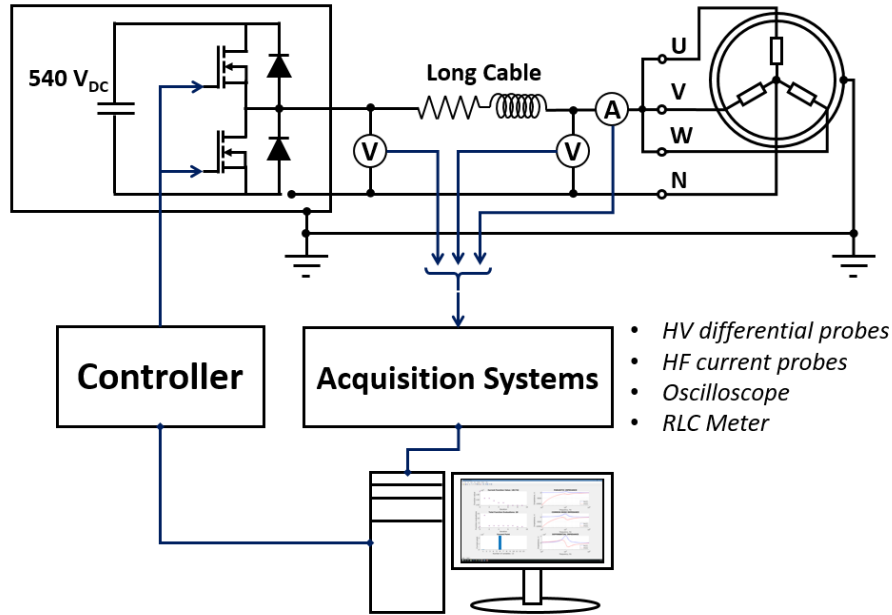


*Fig. 3.1 - Schematic structure of the experimental bench employed for the electrical aging procedure.*

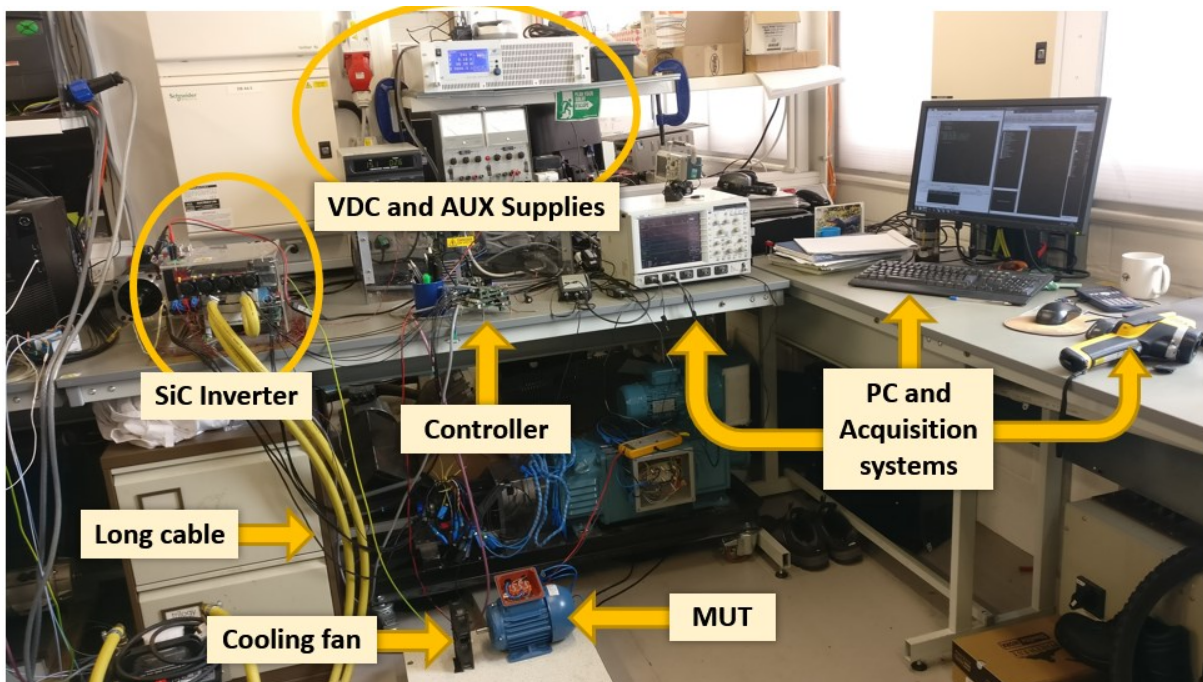


*Fig. 3.2 - Photo of the experimental rig used to perform the electrical aging procedure.*

**Table 3.1** – Rated parameters of the motor under test

Parameter	Unit	Value
Output power	kW	0.37
Full load speed	rev/min	1370
Voltage (Y/ $\Delta$ )	V	230/400
Rated current (Y/ $\Delta$ )	A	1.93/1.11
Locked rotor current	p.u.	3.6
Full load torque	Nm	2.58
Insulation class (temp. rise)	- (K)	F (80)

The experimental bench consists of a SiC-MOSFET inverter connected to the MUT through a 30-meter-long cable to magnify the voltage reflections at the motor terminals, a controller to drive the inverter gates, a PC to handle the tests, and various system to perform acquisition of voltage, currents, temperature, etc. Fig. 3.3 shows a flow chart detailing the steps followed for the aging tests.

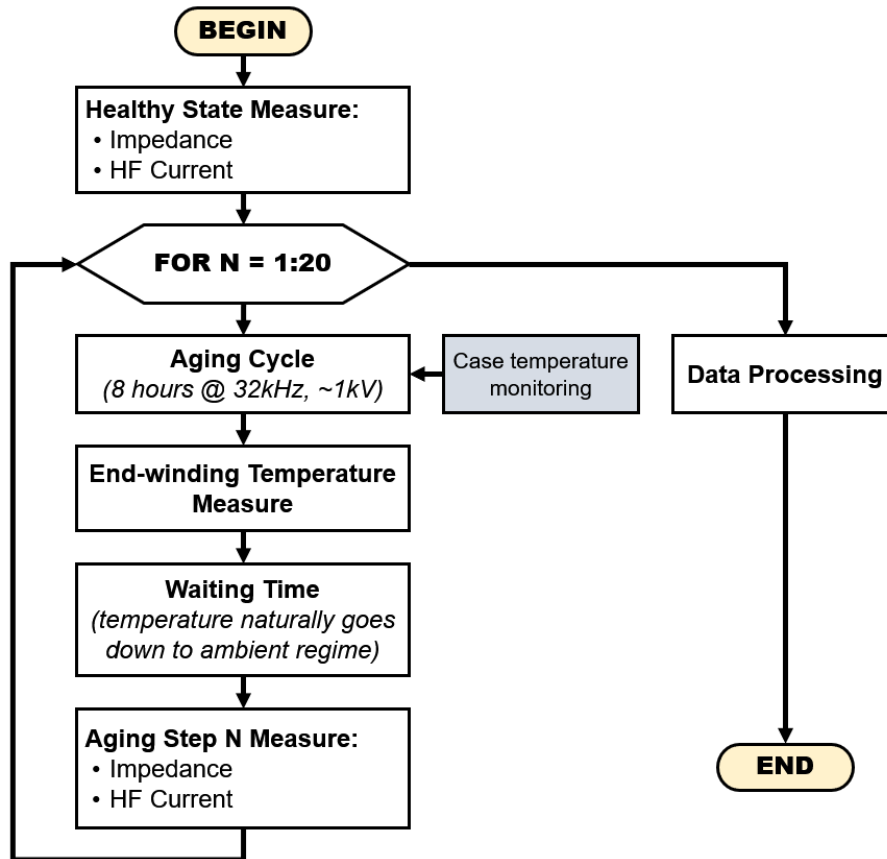


**Fig. 3.3** - Flow chart detailing the routine followed for the tests.

The first step of the aging campaign is the measurement of the HF characteristics of the MUT when the insulation condition is healthy, an information that will be then used as a reference for the estimation of the aging effects. Then, the first aging cycle is initiated. The MUTs are random-wound machines of 0.37 kW rated power, with class F insulation (155 °C maximum

temperature), connected in star configuration with the neutral made accessible. During the electrical aging procedure, the inverter is operated with a DC-link voltage of 540 V and a switching frequency of 32 kHz. The PWM pulses are applied between the motor phase terminals connected in parallel and the neutral (i.e. the three-phase windings are connected in parallel). Each aging cycle lasts for 8 hours, therefore a total of 921.6 million pulses are applied uniformly to each phase during each cycle. The voltage waveforms at the inverter output and at motor terminals are shown in Fig. 3.4a. The rise time of the inverter voltage pulses is around 70 ns, producing a peak overvoltage on the motor of 980 V and a voltage ringing lasting about 20  $\mu$ s. After the aging cycles terminates, the MUT is left unsupplied for one night, in order to let the temperature naturally settle to the ambient regime. The measurement procedure to register the HF characteristics of the machine after the aging step is performed in the morning. The details about the measurements are presented in Section 3.2. Then, a new aging cycle is started and the routine repeats until the selected number of cycles is reached. To avoid undesired thermal effects that could affect the results of the study, it is important to ensure that the temperature of the motor winding lays well below the critical value of the insulating material (i.e., 155 °C in this case). For this reason, a few measures have been taken to prevent that thermal damage overlaps to the effects of the electrical discharges during the aging procedure. First, the aging cycles are performed at a constant duty cycle equal to 7% in order to limit the RMS current absorbed by the motor below the rated value. Moreover, the MUT is externally cooled with forced ventilation to improve heat dissipation. The temperature of the motor case has been regularly monitored during the aging procedure using a thermographic camera. After a few hours of aging, the case temperature is around 40 °C, as shown in Fig. 3.4b. It has been verified that in this condition the winding temperature is around 55-60°C, well below the critical limit of the material. As an additional verification, the end-winding temperature has been measured after a couple of minutes from the end of each aging cycle, after removing the case front closure. Its value has always been around 55 °C.

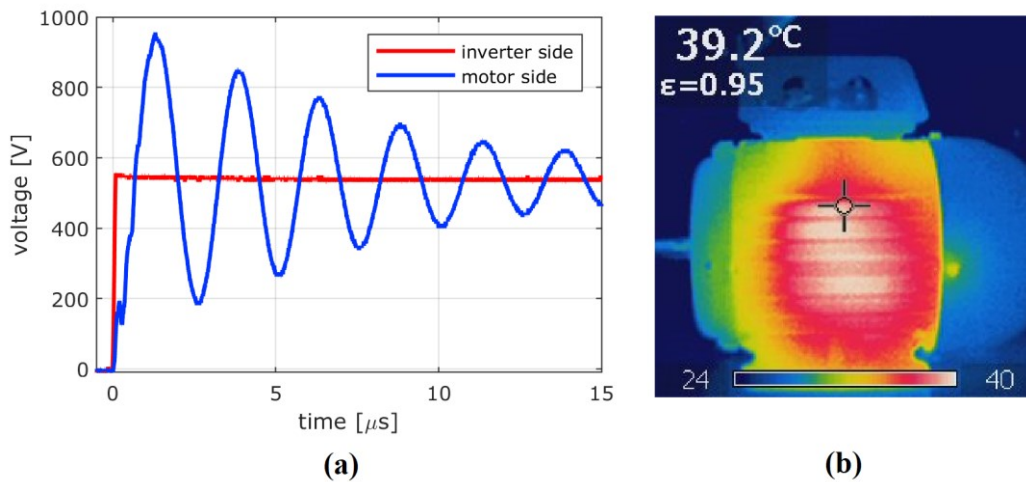


**Fig. 3.4** - Experimental overvoltage at motor side (a) and temperature on the motor case during an aging cycle, measured after a few hours from cycle start (b).

### 3.2. Methodologies for the Estimation of Aging Effects

As discussed above, the parasitic capacitances introduced by the insulation system of the machine dominate its inductive behaviour in the high-frequency domain. These capacitances are determined by the structure and properties of the insulating material between the conductors, or between the conductors and the stator iron, which is grounded. Consequently, a degradation of the insulation properties affects the equivalent value of the parasitic capacitances and can be observed in the machine high-frequency behaviour. To this purpose, after each electrical aging cycle, the effects of the electrical stress on the motor winding insulation can be investigated by analysing its HF characteristics. These characteristics are evaluated from the measurement of the machine response both in the frequency and in the time domains, i.e. by acquiring the motor characteristic impedances as a function of the frequency, and by analysing the current response to a steep voltage pulse applied between the phases.

#### 3.2.1. *Estimation through motor high-frequency characteristic impedances*

An impedance analyser has been employed to measure the machine impedance in a wide frequency range. It can span a frequency range between 100 Hz and 40 MHz, with high accuracy and repeatability of the measures. Three characteristic impedances can be defined according to the relative connection of the machine terminals to the instrument for the measure. The common mode impedance is measured between the three phase terminals shorted together and the ground terminal, while the neutral is floating. The differential impedance is measured between the three phase terminals shorted together and the neutral, while the ground terminal is floating. Finally, the parasitic impedance is measured between the three phases and the neutral shorted together and the ground terminal. A scheme detailing the connection of the motor to the instrument for the impedance measurement is depicted in Fig. 3.5.

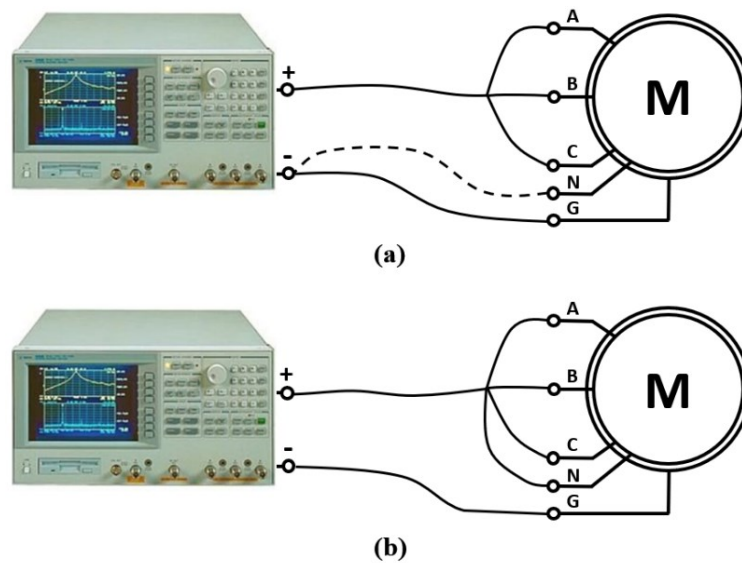


**Fig. 3.5** - Connection of the motor to the impedance analyser for the measurement of the common mode and differential impedances (a), and of the parasitic impedance (b).

The common mode, differential, and parasitic impedances of one of the MUT as a function of frequency are shown in Fig. 3.6, Fig. 3.7, and Fig. 3.8, respectively. For each figure, the healthy insulation state and the measures taken after a few aging cycles are compared.

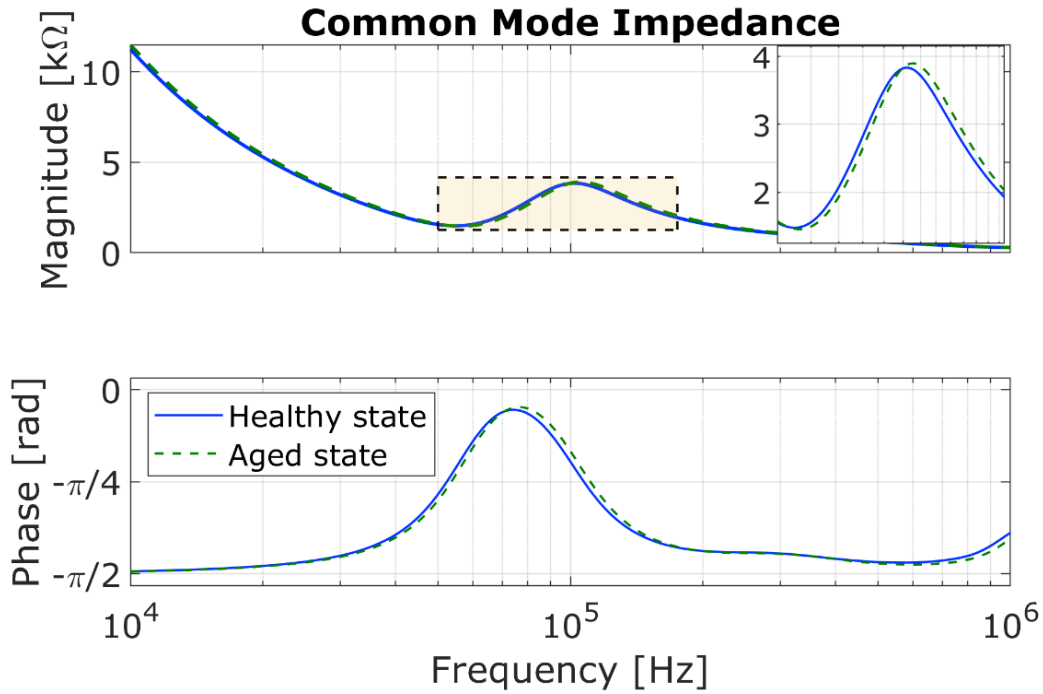


*Fig. 3.6 - Common mode impedance: comparison between healthy and aged insulation state.*

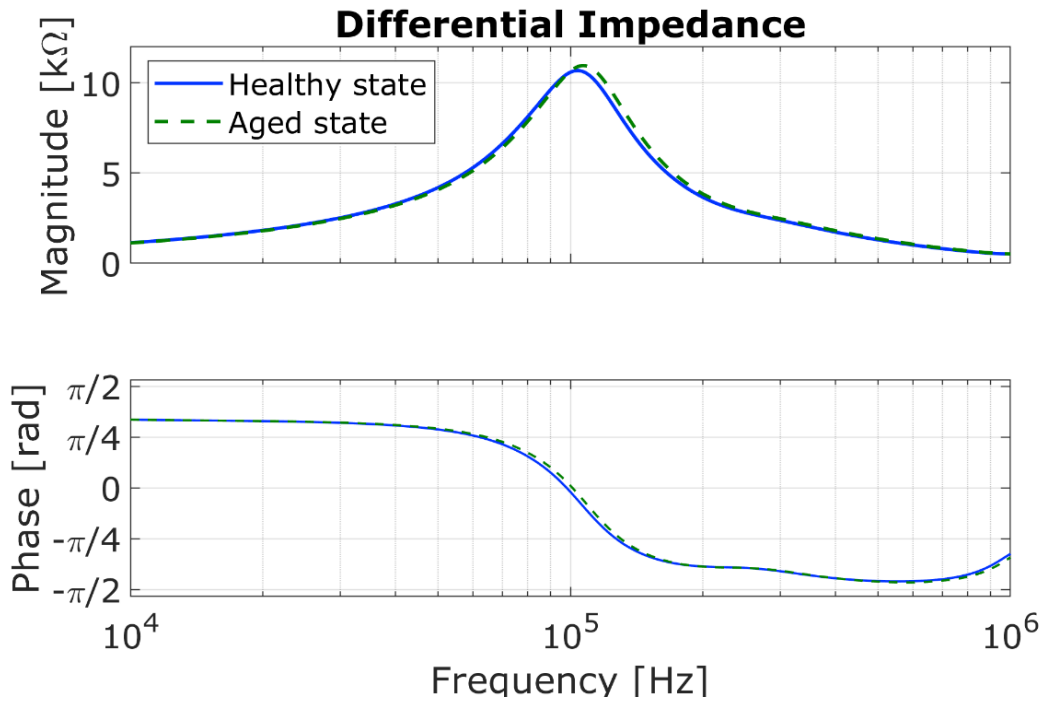


*Fig. 3.7 - Differential impedance: comparison between healthy and aged insulation state.*

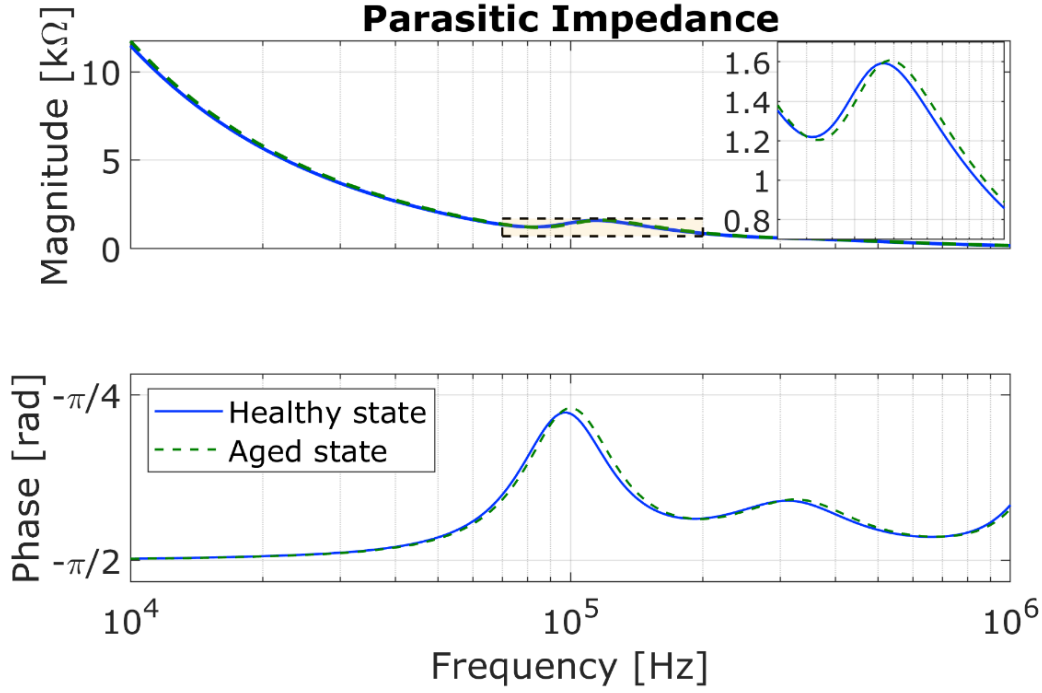


**Fig. 3.8** - Parasitic impedance: comparison between healthy and aged insulation state.

The characteristic impedances of an electric machine have typical shapes, with the relevant information being generally contained in the frequency range between 10 kHz and 1 MHz. At low frequency, the parasitic and common mode impedances have a highly capacitive nature (the phase is near to  $-\pi$ ), with large magnitude mainly because of the insulation that blocks current dispersion from the winding to the motor case. With the frequency increasing, the imaginary part of the impedance decreases sharply until, around 100 kHz, a resonance peak is determined by the interaction with the coil inductance in the common mode path of the current. At the very high frequencies, the behaviour is again highly capacitive, since the turn-to-turn and the turn-to-ground capacitances are the minimum impedance path for the HF currents. The differential impedance has, instead, an ohmic-inductive behaviour at low frequency, which becomes capacitive after the resonance peak, when the turn-to-turn parasitic capacitances become the minimum impedance path for current circulation. It is worth noticing that the differential impedance is the one that the inverter actually “sees” in each switching condition. In each of its states, in fact, the switches are always set so that a phase of the motor is in series with the parallel of the other two.

As can be seen in Figs. 3.6, 3.7, and 3.8, with the progression of the insulation aging, the amplitude and position of the resonance peak slightly change. Therefore, it is possible to calculate an index that measures this displacement after each aging cycle to track the effects of the electrical stress on the insulation. The index employed in this paper is calculated as the root mean square deviation (RMSD) between the healthy state and the considered aging state. It is referred to as impedance deviation and denoted as  $d_z$ .



$$d_{Z,j} = \sqrt{\frac{1}{n} \sum_{k=1}^n w(k) \cdot [Z_0(k) - Z_j(k)]^2} \quad (3.1)$$

In (3.1),  $n$  is the number of measurement points,  $Z_0(k)$  is the module of the healthy state impedance at the frequency  $k$ , and  $Z_j(k)$  is the module of the impedance after  $j$  aging cycles at the frequency  $k$ .  $w(k)$  is a weighting function with values between 0 and 1 that is used to limit the calculation to the frequencies of interest (in this case, it is a rectangular function with value 1 between 10 kHz and 1 MHz).

A second version of this index can be defined as the RMSD between an aging state and the previous one, i.e. substituting  $Z_{j-1}(k)$  for  $Z_0(k)$  in (3.1). The information given by this index can be useful to highlight the entity of the change between two consecutive cycles, regardless of the direction, and is therefore referred to as differential impedance deviation and denoted as  $d_Z^D$ . Finally, an integral impedance deviation ( $d_Z^I$ ) can be calculated as the sum of the differential deviations after each aging cycles and can be useful to track the evolution of the impedance with the time.

### 3.2.2. *Estimation through analysis of high-frequency currents components*

The steepness of the PWM voltage pulses excites the high-frequency modes of the armature winding. As a result, the current that the motor absorbs in response to a single voltage pulse presents an initial high-frequency transient superimposed to the slope proportional to the machine low-frequency reactance. In order to capture this high-frequency transient, the current of one of the phases is recorded by mean of a Rogowski coil connected to a GPIB-programmable digital oscilloscope. The current probe that has been employed has a peak  $di/dt$  of 20 kA/ $\mu$ s and a bandwidth of 20 MHz. The Rogowski probe is shielded within an earthed aluminium box to prevent electromagnetic interference during the measure. Its position is fixed in the box in order to acquire the current response in the same position during each measure. 50 scores are taken for each aging state with the purpose of making some statistical considerations on the results. For each score, a voltage step of 540 V is applied to the winding of the machine and maintained for about 80  $\mu$ s. The rising flank of the voltage step triggers the acquisition on the oscilloscope, and the current data points are recorded in a window of 50  $\mu$ s at a sample rate of 500 MS/s. The trigger delay is set to 5  $\mu$ s, so that an adequate number of samples around zero current is available to correct the acquired data from the offset of the probe. As a result, the net observation window useful for the high-frequency transient analysis is equal to 45  $\mu$ s. Fig. 3.9 shows a schematic timing diagram of the measuring procedure of one score. Considering the very short duration of the applied voltage pulse and the relatively large time required to transfer the acquired data samples from the oscilloscope to the PC (around 10 s in total), it can be assessed that no temperature variations affect the outcome of the measure during this procedure.

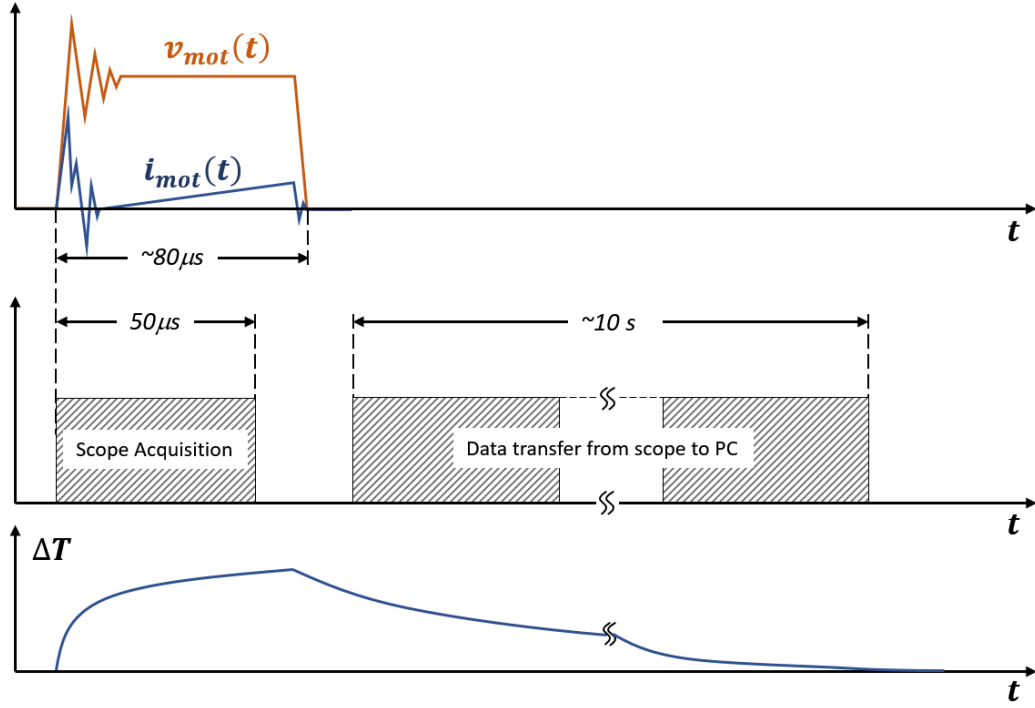


**Fig. 3.9** - Schematic timing diagram of the high-frequency current measurement procedure.

The current waveforms averaged over the 50 scores, for the healthy and for an aged insulation state are shown in Fig. 3.10, which also includes a detail of the first 1  $\mu\text{s}$  from the application of the voltage step. The high-frequency transient changes as the motor undergoes the aging process, are related to the capacitive behaviour of the motor, and thus to the insulation properties. For this reason, the deviation of the current from the healthy state of the machine can be used to derive an index of the degradation of the insulation, similarly to what is done with the characteristic impedances. The current deviation  $d_i$  can be calculated, for each aging step, as the average RMSD with respect to the healthy state

$$d_{i,j} = \text{mean}_s \left\{ \sqrt{\frac{1}{n} \sum_{k=1}^n w(k) \cdot [i_0^{avg}(k) - i_{j,s}(k)]^2} \right\} \quad (3.2)$$

where  $n$  is the number of samples of the current waveform,  $i_0^{avg}(k)$  is the  $k^{\text{th}}$  sample of the current at the healthy state, averaged over the total number of scores, and  $i_{j,s}(k)$  is the  $k^{\text{th}}$  sample of the score  $s$  of the current acquired after  $j$  aging cycles.  $w(k)$  is a weighting function with values between 0 and 1 that is used to limit the calculation to the time interval of interest (in this case, it is a rectangular function with value 1 between 0 and 25  $\mu\text{s}$ ). As for the impedance deviation, it is also possible to define a differential current deviation ( $d_i^D$ ) and an integral current deviation ( $d_i^I$ ) to highlight the entity of the variation regardless of its direction.



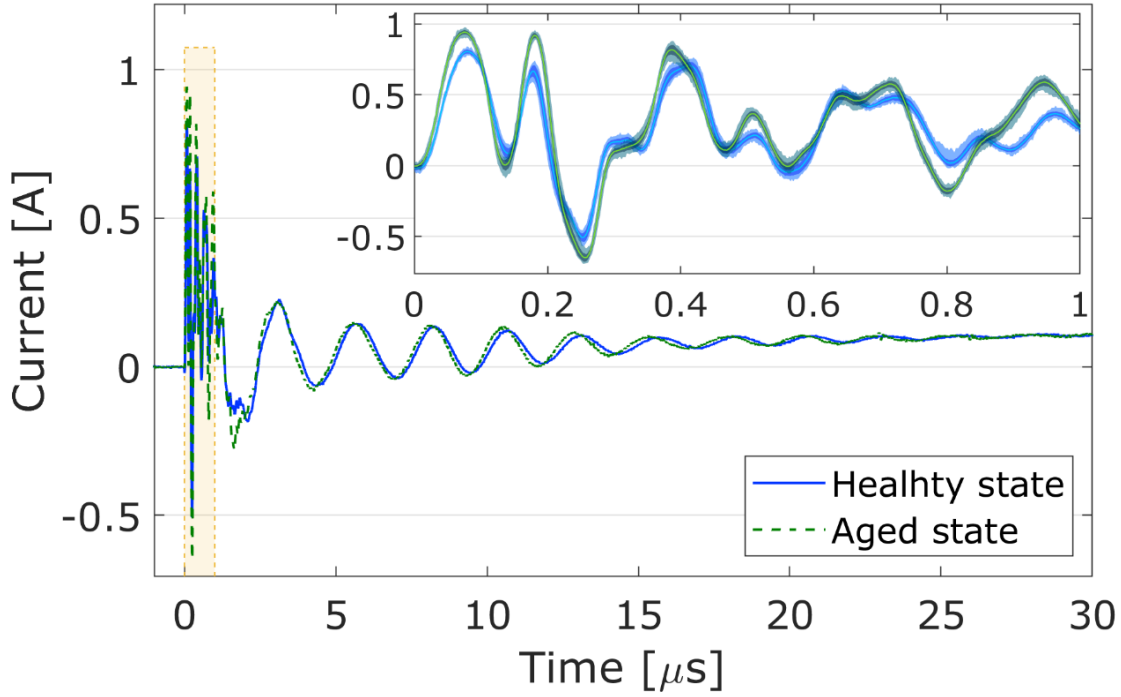


**Fig. 3.10** - Current in phase U measured after applying a voltage step for two different aging states. The detail shows the maximum and standard deviations of the measure.

In order to gain a better visualization of the variation in the frequency domain, a Fast Fourier Transformation (FFT) algorithm is used. Fig. 3.11 shows the spectra obtained from the same aging states that are shown in Fig. 3.10, averaged over the 50 scores. The major difference caused by the aging process occurs in the range from 500 kHz to 10 MHz, confirming the results observed in the current transient. Like the high-frequency currents, also their spectra can be compared to evaluate an index of the insulation degradation. This index, called insulation state indicator (ISI), was firstly proposed by Zoeller *et al.* in [67] for diagnosis purposes. In this paper, in accordance with the other indices proposed, it will be referred to as spectrum deviation ( $d_Y$ ). Its calculation is as in (3.3).

$$d_{Y,j} = \text{mean}_s \left\{ \sqrt{\frac{1}{n} \sum_{k=1}^n w(k) \cdot [Y_0^{avg}(k) - Y_{j,s}(k)]^2} \right\} \quad (3.3)$$

Here,  $n$  is the number of harmonics of the current spectrum,  $Y_0^{avg}(k)$  is the  $k$ -th amplitude of the current spectrum at the healthy state, averaged over the total number of scores, and  $Y_{j,s}(k)$  is the  $k$ -th amplitude of the current spectrum of score  $s$ , acquired after  $j$  aging cycles.  $w(k)$  is a weighting function with values between 0 and 1 that is used to limit the calculation to the frequency interval of interest (in this case, it is a rectangular function with value 1 between 500 kHz and 10 MHz). It is important to properly select the calculation window because, above a certain frequency, the spectrum is influenced by the measurement noise of the probe, which

could lead to a poor interpretation of the results. Moreover, before calculating the FFT on the current signal, it is necessary to remove the constant inductive slope that can be noticed in Fig. 3.10, since it affects the correctness of the results. A differential spectrum deviation ( $d_V^D$ ) and an integral spectrum deviation ( $d_V^I$ ) are also defined, as for the previous cases.

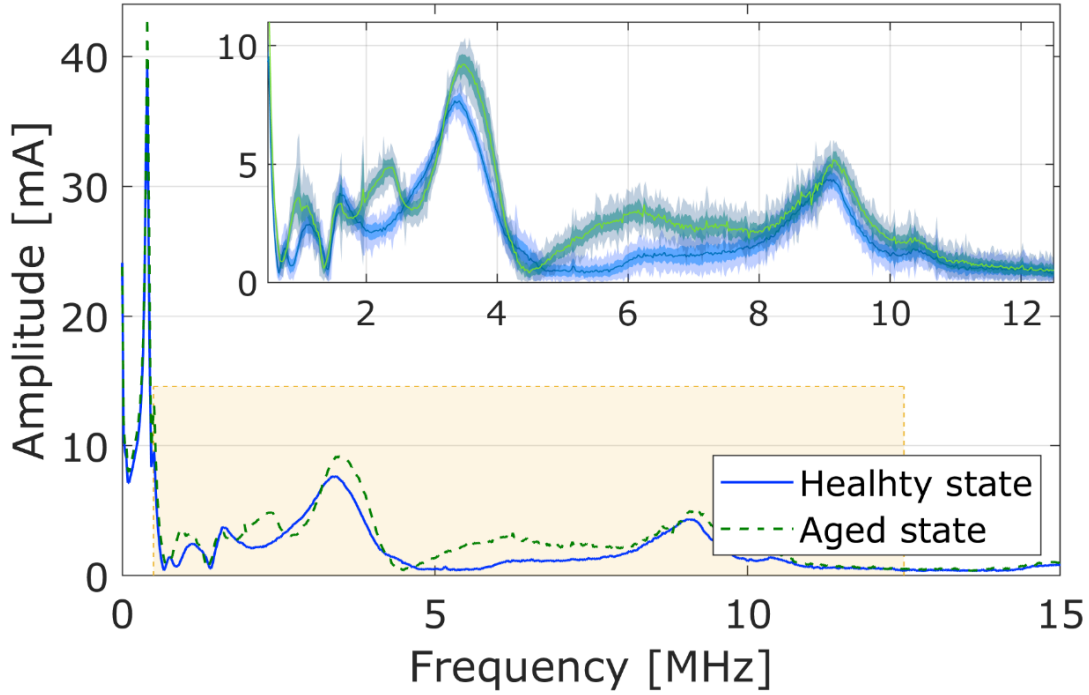


**Fig. 3.11** - Spectrum of the currents for two different aging states and a detail of the frequency range of interest for the calculation of the deviation.

In order to verify that the variation observed in the high-frequency current transient is actually due to the effects of aging, the maximum and standard deviation bands are also depicted in Fig. 3.10 for both aging steps. As it can be noticed from the figure, the measurement accuracy and repeatability are quite good, thus letting a proper comparison of the scores with the purpose of quantifying the insulation degradation. Fig. 3.12 shows the distribution of all the samples of HF current that have been acquired, normalized with respect to their mean values. The standard deviation calculated considering all the samples is equal to 35 mA, thus confirming the goodness of the measure. The same analysis has been performed on the FFT data, obtaining a standard deviation value of about 3 mA. This verification confirms that the measures are accurate enough to discern small variations on the HF characteristics.

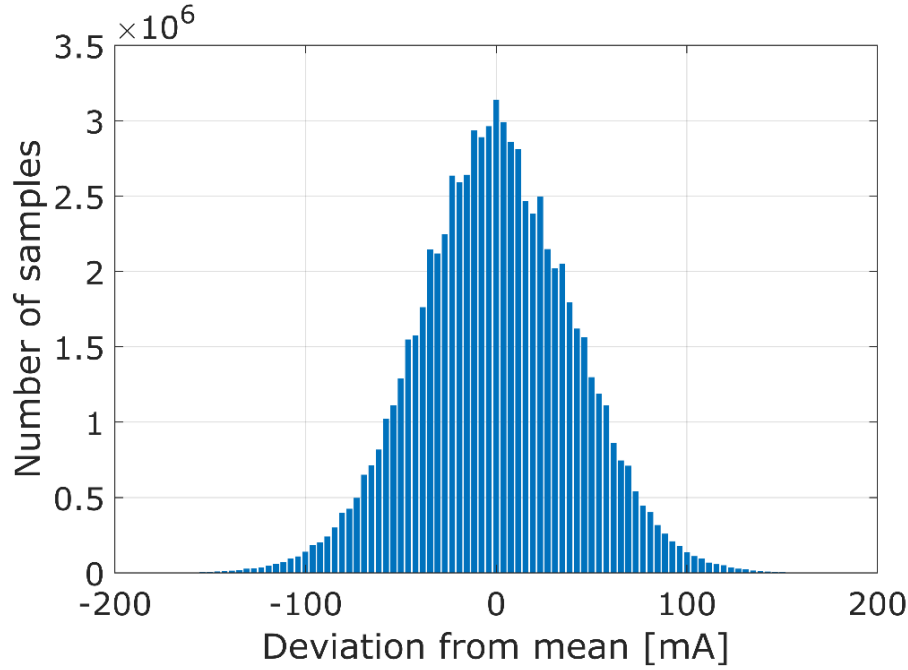


**Fig. 3.12** - Distribution of the sample data of the high-frequency current, normalized with respect to their mean value.

### 3.3. Results and Discussion

This section presents the results of the aging campaign conducted on the three MUTs according to the measuring procedures and to the index calculations illustrated in the previous sections. Fig. 3.13, Fig. 3.14, and Fig. 3.15 show the impedance, current, and spectrum deviations as a function of aging time. For each figure, the base, differential, and integral versions of the indices are reported.

It is worth highlighting the two different perspectives underlying the definition of the three versions of each index. After each aging cycle, the base version of the indices defined according to (3.1), (3.2), and (3.3) evaluates the actual insulation aging state as the absolute distance from the healthy state, regardless of the path followed to reach that state. In fact, it has been observed that the measured macroscopic quantities could undergo negative variations as well. Consequently, the base deviations are characterized by an up-and-down behaviour, as it can be noticed in the uppermost plot in the figures. A negative variation of the index, and hence a reduction in the distance from the healthy state, should not be directly interpreted as an insulation recovery phenomenon. The electrical aging process on a complex system, such as the stator winding, produces alterations of the insulation condition that are characterized by randomness. In fact, casual modifications can happen in different parts and with different intensity within the system. The cumulative effect of such random variations determines the overall capacitive behaviour that can be observed through measuring macroscopic quantities. It is for this reason that the differential and integral deviations are introduced for each index. The differential deviation, in fact, provides information about the distance between two consecutive aging steps, thus putting the focus on the intensity of single variations. Being carried out as the

sum of the differential deviations at each aging step, the integral deviation can reconstruct the overall path of aging that the insulation system experiences, still giving information with respect to the starting point (i.e. the healthy state).

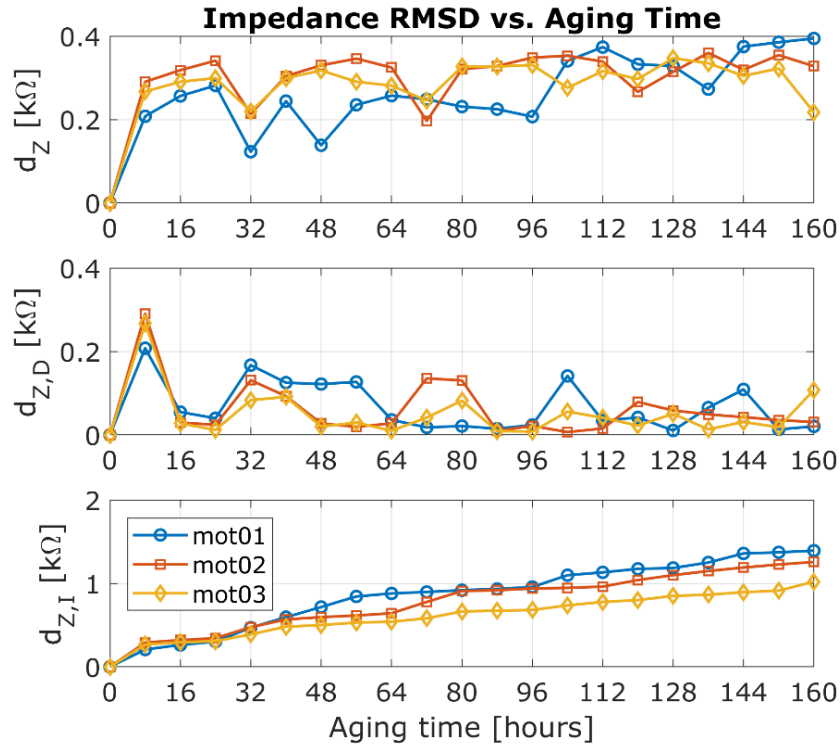


**Fig. 3.13** - Evolution of impedance deviation indices with aging time for the three motors under test.

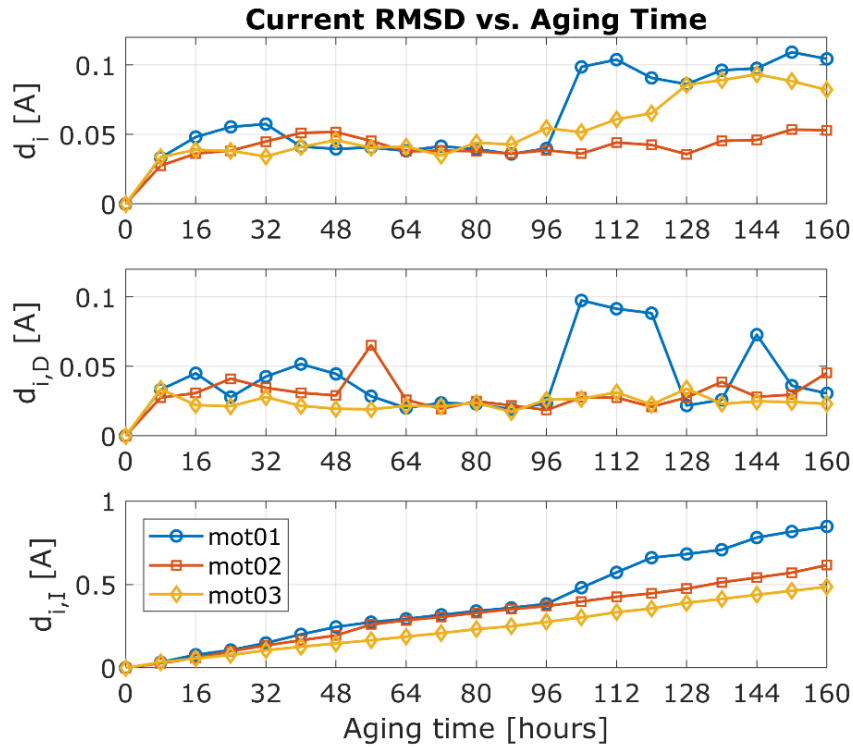


**Fig. 3.14** - Evolution of current deviation indices with aging time for the three motors under test.

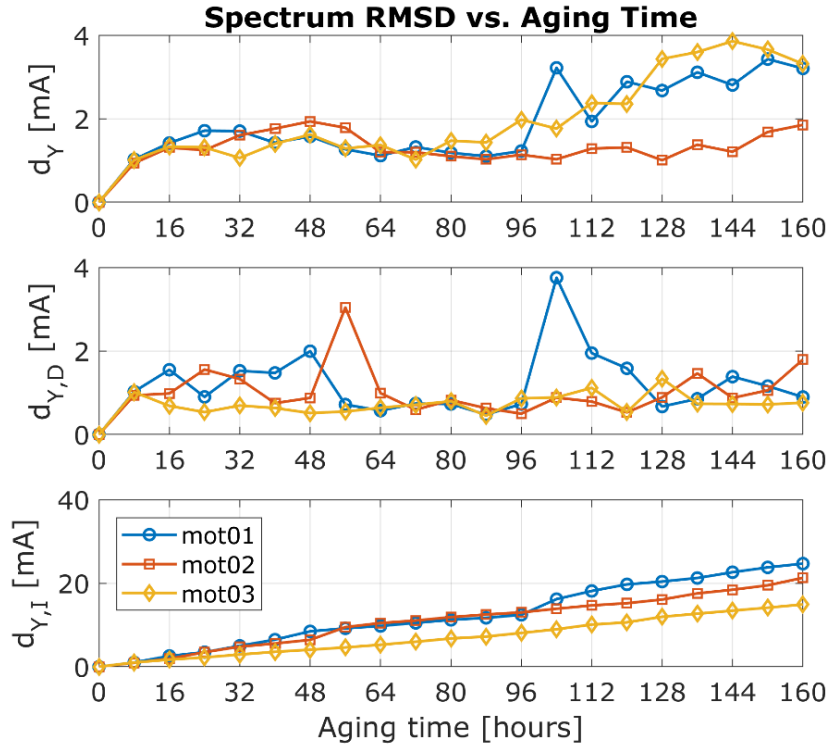


**Fig. 3.15** - Evolution of spectrum deviation indices with aging time for the three motors under test.

In Fig. 3.13, the base impedance deviation presents an initial sharp rise before settling around an almost constant value. For the MUT referred to as mot01 (blue lines in the figures)  $d_z$  initially settles around a value of about 0.2 k $\Omega$ , then, after 96 hours of aging, it ramps up to a value around 0.35 k $\Omega$ , similarly to mot02 (red line) and mot03 (yellow line). This step increase in the index could be due to an abrupt modification of the insulation state. From this result, one could wrongly infer a less intense aging progression for mot01 during the first 96 hours. However, if the differential deviation is considered, it can be noticed how mot01 undergoes more severe variations than the other two MUTs during the first 64 hours, leading to the highest integral deviation.

As it can be noticed by comparing Fig. 3.14 and Fig. 3.15, the trends of the current deviations and of the spectrum deviations are quite similar. The base deviations  $d_i$  and  $d_Y$  initially rise, with different rates for the three MUTs, to about the same value. After 96 hours, while the value for mot02 is almost constant, those for mot01 and mot03 sharply rise almost doubling. In particular, mot01 presents an abrupt variation similar, but more evident, to the one observed in the case of the impedance deviation. By looking at the differential deviations it is evident that mot02 and mot03 have a similar trend, but for the spike at hour 56. This reflects in the integral deviation value that is higher for mot02 despite the slope is the same. Therefore, mot02 presents a more advanced aging state than mot03, despite what observed in the base deviations. By comparing the base deviations of the three methods, it can be noticed that remarkable oscillations characterize the impedance deviation, making it difficult to recognize a clear trend for each motor. The trends of the current and spectrum deviations, instead, is more stable, and the aging

phenomena can be easily detected. On the other hand, the integral deviations of the three indices feature very close results, since a distinct trend for each motor can be assessed.

Focusing on practical implementation aspects, advantages and drawbacks of the proposed approaches can be discussed. The impedance measure is essentially an off-line method since the motor must be disconnected from the system. Moreover, it requires expensive laboratory instrumentation (high-precision impedance analyser) and can be time-consuming since three different winding connections have to be made, which require specific cabling of the MUT. The use of the high-frequency currents to detect aging progress can, instead, be performed during the motor start-up or included in self-commissioning procedures. In addition, it does not require expensive instrumentation, since the current measure could be made through commercial current transducers instead of the Rogowski coils, as demonstrated in [67]. As discussed before, the spectrum-based indices show similar performance with respect to those directly based on currents, which require less computational resources due to the absence of the FFT algorithm. Among the different proposed solutions, the current-based indices are more easily applicable in a practical drive and give the best information about the aging progression. The aging assessment through impedance measure, however, could be profitably used for modelling purposes, as it will be discussed in Chapter 4 of this thesis work. Regarding the index calculation, while the integral deviation performs better than the absolute deviation in describing the aging path that the motor undergoes, the differential deviation can give a useful indication about the intensity of the variations between two consecutive aging steps.

### **3.4. Publications**

The research work and the results presented in this chapter have been published by the author in [70] and [71].

## Chapter 4 Modelling in the High-Frequency Domain

The insight that has been acquired from the accelerated aging study presented in Chapter 3 can be profitably used to develop tools for the investigation and description of the high-frequency phenomena that affect the insulation of electric machines. To this purpose, it is necessary to recur to accurate high-frequency simulation models that can consider the interaction between the distributed motor capacitances (i.e., winding to ground and/or turn-to-turn) and the HF supply from the converters. Such accurate models may be useful for both system design optimization and implementation of advanced prognostic features to improve drive availability and reliability. Therefore, the objective of the research discussed in this chapter is twofold. On the one hand, after briefly discussing the available HF motor models in the literature, an accurate automatic modelling procedure is proposed that uses a genetic optimization algorithm (GA) to fit a set of measured experimental data. The experimental data used to this purpose are the characteristic impedances that have been obtained during the electrical aging procedure described in the previous chapter, which are available for each aging cycle. The use of an automated tuning procedure of the HF model would let the designer to save time by avoiding time-consuming trial-and-error tuning of the parameters. On the other hand, the second objective in developing this HF model is to achieve a very high fitting accuracy in order to distinguish the small impedance variations observed during the aging procedure. In this way, a time-varying model of the winding can be achieved, which parameters can be made dependant on a certain aging progression law. This approach could, for example, be useful to add a model-based diagnosis feature to the drive. The novel contribution of the presented approach is the use of a rational harmonic function for the fitting of the measured impedance data, instead of calculating the parameters of a pre-determined circuit model according to the values of certain points of the characteristic impedances, as commonly done in the literature. In this way, superior accuracy can be achieved in the fitting, with minimum convergence time and computational burden of the algorithm. The optimized rational function can then be turned into its circuit representation or used as a transfer function within the high-frequency model of the drive.

### 4.1. Review of the HF Models Proposed in the Literature

A variety of HF models of AC motors have been proposed over the last years in the literature. According to the approach used, electrical machine HF models can be roughly classified in three families [72]. Lumped-parameter circuit models [73]-[76] are equivalent circuit networks made of passive components, generally disposed as parallel RLC resonators and capacitive branches. These models make use of equivalent parameters to approximate the response of the machine in a wide frequency range. The values of the network components (i.e., resistors, inductors, and capacitors) are usually manually calculated from the values of specific points in the machine frequency characteristics. In [76] this time-consuming manual tuning is substituted by an

automatic fitting procedure using a genetic optimization algorithm. Distributed-parameters circuit models [77], instead, model the machine winding in its length with per-unit circuit elements, generally a  $\Pi$ -type or T-type equivalent. The aim is to obtain a better approximation of the winding parasitic parameters considering its structure and its interaction with the other machine parts. Although very good accuracy is achievable with this approach, the main drawback is the overall model complexity resulting in simulation time too large for their practical use. Transmission line models are the third family of HF motor models. They are based on the transmission line theory and analytically model the machine voltages and currents taking into account the effects of wave propagation through the winding. This approach, however, requires the use of time-consuming 3D finite element simulations with highly accurate geometries to correctly determine the inductance and capacitance matrices [78], [79].

For their simpler structure and ease of tuning without using finite-element simulations, lumped-parameters models are the most commonly employed. In particular, [80] proposes a first simple model, of a single phase, which presents, between the phase and the neutral, a series connection of the stator/rotor resistance and the leakage inductance to describe the low-frequency behaviour, a resistance to account for eddy currents inside the magnetic core and the frame, a capacitance representing the turn-to-turn distributed capacitive coupling. Besides these elements, there is a capacitor between the phase and the ground and an equal capacitor between the neutral and the ground to model such distributed capacitive coupling of the winding. Unlike [80], [81] proposes a per-phase model which is made up of the leakage inductance of the machine to describe the low-frequency behaviour and an R-L-C network to capture a second resonance in the frequency response, which is related to the winding turn-to-turn capacitance. While the branches that include the capacitors, representing the winding to ground coupling, present additional series resistors. A three-phase model is firstly introduced in [82], which also includes mutual inductances to describe the magnetic coupling among the phases. In this paper, the series connection of two resonators is adopted for each phase to represent the part of the winding embedded in the stator slots and the end windings. Each resonator slightly differs from the model of [80]. An improved motor model is also proposed in [83], which is capable of accurately capturing the high-frequency Differential Mode (DM) and Common Mode (CM) impedance characteristics. It differs from the model proposed in [81] only because the capacitors phase-to-ground and neutral-to-ground are not equal. In order to improve the prediction of the CM current peak value, the inductance of the connectors and internal line conductors are considered in [84]. For the same reason, in [76] two coil-like impedances (one for each end of the winding) are added.

## 4.2. Proposed Automatic Modelling Procedure

The first approach adopted during the development of the high-frequency model of the machines tested in Chapter 3 has been to select one of the available models and to build an automatic fitting procedure to find the model parameters. The model that has been used for this



purpose is the one proposed by Degano *et al.* in [76], whose per-phase circuit is depicted in Fig. 4.1. this model consists in 13 parameters to be fitted, the ones indicated in the picture, plus the mutual inductance  $M_2$  between the central coils of the phases.

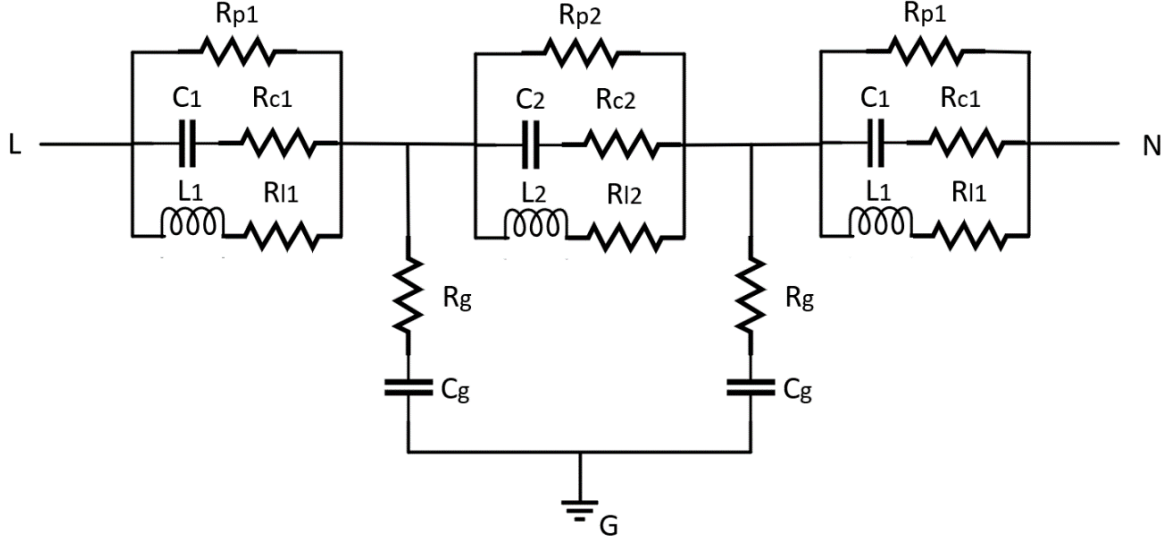


**Fig. 4.1** – Per-phase equivalent circuit of the high-frequency motor model used to implement the automatic modelling procedure, proposed in [76].

In order to avoid time-consuming trial-and-error tuning of the parameters and to automate the procedure, a genetic optimization algorithm (GA) has been implemented to optimize the selection of the circuit parameter values that allow the best matching with the measured machine characteristic impedances. The results of the fitting compared to the experimental data acquired for the healthy state of one of MUTs are shown in Fig. 4.2, Fig. 4.3, and Fig. 4.4. The magnitude of both the common mode ( $Z_{cm}$ ) and differential ( $Z_{dm}$ ) impedances present a good agreement with the measured data only in the first portion of the spectrum, i.e. the main resonance peak is captured by the model. The same cannot be said for the parasitic impedance ( $Z_{pm}$ ), where the resonance frequency is slightly lower than the actual value. However, for all three impedances, the high-frequency portion of the spectrum is not fitted correctly, a problem that can be attributed to the low order of the selected model. Furthermore, by looking at the phase angle, it also appears evident that a low-frequency error is made, especially in the differential impedance. In a nutshell, it can be concluded that this first model can achieve good agreement with experimental data for frequency values up to 1 MHz, but it is not able to meet satisfactory accuracy requirements for modelling small variations that can occur with aging.

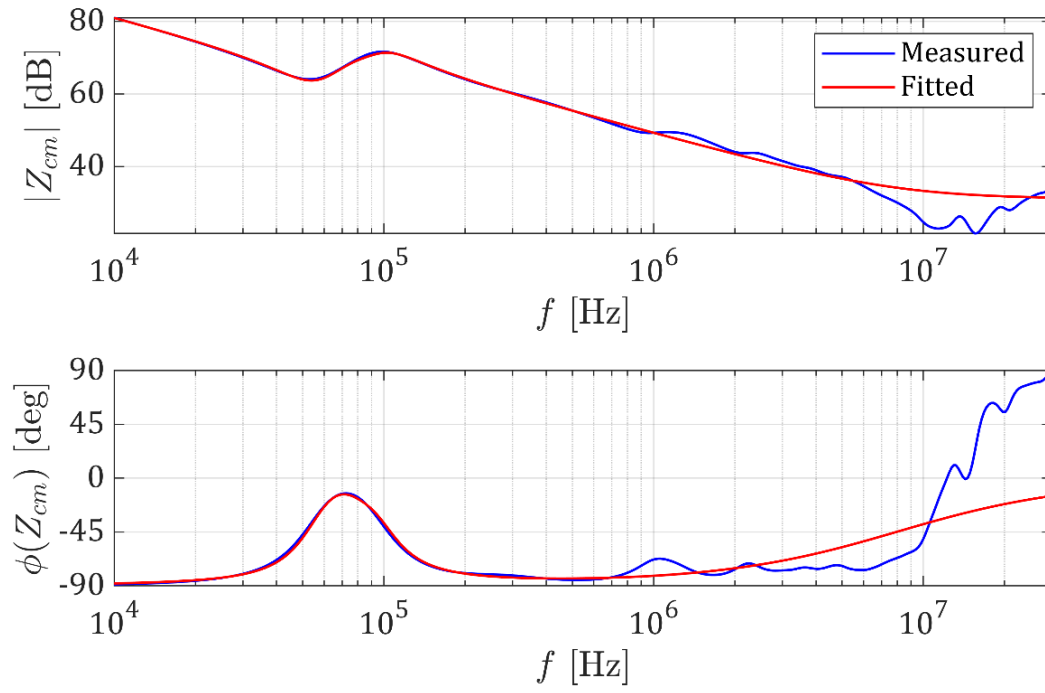


**Fig. 4.2** – Fitting results of the optimization performed with the model proposed in [76]: common mode impedance magnitude (in dB) and phase (in degrees).

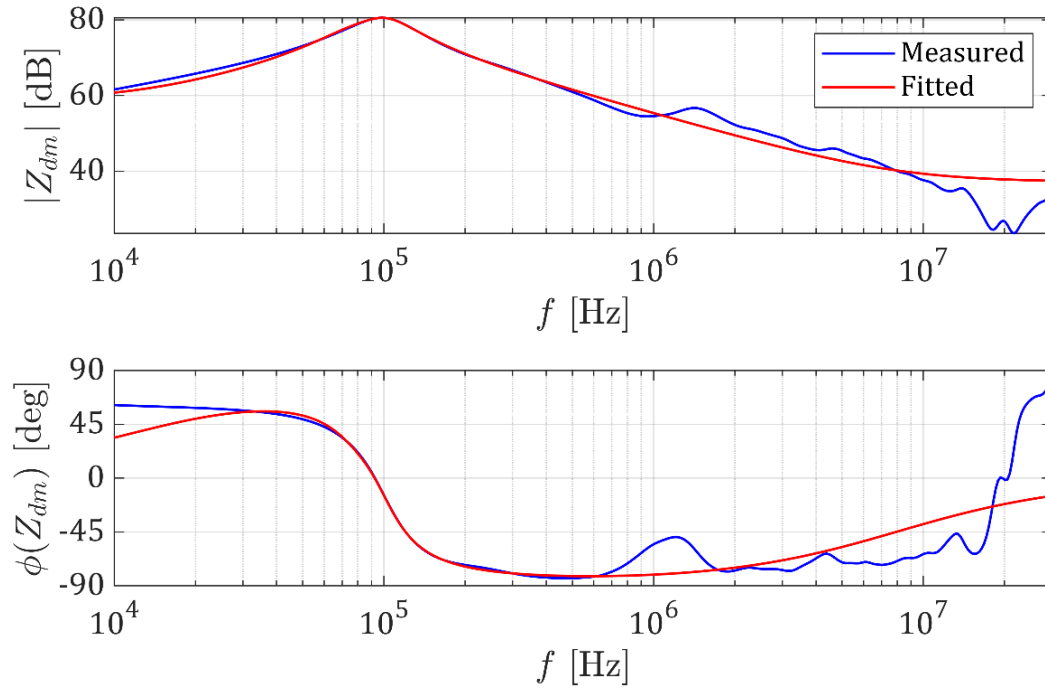


**Fig. 4.3** – Fitting results of the optimization performed with the model proposed in [76]: differential mode impedance magnitude (in dB) and phase (in degrees).

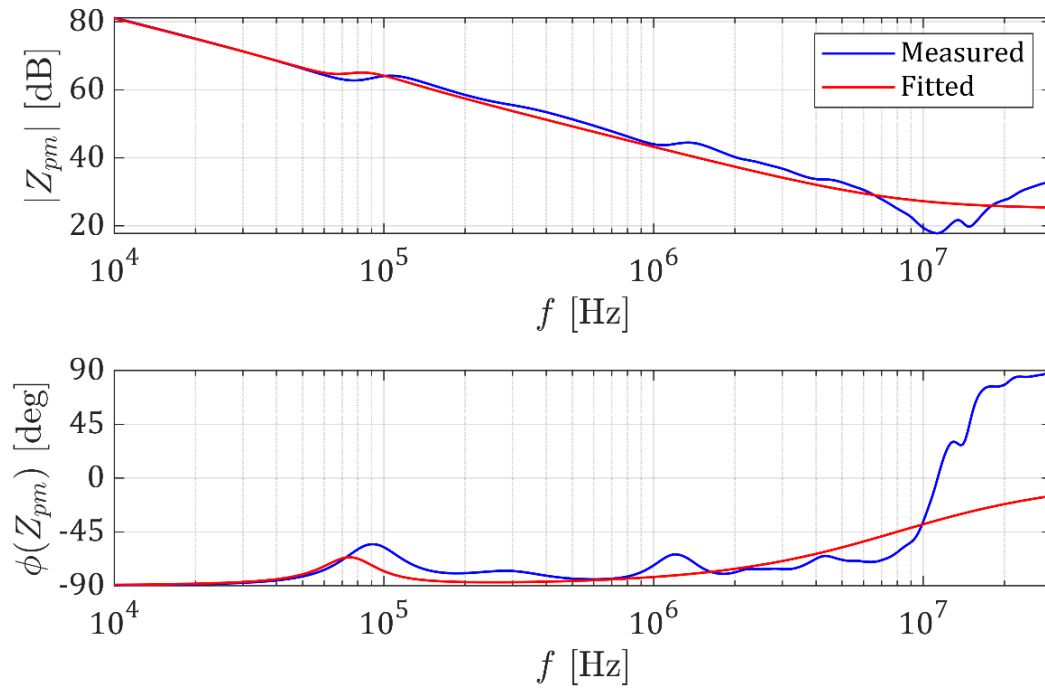


**Fig. 4.4** – Fitting results of the optimization performed with the model proposed in [76]: parasitic mode impedance magnitude (in dB) and phase (in degrees).

The main issue with the first model employed is the low accuracy, especially in the high-frequency domain where the largest aging variations have been seen to occur, as shown in Fig. 4.5 and 4.6. Regarding the aging effects, in fact, it appears that the impedance variations due to electrical stress are mainly concentrated in the very high-frequency portion of the spectrum and are more evident in the common mode impedance. The effects in the range between 10 kHz and 1 MHz progress at a much slower rate than in the case of thermal aging, as shown in [85]. This could be because, unlike partial discharges that are localized phenomena, the thermal stress affects greater portions of the winding, in a more uniform way. A more intense voltage level could probably speed up the aging process due to a more diffused partial discharge activity. However, the focus of the aging tests is the investigation of the aging progression in a low voltage drive operating in realistic conditions. The very small variations in the machine impedances require a very accurate fitting to proper model the aging progression. Further issues are related to the convergence of the algorithm. It has, in fact, been experienced that by fitting the model on three impedance curves, which are related one to each other, convergence to a local minimum may occur. This can be due to the low number of circuit elements, which limit the degree of freedom of the algorithm in the search space. The addition in the model of a third resonator is not enough, probably because the parasitic and the common mode impedances share some dynamic modes that cannot be fitted individually. For this reason, the proposed solution only uses two impedances, the common mode and the differential. Moreover, the presence of the third resonator also affects the computational burden of the optimization algorithm. Due to the fixed model structure, in fact, a closed analytical form does not exist for

the simulated impedances. For this reason, Simulink must be used within the routine to extract a linearized representation of the circuit for each set of parameters, resulting in longer execution time.

The proposed modelling procedure has the objective to obtain the highest fitting accuracy as possible in order to track the small aging steps observed during the electrical aging campaign. Computational burden is also an important feature to reduce the modelling time. As discussed above, the main drawback of the models that are commonly used in the literature is the limited degree of freedom in adjusting the model parameters. A fixed model structure, in fact, can only achieve limited fitting accuracy, especially at higher frequency. To overcome this limitation, the proposed solution aims at finding the best rational harmonic function in the frequency domain so that the deviation between the measured and the simulated values of the impedance is minimized. Two different functions need be found, one to approximate the common mode impedance, denoted as  $\tilde{Z}_{cm}$ , and one for the differential impedance, indicated as  $\tilde{Z}_{dm}$ . The novel characteristic of this approach is that, by using a mathematical function to approximate the frequency response, the poles and zeroes are not predetermined in number and location as for a fixed circuit topology. A network representation of the model can then be obtained from the identified rational function.

A genetic optimization algorithm has been implemented to perform the automatic identification of the common mode and differential harmonic functions. A GA is an optimization routine based on the concept of natural selection, driving mechanism of biological evolution. In a GA, an initial population comprising a certain number of individuals is generated and let to evolve through the course of various generations. Each individual in the population is represented by a vector of optimization variables (*genes*), which can vary within a predefined search space. At each generation, the entire population is evaluated according to the criteria of a fitness function, and the individuals are sorted based on their result. At this point, the best performing individuals are selected for recombination, so that a new generation is produced (*children*) from the previous one (*parents*) through the crossover and the mutation operators. The process repeats until a stopping criterion is satisfied. This type of optimization approach can be very profitably used for problems with a large number of parameters, which in general are characterized by a significant number of local minima that prevent them to be solved by conventional algorithms. For this reason, it has been chosen in this work. In the following, the main aspects of the proposed algorithm are described, highlighting the features that allow a good accuracy to be reached.

#### 4.2.1. *Fitness function definition*

The fitness function is the criterion that the GA uses to decide on the goodness of a certain individual among others. The fitness function that is used in the proposed algorithm is the sum of the two absolute errors calculated in terms of magnitude and phase for the two impedances to be fitted.

$$FF = \sum_{k=1}^{N_{pt}} E_{cm}(f_k) + E_{dm}(f_k) \quad (4.1)$$

In (4.1),  $f_k$  is the  $k^{th}$  measured frequency point,  $N_{pt}$  is the total number of measured data for each impedance,  $E_{cm}$  is the value of the absolute error calculated for the common-mode impedance, and  $E_{dm}$  the one calculated for the differential impedance:

$$E_j(f_k) = \text{abs}(|Z_j(f_k)| - |\tilde{Z}_j(f_k)|) + \text{abs}(\angle Z_j(f_k) - \angle \tilde{Z}_j(f_k)) \quad (4.2)$$

where  $j$  represents either  $cm$  or  $dm$ , and the “ $\sim$ ” symbol denotes the approximation functions. To be sure to obtain a well scaled fitness function, in (4.2), the magnitude of the impedance is expressed in dB and the phase in degrees. In this way, both errors are equally weighted during the optimization leading to a faster and more accurate convergence of the algorithm.

#### 4.2.2. Form of the harmonic function and boundaries of the search space

The common mode and differential impedances as a function of frequency are shown in Fig. 4.5 and Fig. 4.6, respectively for the healthy insulation state and for a degraded condition after a few aging cycles. Only one of the tested motors is shown in the figure, but similar results are obtained for the other two machines.

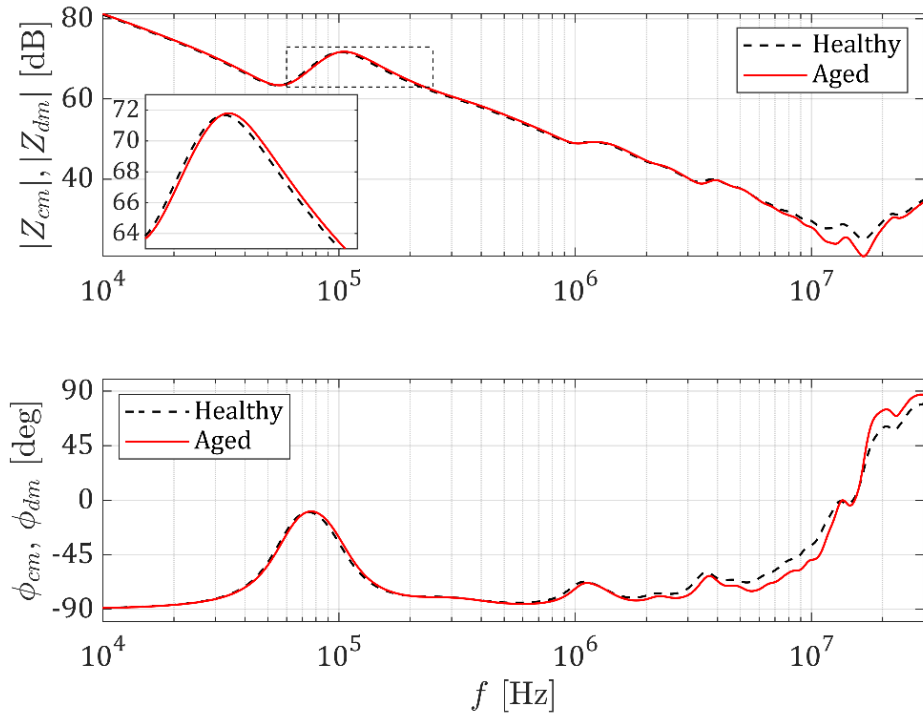


**Fig. 4.5** – Common mode impedance as a function of frequency, expressed as magnitude and phase. The black dashed line refers to the healthy insulation state, the red line to the measure taken after about 50 hours.

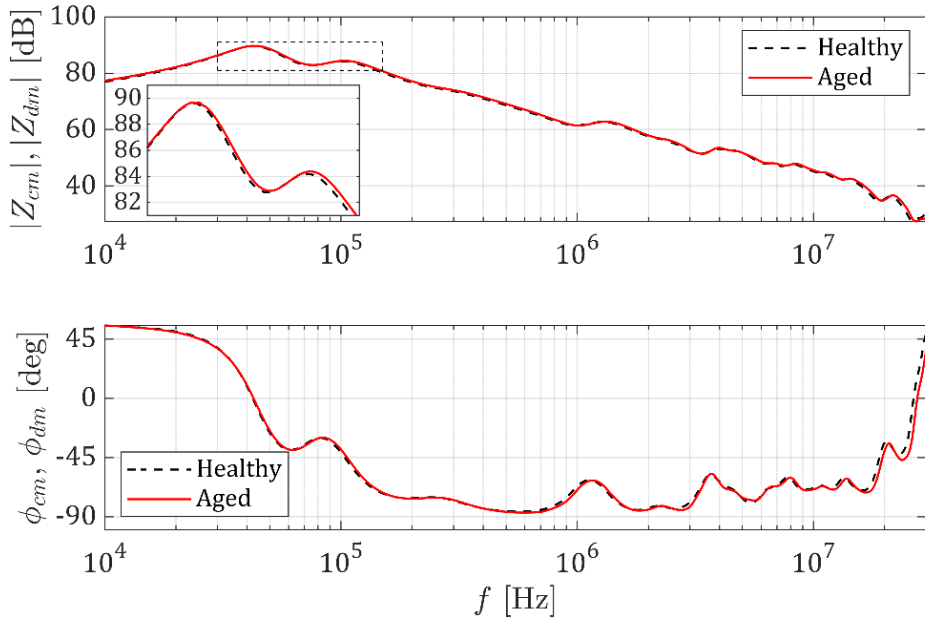


**Fig. 4.6** – Differential impedance as a function of frequency, expressed as magnitude and phase. The black dashed line refers to the healthy insulation state, the red line to the measure taken after about 50 hours.

The common mode impedance is characterized by a very high magnitude at low frequency, which is due to the blocking effect of the phase-to-ground capacitances generated by the insulation between the phase coils and the stator iron. The differential impedance, instead, has lower magnitude at low frequency and is characterized by two adjacent resonance peaks around 100 kHz. A higher number of resonance peaks and notches with lower amplitude are observed in the very-high-frequency range for both the impedances. From a modelling point of view, each peak and notch suggest the presence, respectively, of a complex conjugate pole or zero pair. Therefore, the number of pole-zero pairs increases at higher frequencies. This aspect can be considered in the automatic fitting procedure to reduce the computational burden and the time cost of the genetic algorithm.

The harmonic functions to be found that approximate the machine impedances are implemented in the algorithm in the poles-zeroes form as in (4.3).

$$\tilde{Z} = K \frac{\prod_{p=1}^{N_{zr}} (s - \omega_p) \prod_{q=1}^{N_{zcc}} \left( \frac{s^2}{\omega_{n,q}} + \frac{2\delta_v}{\omega_{n,q}} s + 1 \right)}{s^\mu \prod_{t=1}^{N_{pr}} (s - \omega_t) \prod_{v=1}^{N_{pcc}} \left( \frac{s^2}{\omega_{n,v}} + \frac{2\delta_v}{\omega_{n,v}} s + 1 \right)} \quad (4.3)$$

In the above equation,  $K$  is the function gain,  $N_{pr}$ ,  $N_{zr}$ ,  $N_{pcc}$ , and  $N_{zcc}$  are, respectively, the number of real poles, real zeroes, and complex conjugate pairs of poles and zeroes.  $\omega_p$  and  $\omega_t$  are the frequency locations, in rad/s, of the real zeroes and poles, while each complex conjugate pair of poles or zeroes is described by its natural pulsation  $\omega_n$  and the damping factor  $\delta$ .  $\mu$  is the algebraic multiplicity of the poles in the origin. Its value is set to 1 for the common-mode impedance and to 0 for the differential impedance.

By employing the description in (4.3) for the harmonic functions to be optimized, defining the individuals' optimization variables becomes straightforward. The vector  $x$  of the optimization variables is therefore defined as follows:

$$x = [\Omega_{pR} \ \Omega_{zR} \ \Omega_{pCC} \ \Delta_{pCC} \ \Omega_{zCC} \ \Delta_{zCC} \ K] \quad (4.4)$$

Here:

- $\Omega_{pR} \in \mathbb{R}^{1 \times N_{pr}}$  is the sub-vector of the real poles;
- $\Omega_{zR} \in \mathbb{R}^{1 \times N_{zr}}$  is the sub-vector of the real zeroes;
- $\Omega_{pCC}, \Delta_{pCC} \in \mathbb{R}^{1 \times N_{pcc}}$  are the vectors of the natural pulsations and damping factors of the complex poles;
- $\Omega_{zCC}, \Delta_{zCC} \in \mathbb{R}^{1 \times N_{zcc}}$  are the vectors of the natural pulsations and damping factors of the complex zeroes;
- $K \in \mathbb{R}$  is the gain.

Defining the individual as described above makes easier to control both the generation of the initial population, which has been found to be a key element for the fast and accurate convergence of the algorithm, and the selection of the constraints for the search space. The latter advantage is due to the knowledge of the shape of the frequency curves to be fitted, so that the poles and zeroes can be limited to the frequency range of interest (i.e., between 10 kHz and 30 MHz). furthermore, the variation of the damping factors is naturally limited between 0 and 1. The only element that makes it difficult to define limits for is the function gain  $K$ . The reason is that its value can have a very large variation range, therefore a few tries are needed to find the proper boundaries for this parameter, before starting the core optimization procedure. This step does not require too many generations to be processed, since after a few iterations the algorithm tends to converge towards a value that is close to the final one. A starting procedure could also be implemented to automatize this step.

#### 4.2.3. *Generation of the initial population*

A crucial factor in determining the convergence of the genetic algorithm is the generation of the initial set of individuals to start the evolutionary process. It has, in fact, been observed that uniformly generating the initial population allocating the poles and zeroes in the frequency range of interest leads to the non-convergence of the algorithm in a reasonable time. To overcome this issue, a specialized generation function has been built that divides the frequency range to be fitted in three intervals, according to the concentration of resonance peaks in the measured data. The first interval is defined between 10 and 100 kHz, with a lower number of pole-zero pairs; the second one is defined from 100 kHz to 1 MHz, presenting an higher number of peaks; The last interval goes from 1 MHz to 30 MHz and presents the higher concentration of resonances and notches. For each of the three intervals a weighting factor is selected so that their sum is equal to unity (e.g.,  $w_1 + w_2 + w_3 = 1$ ). The number of poles to be allocated in each

frequency segment is then equal to the total number of poles or zeroes multiplied by the associated weight. The poles and zeroes are distributed uniformly in each interval also considering an overlap factor. The latter enlarge each frequency interval by a certain percentage to achieve an initial population with a higher variety. A good value for the overlap factor is found to be between 15% and 20%. With the above-described generation function, both speed and accuracy of the genetic algorithm are greatly improved.

#### 4.2.4. *Selection, crossover and mutation operators*

The crossover operator is used after the individuals have been evaluated according to the fitness function and a percentage of them has been selected for recombination. The selection function used in this work is the *stochastic uniform sampling* (SUS). In SUS, the selection of the parents is made by sampling at an equal rate along a line made by a number of segments that is equal to the number of individuals evaluated. Each segment of the line is proportional to the fitness value of the associated individual. By sampling along the line at a constant rate, the better individuals are more favourably selected with respect to the weaker ones.

The *intermediate crossover* function is used in the proposed algorithm. This crossover operator creates a child  $c$  as the weighted average of its parents  $p_1$  and  $p_2$ .

$$c = p_1 + R * (p_2 - p_1) \quad (4.5)$$

$R$  is a random real number, whose variation range controls the position of the child with respect to its parents. If  $R \in [0; 1]$ , then the child lays between the values of the genes of its parents. In the proposed GA implementation,  $R$  is set to vary up to 1.5, meaning that the value calculated for the child can be outside the segment defined by its parents. This choice, despite being theoretically in contrast with the convergence of the optimization algorithm, has been found to be beneficial for accuracy, since, together with the mutation operator, gives more flexibility in the search space. Two other important parameters in the crossover function are the so-called *elite fraction* (set to 0.05) and *crossover fraction* (set to 0.1). The first specifies the percentage of individuals that will survive to the next generation, while the latter specifies the percentage of children that will be created by crossover. Both these parameters let the algorithm to maintain both the best and the worst individuals of a generation to the new one. This can be useful to avoid premature convergence to a local minimum.

The mutation crossover applies to the children obtained by crossover a small random change in their gene values. In this way, the algorithm can investigate a broader space and achieve more genetic diversity. The selected operator for the proposed GA is the *uniform mutation*. First, part of the genes of each individual are selected for mutation with a certain probability rate (i.e., 15% for our case), then the value of the selected genes is replaced by a random value within the constraints that are set for that variable.



#### 4.2.5. *Local optimization and aging variations*

As it can be deduced by the previous description, a series of parameter are included in the proposed algorithm that increase the genetic diversity of the population. Furthermore, the size of the population itself is chosen to be fifteen times the length of the optimization variables vector, which is a large number considering the high order of the rational function to properly identify the high-frequency points. This is due to the large number of local minima that are present in the search space, because of the complexity of the problem and the large number of pole-zero pairs. With the values indicated above for the crossover rate  $R$ , for the elite and crossover fractions, and for the mutation rate, a good genetic diversity is reached, and the procedure can converge near the global minima. However, for the same reason, it is then hard for the algorithm to properly optimize toward the best fit within the found minimum. It is for this reason that, after the GA run is completed, the optimized set of variables is used as the initial solution of a constrained minimization problem to be solved with a gradient-base routine, which is best suited for local minima optimizations. The selected algorithm is the interior-point optimization. The function value is reduced up to one third of its starting value by using this approach, which leads to a very good final accuracy.

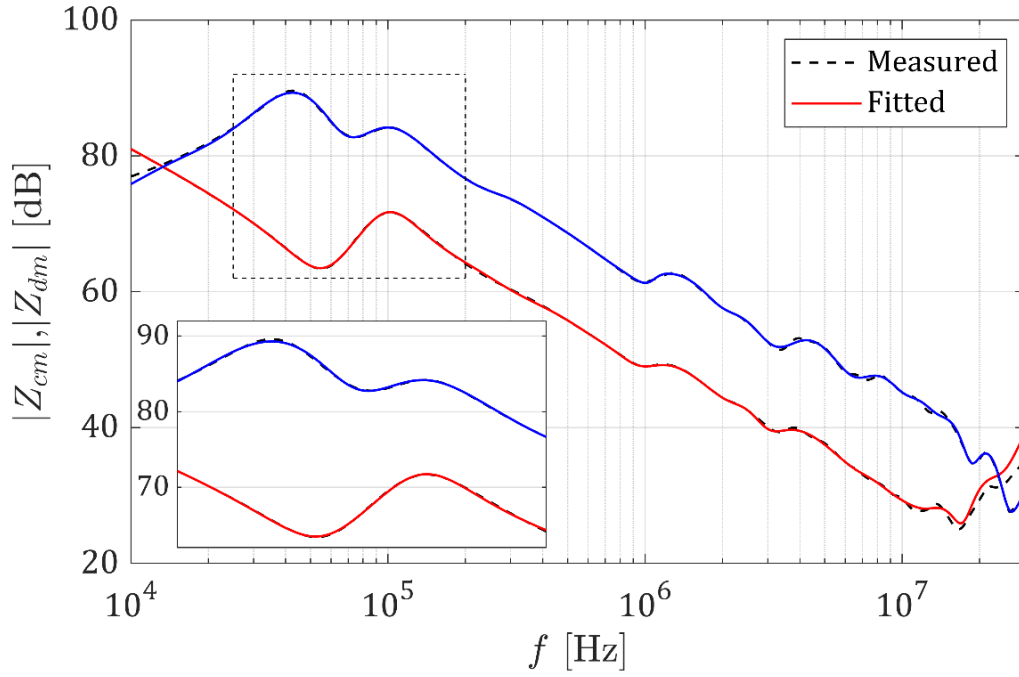
Speaking about execution time of the whole algorithm, the GA take between 15-20 minutes to complete on a quad-core PC with 16 GB RAM, while the local minimization requires about 1-2 minutes to converge. As a result, the total required time is lower than 25 minutes for the fitting of the two impedances of a motor, confirming the goodness of the proposed approach.

The local search algorithm that finishes the fitting routine is also used to evaluate the variation of the optimized model parameters according to the progression of aging. For each aging step, in fact, a local optimization run is launched, where the initial set of parameters is set to be the solution of the optimization at the previous aging step. In this way, coherence of the variation is guaranteed. From the analysis of the results, it is possible to establish a direct link between the poles and zeroes of the model and the impedance variations observed during an aging campaign. Then, according to the data, the coefficients of the harmonic functions can be expressed as a function of some “*aging factors*”, so that a simulation model for the insulation degradation may be derived. Such a model can be very profitably used either to implement prognostic features in high-speed drives or to describe the intensity variation in function of time of the oscillatory phenomena.

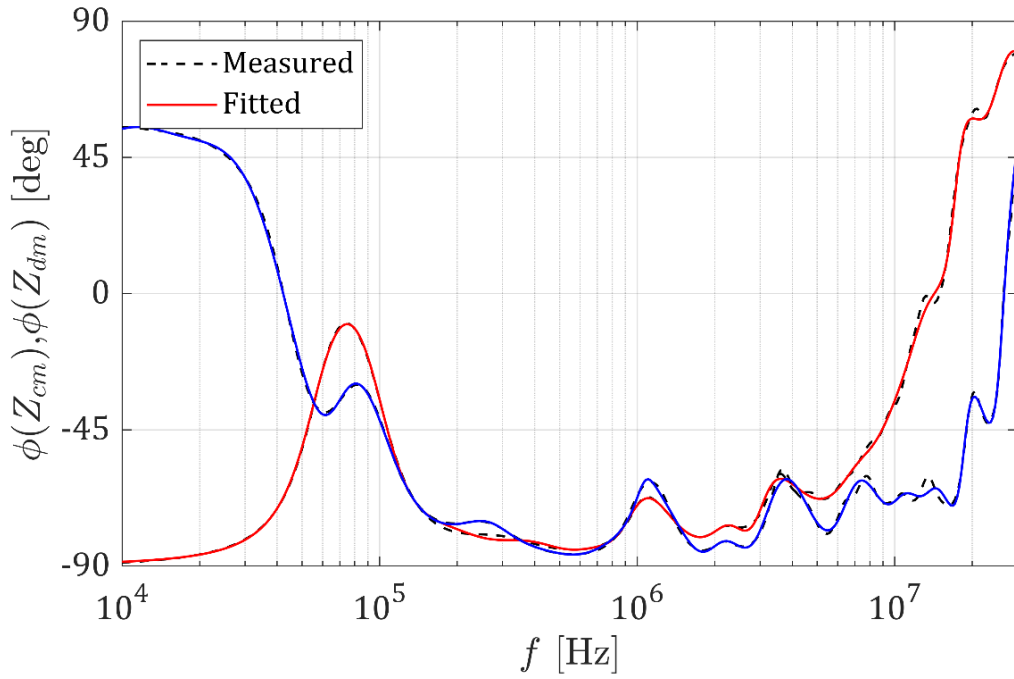
#### 4.2.6. *Results and Discussion*

Fig. 4.7 shows the result of the fitting procedure on the magnitude of the common-mode and differential impedances at the healthy insulation state. The phase is depicted in Fig. 4.8. There is a very good agreement between the measured and the fitted curves, despite minor divergences at the limits of the frequency interval in both impedances. To quantify the accuracy of the algorithm the mean absolute error is calculated for both impedances as the averaged sum of the deviations at each measured frequency. Its value is equal to 0.41 (dB in the case of the modules

and degrees for the phases). For the common-mode impedance, the order of the harmonic function is 20, while for the differential impedance is 22 (2 more poles in the lower frequency interval). To improve the algorithm accuracy at the boundaries of the frequency window a few more measurement point could be needed, however, the major features are captured in this configuration, since the low frequency behaviour is not an objective of the model.



**Fig. 4.7** – Comparison of fitting accuracy for the healthy state for the CM (red line) and the DM (blue line) impedance: magnitude.



**Fig. 4.8** – Comparison of fitting accuracy for the healthy state for the CM (red line) and the DM (blue line) impedance: phase.

To verify the goodness of the algorithm in catching the small variation due to the aging, a comparison between two aging states is depicted in Fig. 4.9 and Fig. 4.10 for the common-mode and the differential impedances, respectively. The values of the mean absolute errors are indicated in Table 4.I both for the experimental data (deviation between healthy and aged condition) and for the fitting. The accuracy obtained with the proposed procedure is good enough to catch aging variations of the entity observed in this work. By performing more tests on the motors, it could be then possible to build an accurate high-frequency model with time-varying parameters. This model could be profitably used either for design purposes or in model-based diagnosis algorithms. For the latter, a greater number of tests would be needed also to add statistical features to the model and to characterize different motor sizes and winding topologies.

**Table 4.I** – Mean absolute errors between measured and fitted values and healthy and aged data for  $Z_{cm}$  and  $Z_{dm}$ .

	Common-mode imp.	Differential imp.
<b>Healthy – Aged (exp.)</b>	1.98	0.68
<b>Meas. – Fit. (Healthy)</b>	0.41	0.41
<b>Meas. – Fit (Aged)</b>	0.49	0.46

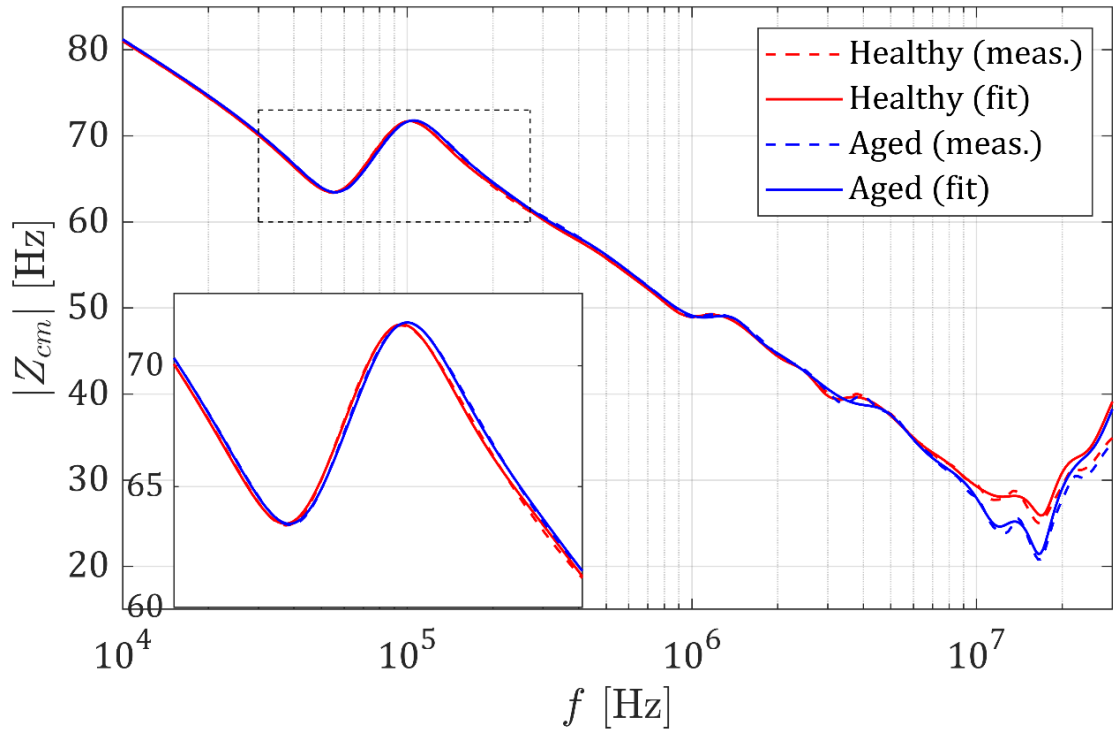


**Fig. 4.9** - Comparison of fitting accuracy between healthy and aged state for the common-mode impedance.

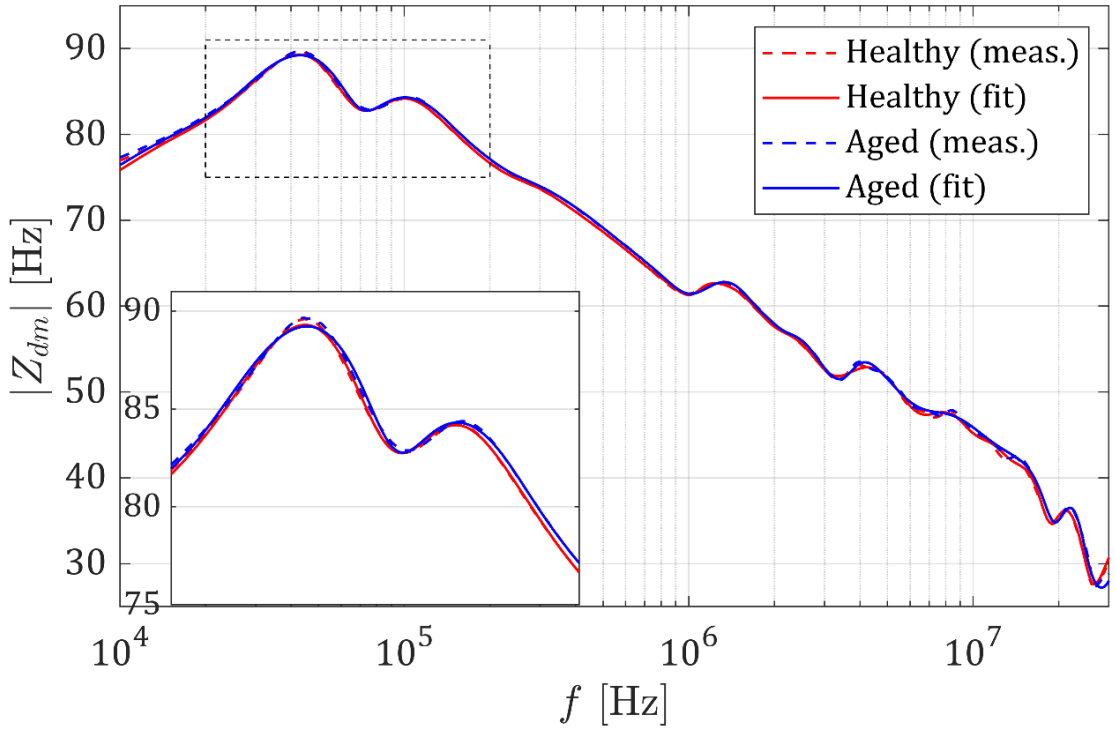


**Fig. 4.10** - Comparison of fitting accuracy between healthy and aged state for the differential impedance.

### 4.3. Simulation of the Overvoltage at Motor Terminals

To conclude this chapter about drive modelling in the high-frequency domain, a suitable representation of the converter together with the connection cable is required to correctly predict the reflection transient at the motor terminals. To this purpose, the equivalent circuit in Fig. 4.11 has been used, where the inverter is simply modelled through its output series impedance ( $R_{inv} + j\omega L_{inv}$ ) while for the cable the capacitive coupling with the ground is also included.

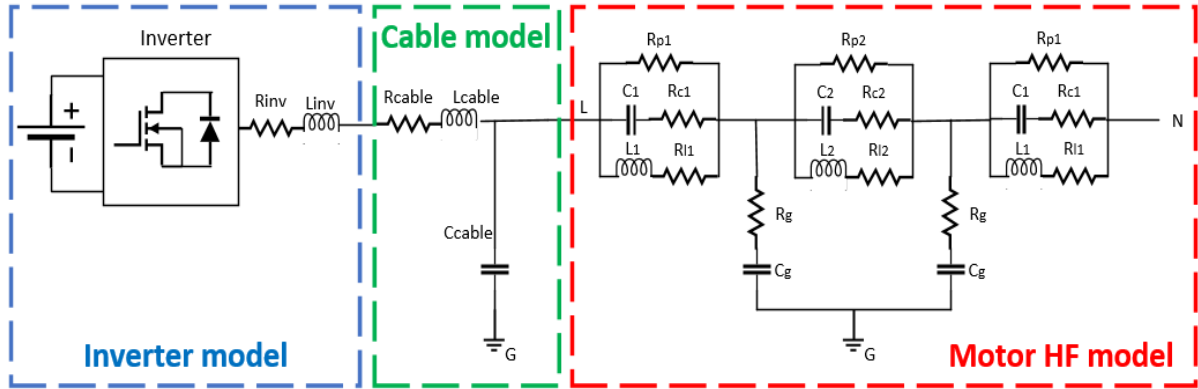


Fig. 4.11 – Equivalent high-frequency circuit of inverter-cable-motor system (per-phase).

The cable impedance can be found from its open-circuit and short-circuit impedances, measured with an impedance analyser over a wide frequency range. The cable model parameters mainly affect the frequency of the ringing transient produced by the reflection phenomenon over the cable length. The output impedance of the inverter, instead, has mainly an effect on the shape of the voltage waveform at the inverter terminals.

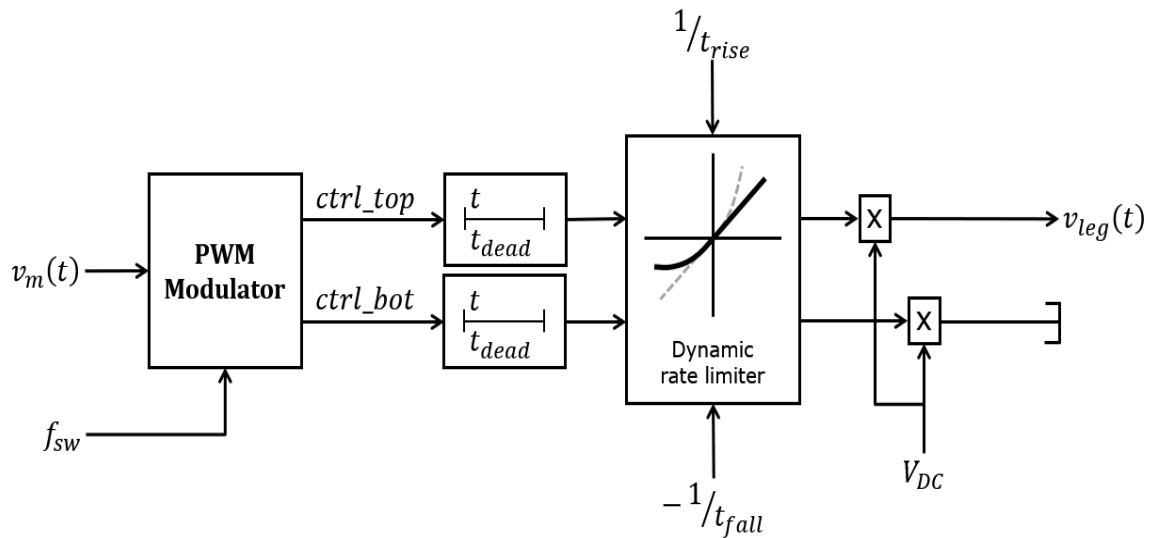
#### 4.3.1. Inverter analytical model

To properly simulate the cable voltage reflections that produce the overvoltage at the terminals of the machine, a switching model of the inverter is required to consider the effect of rise and fall times. However, to achieve this purpose with a physical model would require including a detailed model of the power devices to simulate the exact switching behaviour of their voltage and current waveforms, with consequent increase of computational burden. Furthermore, including a switching model would also require the simulation step to be very short to catch the HF dynamics, which in turn would drastically increase the simulation time of the model. If the aim of this kind of model is the simulation of aging mechanisms that would take hours or days to happen, it is then clear that this modelling approach is not adequate to the purpose.

To avoid the afore-mentioned problems, two measures have been taken. First, the inverter switching behaviour is modelled analytically by calculating the applied voltage waveform mathematically and then supplying it to the equivalent HF circuit by mean of a *controlled voltage*

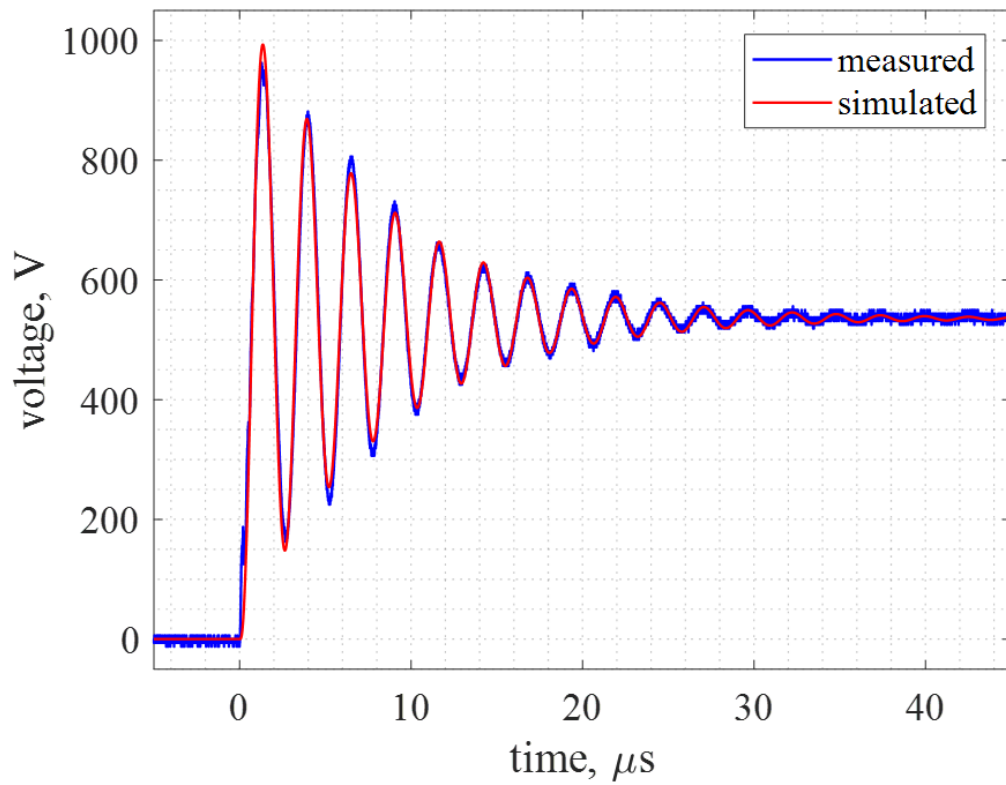
source circuit element. Second, a time-scale decoupling must be used for the simulation of the electrical aging mechanism, which will be described in more detail in Chapter 5. Here, a brief description of the analytical model of the converter is done, to the purpose of correctly simulating the overvoltage produced at the motor terminals. A functional scheme of the inverter analytical model proposed is depicted in Fig. 4.12.

The control signals to drive the devices are calculated by comparing three sinusoidal duty cycles with the triangular carrier signal, as in every sinusoidal PWM technique. For each leg, two PWM signal varying between 0 and 1 are therefore generated. Dead times are then introduced at this point to avoid leg short-circuit according to the switching times of the devices. The signal for the upper device, at this point, corresponds to the leg voltage  $v_{leg}$  scaled by a factor  $V_{DC}$ , i.e. the value of the DC-link voltage. To take the switching transient into account, the gate signals are fed to a dynamic rate limiter, which is configured to apply a slope that is proportional to the inverse of the rise and fall times. Finally, the phase and line voltage to supply the motor are calculated considering the DC-link voltage value.



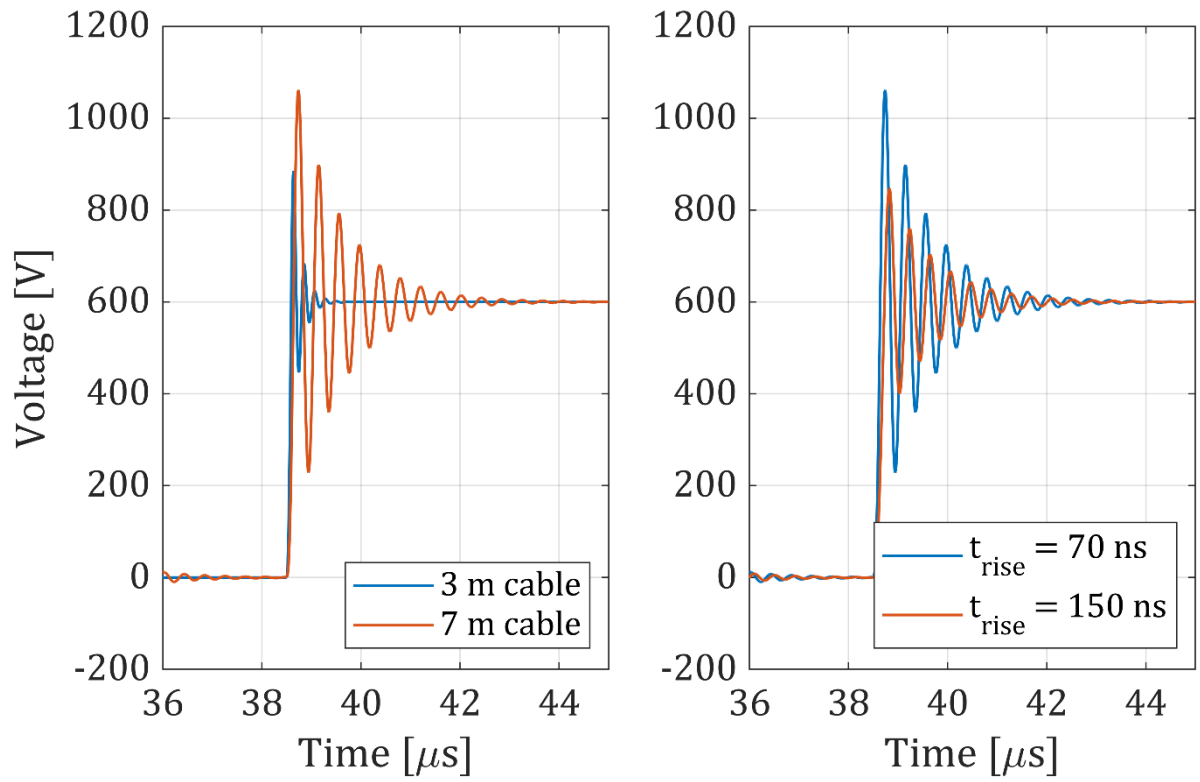
**Fig. 4.12** - Functional scheme of the analytical converter model.

Fig. 4.13 shows the agreement between the simulated and the measured voltage waveform at the motor terminals when a voltage pulse of 540 V and 70 ns rise time is applied by the inverter to the electric machine through a cable of 30 m. The development model proves to be adequate for the simulation of the high-frequency phenomena.



**Fig. 4.13** – Voltage at the motor terminals with a 30-meter-long cable and 70 ns voltage pulse rise time: agreement between measured and simulated data.

The developed model can be used to estimate the overvoltage at the terminals of a machine as a function of cable length and rise time of the PWM voltage pulses. In Fig. 4.14, the effect of the two afore-mentioned parameters are shown according to the simulation results of the proposed model. In next chapter, this model will be employed to investigate some approaches for the mitigation of the electrical stress on motor insulation.



**Fig. 4.14** – Simulation results: effect of cable length (left) and rise time (right) on the overvoltage and ringing at motor terminals.

#### 4.4. Publications

The research work and the results presented in this chapter have been published by the author in [86], [87].



## Chapter 5 Investigation of Possible Approaches for the Mitigation of Electrical Aging Effects

The problem of accelerated electrical aging in PWM-fed electric motors is a strong limiting factor for the exploitation of all the benefits of modern fast-switching semiconductor devices. As it has been discussed previously in this thesis, the main phenomenon that is responsible of the premature insulation degradation is the increased partial discharge activity generated due to the turn-insulation experiencing higher electric fields than those assumed as design specifications. These high electric fields, which tend to be particularly large across the weak spots of the insulation system, are proportional to the effective voltage between the turn conductors, which in turn is magnified during the propagation from the converter to the motor terminals (voltage reflection along the cable) and along the coils themselves (uneven voltage distribution). At the origin of all effects, there is the very fast slew rate of the applied voltage, resulting from the turn-off and turn-on time that the power switches take to commute.

The use of sinusoidal or  $dv/dt$  filters is the common practice for the dampening of the overvoltage at the motor terminals, especially in industry applications. However, due to the increased weight, encumbrance, and cost that the introduction of a filter implicates, and considering the performance reduction that follows, new approaches to the problem are required. This is especially true in all those applications that are strongly dependant on equipment weight and/or volume, such as aerospace and transportation in general. More promising approaches are the use of corona-resistant insulating materials and the concept of co-design. However, the increased cost of new materials is limiting their penetration in the general-purpose motor market, while co-design is not always an option due to environment or space utilization constraints. In this chapter, two possible approaches are investigated to mitigate the insulation accelerated aging. First, an innovative idea is presented that aims at introducing an active control of the aging of the electric machine based on the estimation of the progression of damage. Then, the possibility of employing multilevel converter structures is indagated by analysing the performance of a cascaded H-bridge (CHB) multilevel inverter. Both solutions are investigated through simulation employing the high-frequency electrical models proposed in the previous chapter. Additional modelling efforts required for the specific simulations are described in the section of competence.

### 5.1. Active Aging Control to Extend Drive Life Expectation

#### 5.1.1. *Structure of the proposed active aging control system*

The conceptual scheme of the proposed idea of the active aging control (AAC) is shown in Fig. 5.1. The proposed AAC system works in conjunction with the motion control of the machine to increase the overall performance and the availability of the electric machine. In motion control, the required voltage references calculated according to the load and speed requirements

(and eventually trajectory in positioning controls) are elaborated by a PWM modulator that commands the switches of the inverter to apply the desired duty cycles. In conventional drives, the commutation frequency is usually kept constant, fixed by the repetition rate of the triangular or sawtooth carrier waveform of the modulator. The slew rate of each voltage pulse is also constant, depending on the technology of the semiconductor devices, on the design of the driver circuitry, and on the selection of the dead times to avoid the short circuit of the leg. The proposed active aging control system works at a higher level with respect to the motion control regulating both the switching frequency and the turn-on and turn-off times of the power devices according to the output of the controller. The timing requirements of such a system are much more relaxed than those of the motion control, since the AAC must observe and regulate an aging phenomenon that evolves slowly with respect to the electrical quantities dynamics. The proposed AAC system is made of three main separate components: an aging estimator use the measured electrical quantities to obtain a feedback signal containing the information about insulation degradation, then a multi-objective optimization algorithm is in charge of elaborating the data and select the optimal operative condition of the inverter, finally, a set of active gate drivers regulate the switching behaviour of the power switches by controlling their turn-on and turn-off dynamics.

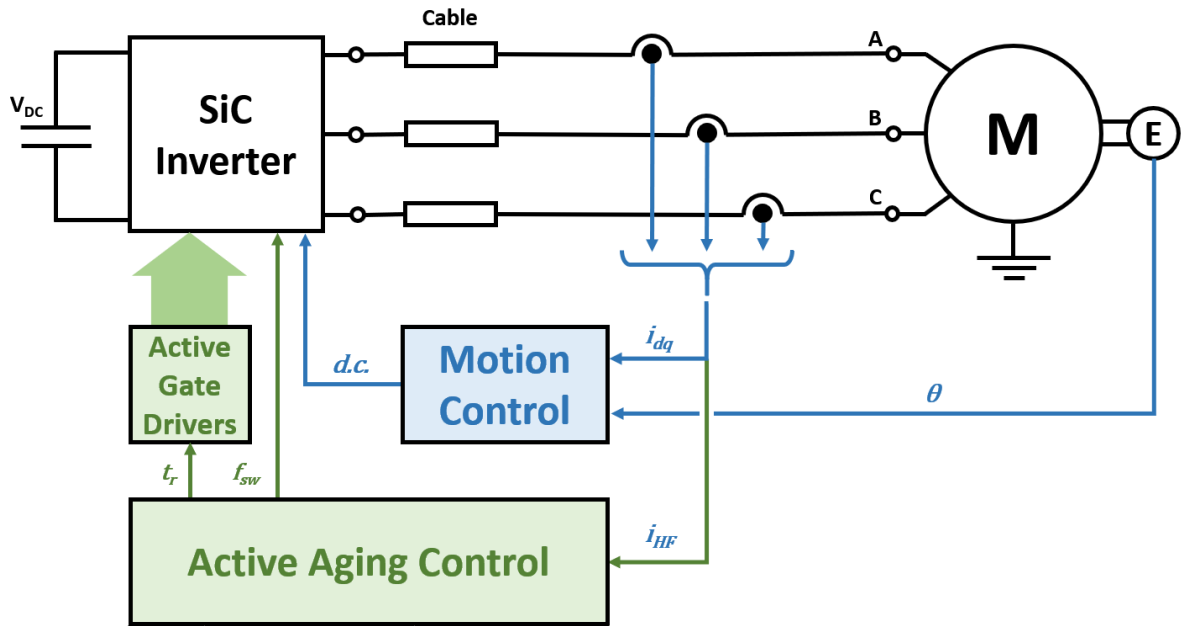


**Fig. 5.1** - Conceptual scheme of the proposed control system for the Active Aging Control.

The estimation of the aging progression can be obtained from the measurement of the phase currents acquired through the current sensors and the analog-to-digital converters (ADCs) which are normally equipped on an electric drive for motion control purposes. The use of standard sensors is important because it avoids the installation of additional dedicated equipment that would increase the weight and the cost of the system. The current measurement together with the position feedback are normally used to elaborate the motion control action

based on the operative performance requirements. On a higher level of control, the phase currents can be further processed to calculate an index that provides information about the aging state of the winding insulation system, according to what has been discussed in Chapter 3 of this thesis. The value of this index is fed to the active aging controller, together with the information related to the required operative condition of the electric drive (e.g. speed and load conditions, DC-link voltage, actual switching frequency and pulse rise time, etc.). Recalling the results discussed in previous chapters, to obtain a valid index of the winding insulation conditions, the high frequency current components must be analysed. This is because the capacitive behaviour of the motor, which depends on the structure and state of the stator winding insulation system, can only be observable from its high frequency characteristics, while at low frequency the inductive component is prominent. The high frequency information can be extrapolated from the measurement of the motor phase currents when a voltage pulse is applied at the machine terminals. This procedure only requires the machine to be stopped for a few seconds to perform the measures, without the need for expensive and delicate laboratory equipment and without disconnecting the machine. The current measured in this procedure presents a typical shape, featuring a high-frequency transient superimposed to the inductive rise that is determined by the low frequency motor behaviour and by the positive voltage pulse. Fig. 5.2 shows the voltage pulse at inverter and motor sides and the resulting phase current waveform.

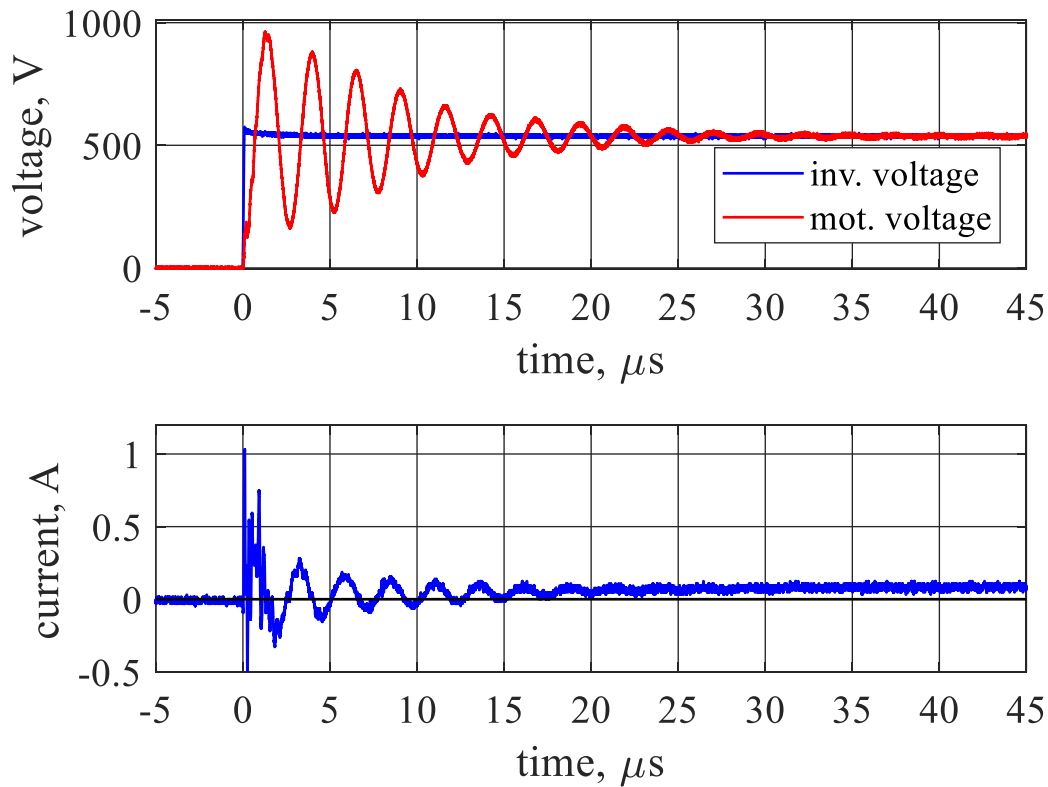


**Fig. 5.2** - Voltage waveforms at inverter and motor sides (top) and phase current showing the high-frequency transient (bottom).

The slope of the inductive rise is inversely proportional to the value of the motor inductance, thus the larger the machine the more pronounced the slope. The HF transient, which contains the desired information about the insulation state, expires in about 25-30  $\mu$ s. To improve the accuracy of the results, a higher number of samples can be acquired and then statistically elaborated to calculate an insulation state indicator (ISI) as discussed in Chapter 3. In the simulations presented in this chapter, the version of the index based on the spectrum is used, as firstly proposed by Zoeller *et al.* in [85]. The definition of the index is reported below for simplicity:

$$ISI = \text{mean}_s \left\{ \sqrt{\frac{1}{n} \sum_{k=1}^n w(k) \cdot [Y_0^{avg}(k) - Y_{j,s}(k)]^2} \right\} \quad (5.1)$$

The active aging controller has the role of analysing the data acquired from the estimator and performing a multi-objective optimization to maximize both efficiency and life duration. The AAC selects the optimal set of parameters to drive the inverter (i.e. pulse rise time and switching frequency) based on a complex algorithm which runs with a much larger sampling period with respect to that of the motion controller. The fitness functions for this complex optimization algorithm are derived taking into account both a model of the converter losses and efficiency under various operative conditions, together with the information about the aging state of the machine, given by the ISI. The mission profile required by the motion control is also considered as constraint of the optimization routine, to ensure the drive satisfies the application requirements. As a result, the AAC will improve the reliability of the drive by increasing the life expectancy of the electric machine, while reducing the overall losses.

In order to actuate such a control action elaborated by the AAC, ordinary gate drivers are not useful. In fact, this kind of driver is not able to dynamically change its performance to modify the turn-on and turn-off times of the power devices. It is thus necessary to develop a novel gate driver that is able to actively regulate the charging and discharging processes of the input parasitic capacitance, which in turn affect the steepness of the PWM pulses. Different techniques have been investigated in the literature regarding active driving [88]. The simplest way to perform the regulation of the switching behaviour of the semiconductor devices is to vary the gate resistance. This approach, however, is the most inefficient due to the direct increase of the switching losses that produces. To limit the increase of switching losses, different approaches have been proposed in the literature based on the shaping of the gate-to-source voltage: instead of instantly applying a voltage step to turn-on the device, the gate voltage is applied gradually or using a certain number of levels [89]. The higher the number of levels, the more complex the control circuit, but the higher the degree of optimization that can be achieved. In the example considered in this chapter, the details of the gate driver are neglected.

In this chapter, the idea is investigated through simulation by mean of the high-frequency models presented before. To complete the model, an analytical model has been implemented to

simulate the insulation aging mechanism, which is based on the data collected from the literature studies that have investigated the role of partial discharges on insulation degradation. Although not being accurate from a practical implementation point of view, the simulation results presented here are useful to describe the operation of the proposed idea. The realization of the final system will require more effort in developing and realize the various parts, from the estimator to the active gate driver, which will be done in future developments.

### 5.1.2. Simulation of electrical aging phenomena

The aging of the insulation system of an electric machine is a relatively slow process that can take long time to develop, from hundreds of hours to days or months of operation. On the other hand, the phenomena that cause it, i.e. partial discharges, act in the very high-frequency domain, since they depend on the switching frequency of the converter and to the very short rise times of the PWM pulses. For these reasons, a model to predict the aging behaviour of the winding insulation should be able to simulate hours of operation while running with a very short simulation time step, in the order of nanoseconds. Therefore, the simulation would take too long to complete, and the computational burden of the processor would be too large. In order to overcome this problem, a multi-time-domain model has been developed in the MATLAB/Simulink environment resorting to some simplifications for decoupling the high-frequency and the low-frequency domains. A schematic representation of the drive model that has been discussed in the previous chapter is depicted in Fig. 5.3. A three-phase equivalent circuit is used to model the inverter parasitic output impedance ( $R_{inv}$  and  $L_{inv}$ ), the cable lumped impedance ( $R_{cable}$ ,  $L_{cable}$ , and  $C_{cable}$ ) and the motor impedance. The latter impedance is modelled through the circuital representation of the transfer functions obtained by the genetic optimization routine previously described for the fitting of the motor HF model. The goodness of the agreement between the simulation results and the experimental data has been shown in the previous chapter.

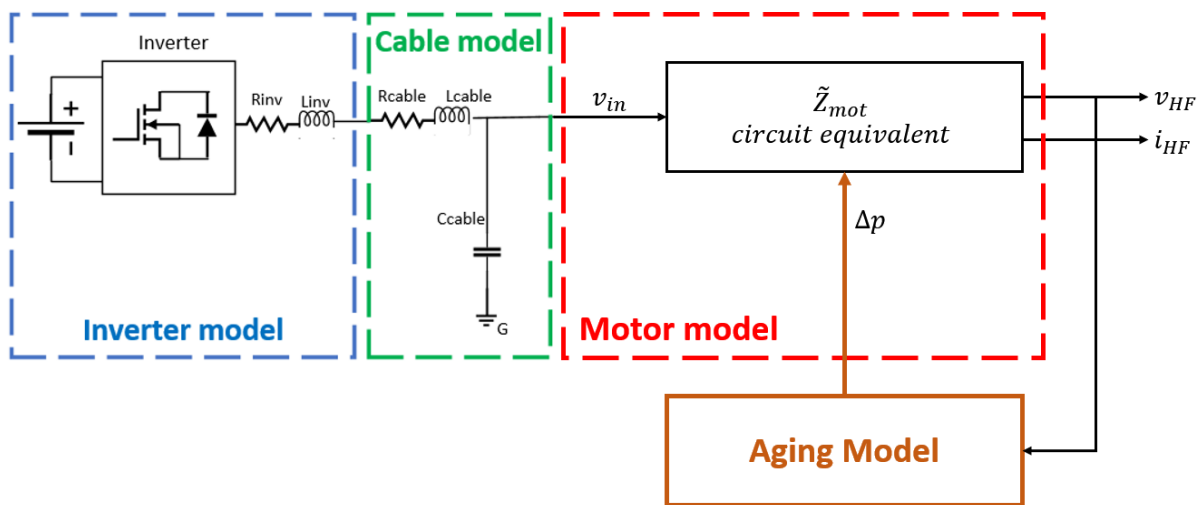
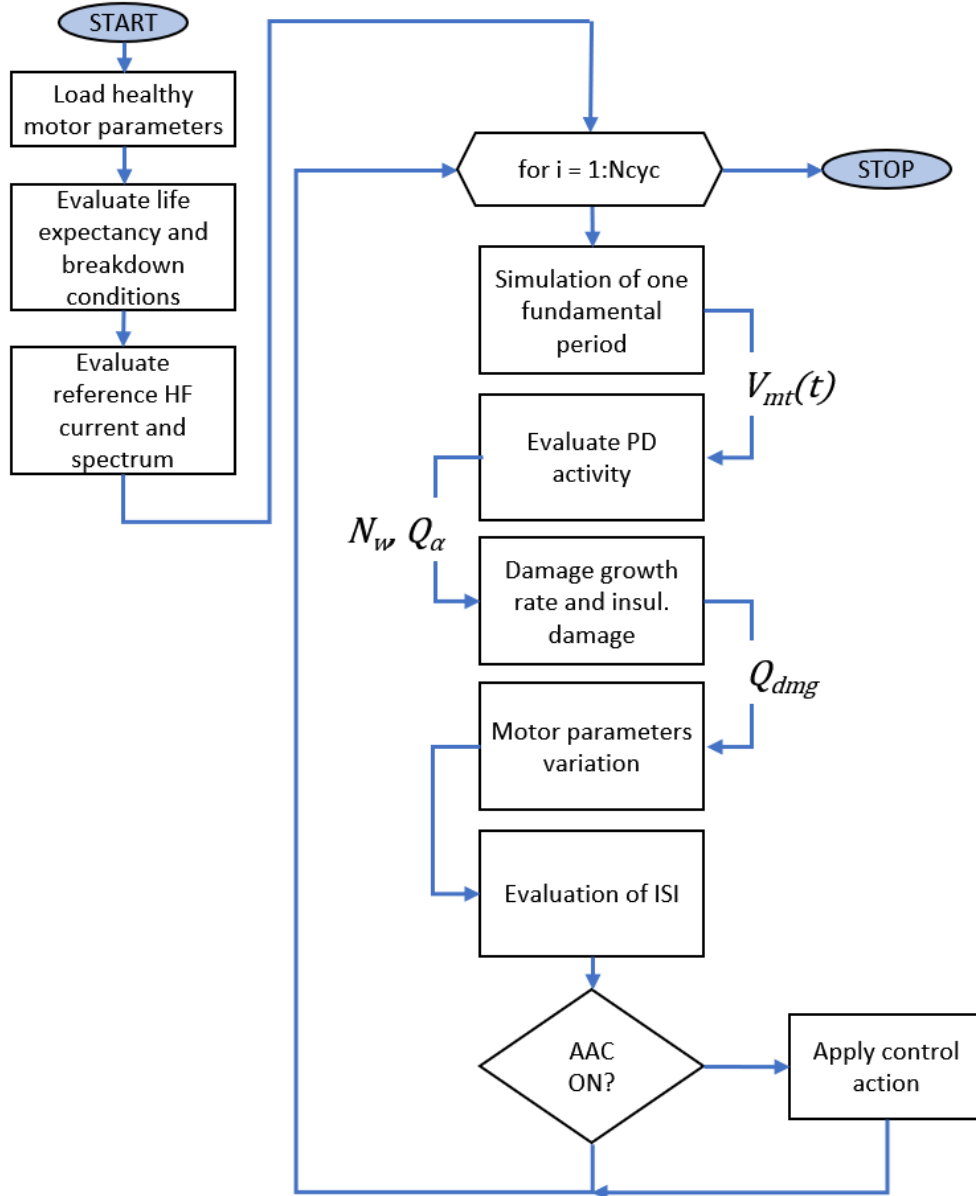


Fig. 5.3 – Schematic representation of the model employed for the simulation of electrical aging.

The drive system that has been modelled and that is used in the following analysis is the same that has been used for the accelerated aging studies presented in Chapter 3, with a SiC-MOSFET-based inverter connected to a general-purpose 370 W induction motor through a cable of 30 m. A flow chart detailing the operation of the developed model is shown in Fig. 5.4.



**Fig. 5.4** - Flow chart of the Active Aging Control simulation model.

When the simulation starts, first the model parameters corresponding to the healthy state are loaded. The simulation is carried out assuming that the total simulated time corresponds to the motor lifetime, (i.e. breakdown occurs at the end of the simulation if the control action is not active). Thus, if  $N_{cyc}$  is the number of aging cycles simulated and  $T_{cyc}$  is the duration of each cycle, the lifetime can be expressed as:

$$L = N_{cyc} T_{cyc} \quad (5.2)$$

Based on this hypothesis, it is possible to estimate the occurrence of the breakdown considering the results of the work presented by Wang *et al.* in [90]. This paper defines a Damage Growth Rate (DGR) as a quantity related to the rate of damage progression within insulation cavities caused by PD activity. This DGR is defined as:

$$DGR = N_w Q_\alpha \quad [C/s] \quad (5.3)$$

where  $N_w$  is the number of PDs occurring for each fundamental electrical period, and  $Q_\alpha$  is the scale parameter of the Weibull distribution at the 63.2% of the charge deployed by each PD event. From the data shown in this study, it is possible to derive the total charge depleted by the PDs until breakdown based on the assumed life expectancy:

$$Q_{fail} = \overline{N_w Q_\alpha} \cdot L \quad [C] \quad (5.4)$$

where  $\overline{N_w Q_\alpha}$  is the average value of DGR as evinced from the data presented in [90]. In Fig. 5.5 the average  $\overline{N_w Q_\alpha}$  values as a function of failure time are indicated according to the findings of the authors of the study. The total charge to breakdown,  $Q_{fail}$ , calculated according to (5.4), is used within the developed model to evaluate the percentage of damage caused by the PD activity during each simulated aging cycle.

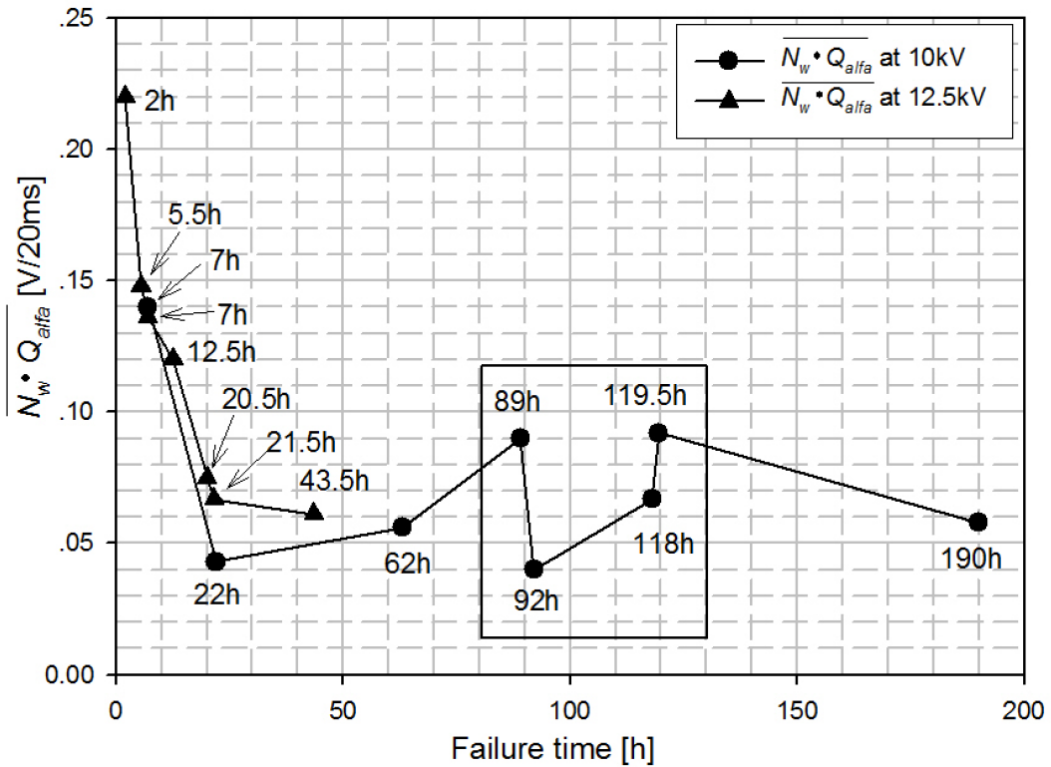


**Fig. 5.5** - Average  $\overline{N_w Q_\alpha}$  values as a function of failure time of the specimens aged at two values of the test voltage. Source: [90].

Before starting the aging cycles, the last step is to evaluate, by mean of the circuit model in Fig. 5.3, the reference high-frequency current of the healthy state of the machine. The spectrum associated to this current is lately used within the model to calculate the ISI.

Each aging cycle starts with a simulation, using the equivalent circuit in Fig. 5.3, of one fundamental electrical period under specific rise time and switching frequency. The voltage waveform at motor side is then used to evaluate the PD activity in terms of  $N_w$  and  $Q_\alpha$ . To estimate the number of PDs per fundamental period,  $N_w$ , the results highlighted about the effects of the PWM pulse characteristics on the properties of PDs that have been discussed in Chapter 2 are used. In particular, it has been found in the literature that when the pulse rise time is below 1  $\mu$ s, a single discharge develops for each voltage pulse. Additionally, the number of PD events also seems to depend on the duration of each applied voltage pulse. Based on these considerations,  $N_w$  is calculated as the number of PWM pulses for each fundamental cycle multiplied by a sigmoid function which relates the normalized number of discharges with the duration of each voltage pulse. This weighting function is obtained by fitting the data presented in [58], which are, for the sake of simplification, assumed valid also at higher frequencies with respect to those tested in the study. The magnitudes of the PD events occurring during one electrical fundamental cycle are calculated by downscaling the values of the voltage overshoots registered over the same interval. These magnitudes are distributed according to a Weibull probability function, from which the scale parameter  $Q_\alpha$  is carried out. The values of  $N_w$  and  $Q_\alpha$  calculated in this way are then used to estimate the DGR that is caused by the selected operative conditions according to (5.3). It is now possible to calculate the per unit damage caused during the considered aging step ( $Q_{dmg}$ ) with respect to the total damage to breakdown ( $Q_{fail}$ ) as in the following equation:

$$Q_{dmg} = \frac{N_w Q_\alpha \cdot T_{cyc}}{Q_{fail}} \quad [p. u.] \quad (5.5)$$

Since the electrical aging affects the high frequency behaviour of the motor, the model parameters must vary according to the progression of the damage due to the partial discharge activity. To implement this aspect, it is assumed that the overall percentage variation of the motor model parameters (indicated as  $\Delta p$  in Fig. 5.3) equals the percentage damage calculated at the considered aging cycle. Since not all the parameters vary in the same measure, each parameter variation is calculated by multiplying the percentage damage by an associated weighting factor which has been chosen based on the experimental observations made during the electrical aging campaign presented in Chapter 3.

Finally, the ISI value at the considered aging step is evaluated on the circuit model with the new aged parameters. Its value is used to calculate a proportional control action that is applied by changing the rise time of the voltage pulses, if the control action is active.



### 5.1.3. Simulation results and discussion

Using the model described in the previous section, simulation tests are carried out in order to demonstrate the validity of the proposed control technique. Fig. 5.6 and Fig. 5.7 show the results of a simulation in which the lifetime of the electric motor winding is assumed equal to 240 hours. The aging process is updated in the model at a step of 24 hours.

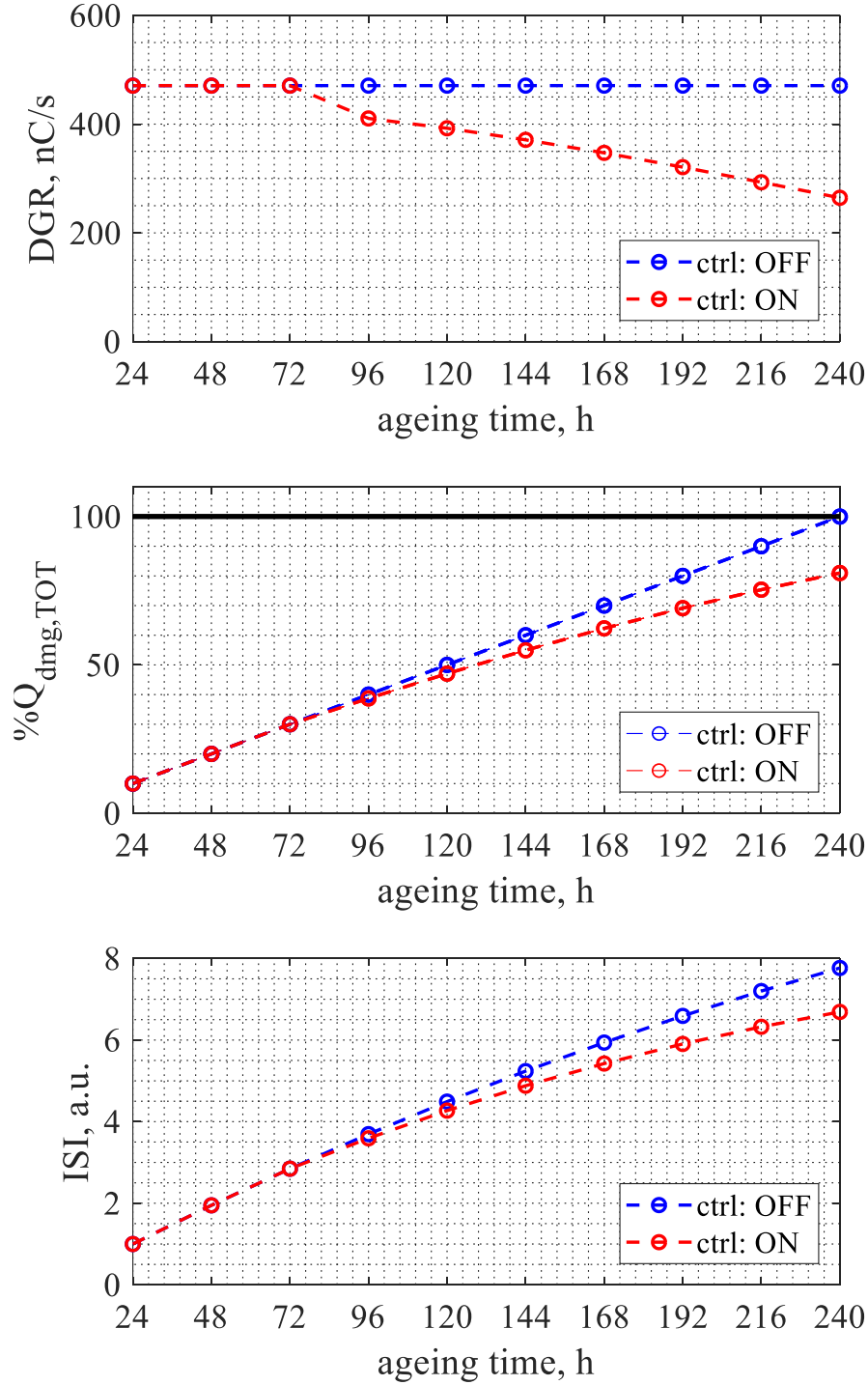


**Fig. 5.6** - Simulation results: trend of the damage growth rate (top), cumulative damage (middle), and ISI (bottom).

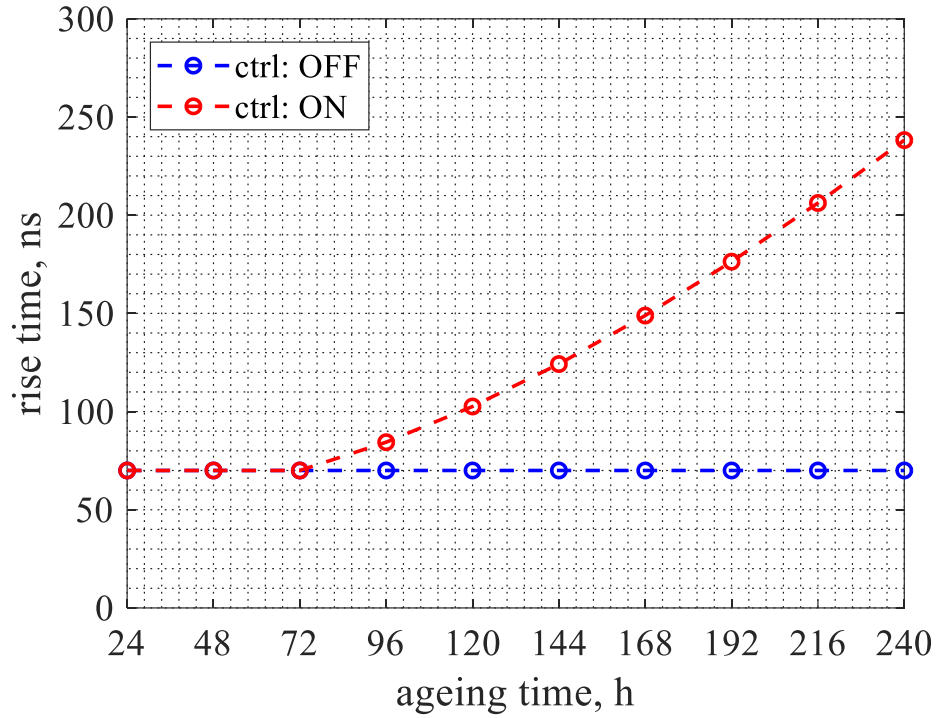


**Fig. 5.7** - Simulation results: Active Aging Control output in terms of pulse rise time.

Two cases are simulated and compared in the figures: blue lines refer to the case in which the AAC is not active, while red lines indicate the case in which the AAC is active starting after 72 hours of simulation. In the first case, the damage growth rate (Fig. 5.6, top) remains constant over the whole lifetime, this yields the cumulative damage  $Q_{dmg,\%}$  (Fig. 5.6, middle) to increase constantly until the breakdown exactly occurs after 240 hours of operation. The increasing value of the ISI (expressed in absolute units with respect to the first value, Fig. 5.6 bottom) proves that this index can detect the progressive deterioration of the winding insulation system. In the second case, when the AAC is turned on, the control action is implemented by calculating the rise time increment with respect to the initial value (set to 70 ns) as proportional to the ISI. As a result of the applied control action, the damage growth rate is progressively reduced, and the life expectancy is effectively extended (80% percent cumulative damage after 240 hours) because of the increased pulse rise time.

## 5.2. Mitigation of the Electrical Stress by Employing Multilevel Converters

In this section, a second approach is investigated for the mitigation of the overvoltage level at the terminals of high-speed drives with the purpose of extending the service life of the machine. This approach consists in employing a multilevel power electronic converter to feed the electric machine instead of a 2-level voltage-source inverter (2L-VSI), thus supplying the motor with a voltage waveform made up of multiple levels of lower amplitude each. The direct advantage of adopting this kind of approach is that the motor is subjected to a lower voltage

gradient than in the case of a 2L-VSI, so that the overvoltage level at its terminals is reduced. A 5-level cascaded H-bridge (5L-CHB) multilevel converter has been considered for the comparison in this case. This kind of converter, when operated through a Phase Shifted Sinusoidal PWM (PS-SPWM) technique, allows for optimal harmonic components cancellation up to the  $2n^{th}$  carrier multiples, being  $n$  the number of the CHB cells [91]. Therefore, other than the reduction of the stress on the insulation, a second advantage of adopting a CHB converter is that it is possible to produce the first group of voltage harmonics in the same frequency range of those produced by a standard 2-level VSI with a much lower frequency ratio between the carrier and the modulating signals [92], [93]. Consequently, at the same fundamental frequency, a 5L-CHB multilevel converter allows for lower switching frequencies compared to the standard 2L-VSI. This feature allows the use of silicon IGBTs in the CHB converter, in place of the SiC-MOSFETs that are required in the case of the VSI. Moreover, due to its intrinsic modularity, is well suited for applications that require a higher level of reliability and ease of maintenance.

With the objective of quantifying the possible advantage of employing a multilevel converter to spin high-speed machines rather than introducing new control features in the drive system to extend the service duration before maintenance, the two approaches are compared here in their overall performance. Under some assumptions to make the comparison valid, a set of simulation models are used to assess the efficiency of the two solutions and to predict the weight and volume of the final converters considering the cooling requirements. A 2-levels SiC-MOSFET-based VSI featuring active gate drivers with variable gate resistance for the  $dv/dt$  regulation and a 5-level Isi-IGBT CHB multilevel converter are modelled and analysed in the electro-thermal domain. The simulation model is built employing both the datasheet and the spice model of the selected devices, as available on manufacturer websites. Converter efficiency, volume/mass and architecture complexity are considered in the comparison, which is conducted having set the same load condition and the same voltage stress on the motor insulation for both converters.

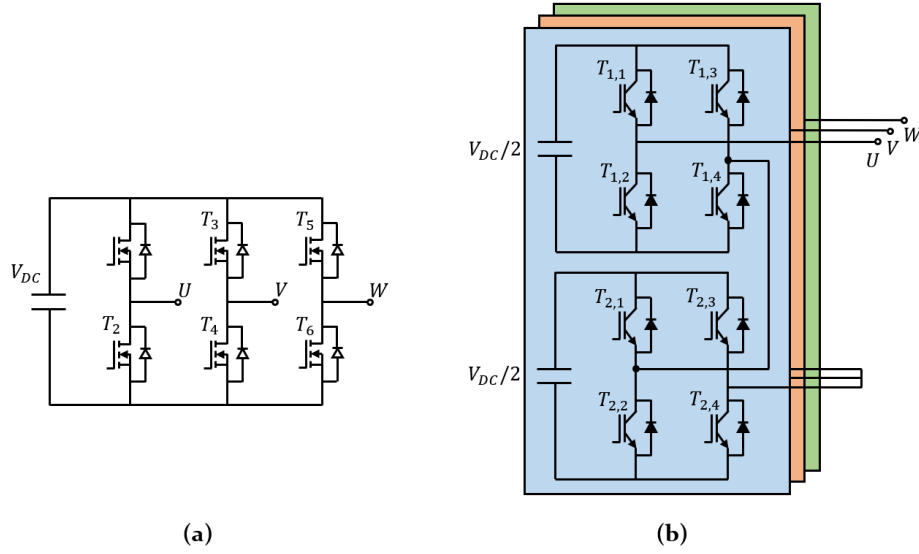


**Fig. 5.8** – Circuit schematic of the SiC-MOSFET-based 2-level VSI (a) and of the Si-IGBT-based 5-level CHB multilevel converter (b).

### 5.2.1. Hypothesis and conditions for the comparison

Here, the hypothesis that have been made and the simulation models employed for the comparison are described and discussed. Since one of the targets is the comparison of the losses and the efficiency of the converters, the first choice that is made is to assume that the motor has the same losses in both cases, so that they can be neglected from the comparison. In order to make this hypothesis, the switching frequency of the converters is selected in such a way that the Total Harmonic Distortion (THD) of the motor phase current results the same. For this step, the motor is modelled as a three-phase RL circuit with a voltage generator to simulate its back-EMF. The fundamental frequency of the machine is set to 1.6 kHz (i.e. that of a 2-pole-pair electric machine spinning at 48.000 RPM). Fig. 5.9 shows the voltage and current waveforms supplied by the converters. Both converters are driven with a sinusoidal PWM technique, employing carrier phase shift in the case of the 5L-CHB converter. With a 5-level multilevel converter, the THD of the phase current is 1% with a switching frequency of 9.6 kHz. To obtain the same THD level with the 2L-VSI, a switching frequency of 72 kHz is required. Knowing the switching frequency, the semiconductor devices are selected for the two converters. For the 2L-VSI, the SiC-MOSFETs from *Rohm SCT3022KL* are chosen, which are rated for a maximum blocking voltage of 1200 V and a nominal current of 95 A at 25 °C. For the 5L-CHB, the IGBTs from *Rohm RGVTX6TS65D* are selected, they have a blocking voltage of 650 V and a rated current at 25 °C of 144 A. Both devices are discrete components and have similar power dissipation (about 400 W at 25 °C), and a maximum junction temperature of 175 °C. The device voltage ratings are selected according to the application, since the simulations are performed with a DC-link voltage of 600 V for the VSI and of 300 V for the CHB converter.

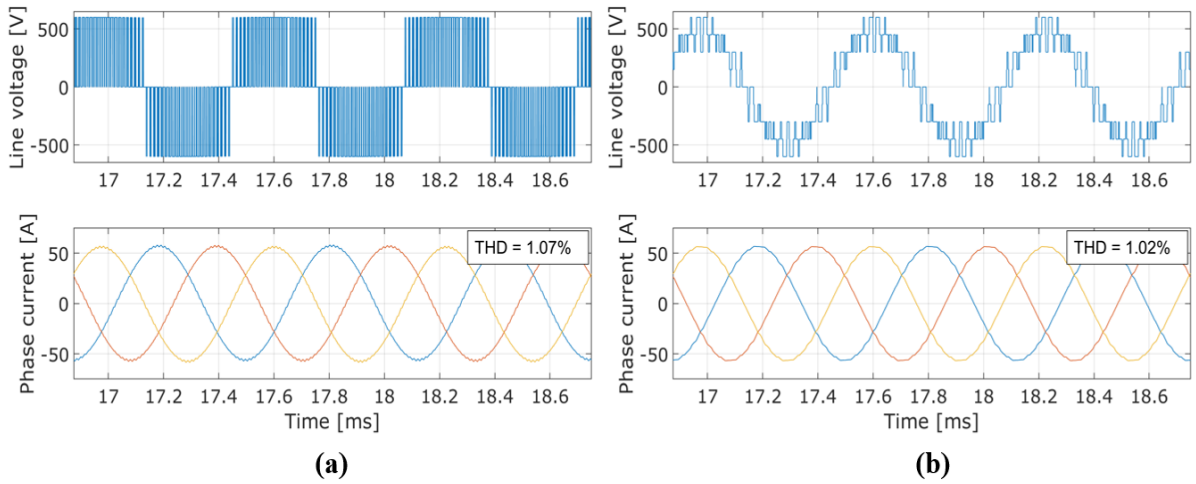


**Fig. 5.9** – Line-to-line voltage and phase currents for the SiC-MOSFET VSI (a) and for the Si-IGBT CHB multilevel converter (b).

The second hypothesis that is made is about the overvoltage level obtained at the motor terminals. In particular, the operative condition of both converters for the loss comparison is selected to achieve the same voltage overshoot. The 5L-CHB converter is taken in this case as a reference, thus selecting the gate resistor as suggested in the IGBT datasheet, 10  $\Omega$ . The gate resistance of the MOSFET drivers is chosen by slowing the switching transients down until the same level of electrical stress is reached. To this purpose, the developed high-frequency model of the electric machine that has been described in Chapter 4 is employed, together with the equivalent circuit of the converter and cable. To properly consider the effects of the switching transients of the semiconductor devices and avoid unpractical simulation times, the converters are modelled analytically as described in Chapter 4. A controlled voltage source is then used to supply the calculated waveforms to a three-phase circuit modelling the inverter output impedance, the cable and the motor in the HF domain. The analytical calculation of the voltage waveforms for the VSI has been described in the previous chapter of this thesis, an analogous model is used for the CHB, where the gate signals calculated through the PS-SPWM are four for each phase instead of two.

The values of the rise and fall times are obtained through simulation in a spice environment, adopting the manufacturer device models that are available online. To this purpose, a circuit model of a double-pulse test (DPT) has been built in the open source LT-Spice software and used to investigate the switching behaviour of the selected devices under different operative conditions. By performing the DPT with the model from the manufacturer, a set of look-up tables (LUTs) have been built giving the turn-on and turn-off times as a function of the device blocking voltage, the drain (or collector) current, the gate resistance, and the temperature. A scheme of the DPT circuit is depicted in Fig. 5.10a, where also the values of the inductances and capacitances employed for the simulation are indicated. The switching behaviour of the SiC-MOSFET at 100  $^{\circ}\text{C}$ , with 600 V blocking voltage and a drain current of 35 A is shown in Fig. 5.10b as an example.

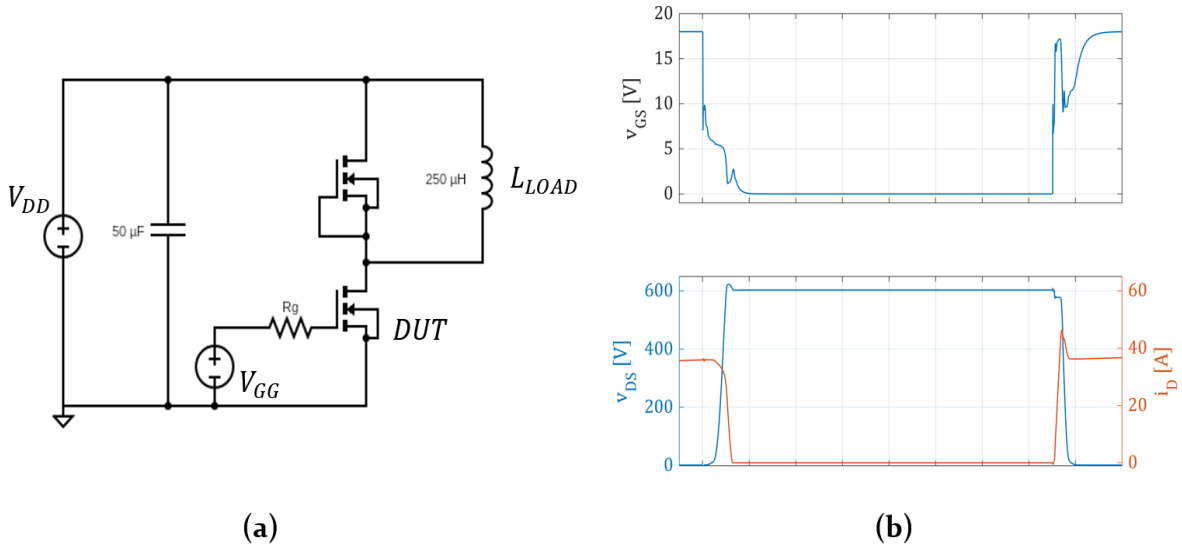


**Fig. 5.10** – Simulation circuit for the double-pulse test used for the generation of the LUTs of the SiC-MOSFET and of the IGBT models (a) and example of the turn-on and turn-off waveform for the SiC-MOSFET (b).

The switching times are calculated considering the voltage waveforms during turn-on and turn-off of the devices, according to their definition as reported in MOSFET datasheets. In particular, the rise time is defined as the time required for the drain-to-source voltage to reduce from 90% to 10% of the blocking value. Similarly, the fall time is the time during which the drain-to-source voltage goes from 10% to 90% of the blocking voltage. Fig. 5.11 shows the variation of the device switching times as a function of the gate resistance. The results obtained for the two converters employing the high-frequency model of Chapter 4 and the switching time LUTs defined as above are shown in Fig. 5.12. With a gate resistor of 10  $\Omega$ , the peak voltage at the motor terminals when using the 5L-CHB is about 40% higher than the inverter voltage. The same condition is achieved with the 2L-VSI when the gate resistance is set to 17  $\Omega$ . Furthermore, due to the different nature of the voltage waveform of the two converters, it can be seen from the figure that slowing down the commutation times is more effective in a 2L-VSI than in the 5L-CHB for the mitigation of the overvoltage.

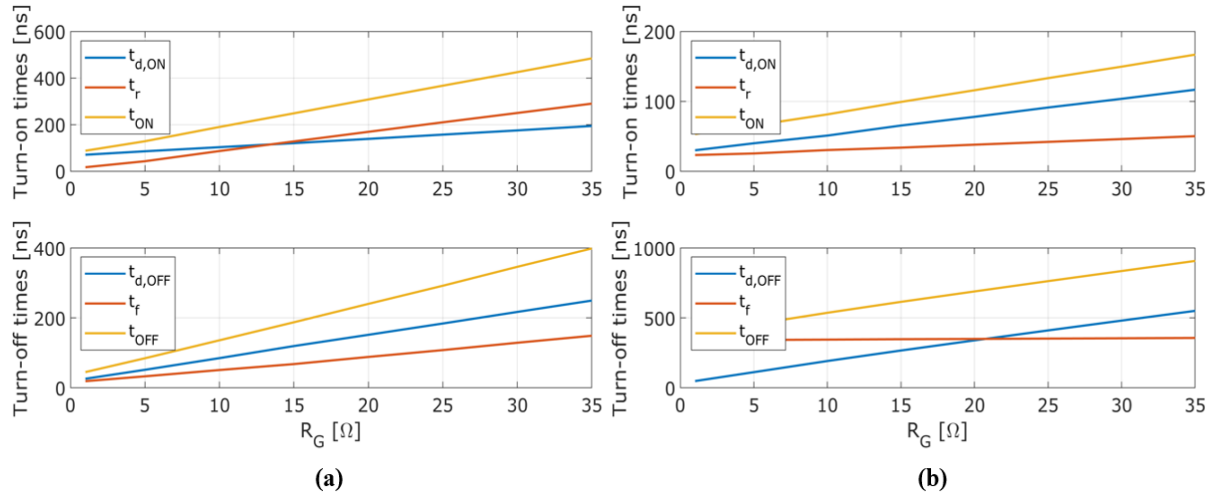


**Fig. 5.11** - Switching times of the devices as a function of the selected gate resistance: MOSFET (a), IGBT (b).

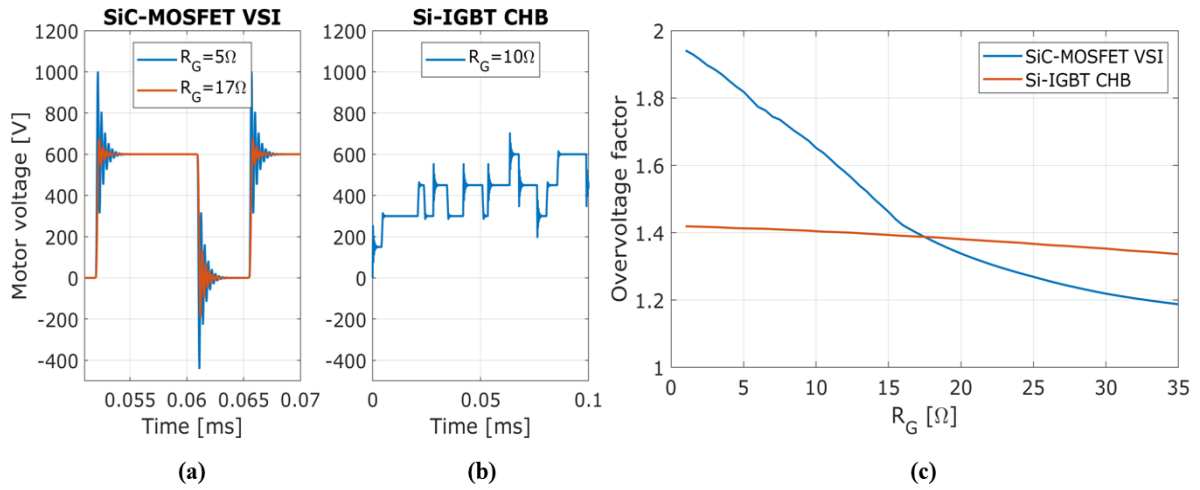


**Fig. 5.12** - Overvoltage on motor side obtained with the VSI (a) and with the CHB (b), and overvoltage factor as a function of the gate resistance compared for the two converters (c).

### 5.2.2. Loss and thermal model of the devices

The last modelling stage is building of the thermal model of the devices, which is used to evaluate the losses of the converter and to estimate the volume of the cooling system. With the previous analysis, the switching frequencies of the devices and the gate resistances for the gate drivers have been selected. The thermal model of the devices is built using the PLECS environment in conjunction with MATLAB. A series of DPTs has been performed using the spice model of the devices with the gate resistances selected at the previous stage, with the purpose of evaluating the switching energies at turn-on and turn-off at different operating points (blocking voltage and current) and at various temperature values. As a result, a second set of LUTs is obtained that constitute the device thermal descriptions in PLECS. Fig. 5.13 shows the turn-on and turn-off dissipated energy for the two considered devices.

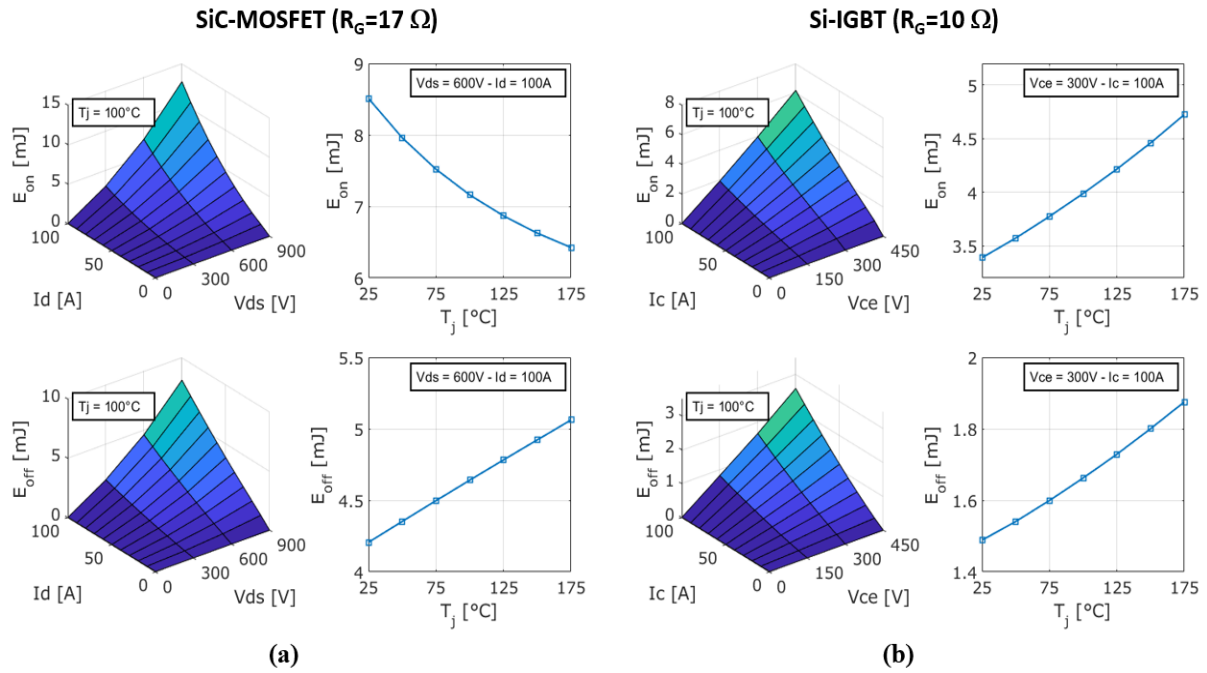


**Fig. 5.13** – Switching energy LUTs calculated from the device spice models: SiC-MOSFET with  $17\Omega$  gate resistance (a) and Si-IGBT with  $10\Omega$  gate resistance (b).

Regarding the thermal equivalent network, a three-element Cauer thermal circuit is used in the simulations to model the device behaviour from junction to case. The values for the thermal resistances and capacitances are extracted from the manufacturer thermal models and are listed in Table 5.1. Fig. 5.14 shows the equivalent thermal network of the system considering the heat sink. In the case of the 2L-VSI, a single heat sink is used to dissipate the heat produced by all the six devices, while in the case of the 5L-CHB, three heat sink are considered, one for each phase (i.e., eight devices are mounted on each heat sink). The heat sink thermal resistance has been dimensioned considering the maximum load condition of 90 A, and a maximum steady state junction temperature of  $150^\circ\text{C}$ . The selected heat sink is made of aluminium with a toothed profile, and it is designed for forced ventilation. The dimensions of the 100 mm sample are  $95 \times 40$  mm, with a specific mass of  $3.8\text{ kg/m}$ . The base thermal resistance for this sample is  $0.13\text{ K/W}$  considering an air speed of  $5\text{ m/s}$ . After selecting the required thermal resistance according to the constraints, the length of the sink is calculated accordingly, and so are its mass and volume. The thermal capacitance is calculated multiplying the total mass by the specific heat of the aluminium material, i.e.  $921\text{ J}\cdot\text{K}^{-1}\cdot\text{kg}^{-1}$ .

**Table 5.1** – Parameters of the Cauer equivalent thermal network of the devices used in the simulations.

Cauer thermal network element	SiC-MOSFET (SCT3022KL)	Si-IGBT (RGVTX6TS65D)
$R1$ [mK/W]	6.662	80.43
$R2$ [mK/W]	114.2	46.72
$R3$ [mK/W]	149.3	112.9



$C1$ [mJ/K]	1.234	1.112
$C2$ [mJ/K]	17.25	3.960
$C3$ [mJ/K]	48.56	3.962

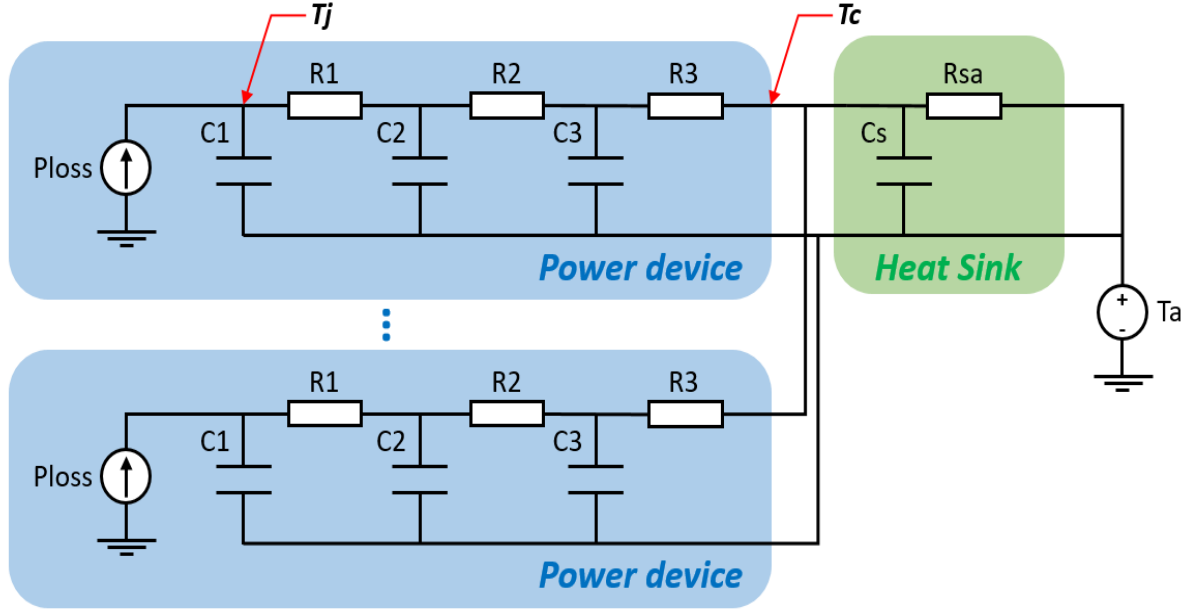


**Fig. 5.14** – Thermal network used for the simulation of the converter thermal behaviour.

### 5.2.3. Results and discussion

The conduction and switching losses of the two converters evaluated according to the model described above are shown in Fig. 5.15 as a function of the current load. As expected, in the case of the 2L-VSI the switching losses are greater than the conduction losses due to the higher switching frequency required to obtain a lower THD of the phase current. The opposite is true for the 5L-CHB because of the devices conducting for a longer time during the switching period. The conduction losses of the SiC-MOSFETs increase more than linearly for higher current values. 2L-VSI switching losses and IGBT losses have a linear trend. Despite the higher number of devices, the 5L-CHB still presents lower losses than the 2L-VSI with increased gate resistance. The efficiency as a function of the current load is depicted in Fig. 5.16. The 2L-VSI has a slightly lower efficiency than the 5L-CHB, with the difference becoming larger at higher loads. At full load, the 5L-CHB efficiency is 98.5%, while that of the VSI is 97.3%.

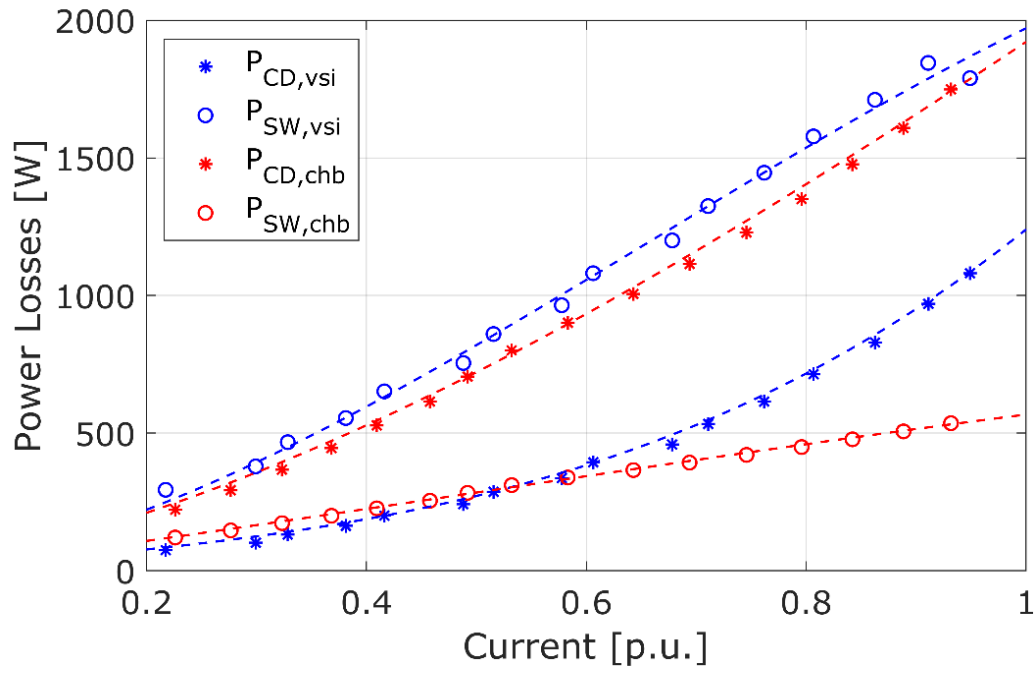


**Fig. 5.15** – Conduction (star marker) and switching losses (circle marker) of the VSI (blue lines) and of the CHB converter (red lines) as a function of the load current.

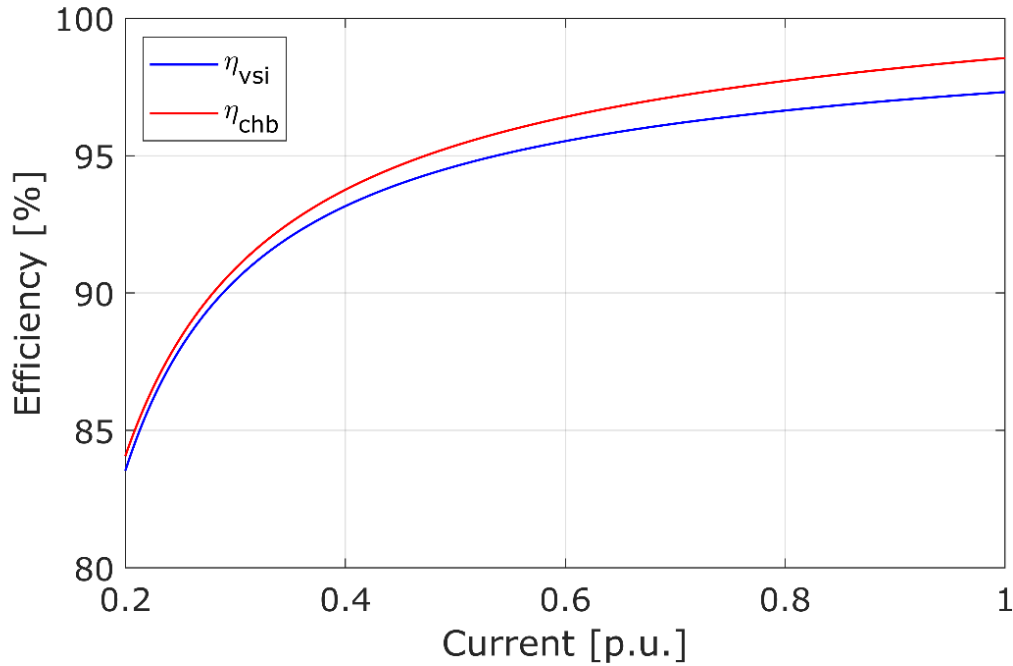


**Fig. 5.16** – Efficiency of the VSI (blue line) and of the CHB converter (red line) as a function of the load current.

Fig. 5.17 depicts the total mass of the heat sink as a function of the sink-to-ambient thermal resistance. In the figure the design point for the two converters according to the thermal dimensioning described in the previous Section are highlighted. For the 2L-VSI, a thermal resistance of 0.03 K/W is required, resulting in a heat sink mass of approximately 1.6 kg and a

volume of 1.6 l. In the case of the 5L-CHB, each one of the three heat sinks have a thermal resistance of 0.09 K/W, with a combined mass of 2.4 kg and a volume of 2.4 l. Despite the lower losses, the 5L-CHB needs a bigger dissipation system due to the higher number of required components. The high part count is the main drawback of the multilevel converter with respect to the 2L-VSI. The 5L-CHB, in fact, is made of 24 switches, which require an equal number of gate drivers to be controlled. With respect to the 2L-VSI, however, this converter can be designed with modularity in mind to increase reliability. Both the S-PWM and the PS-SPWM strategy are quite simple and easy to implement. However, speaking about control-related aspects, a 2L-VSI with switching time regulation capabilities results in a more complex implementation of both the gate driver hardware and software. The simplest implementation of the turn-on and turn-off control is the use of a variable gate resistance. Better performance can be achieved with a shaping of the gate-to-source voltage, a solution which is, however, even more complex. With the  $dv/dt$  regulation features, the efficiency of the 2L-VSI converter can be kept higher when the insulation conditions are good, and then sacrificed in favour of drive service life extension.

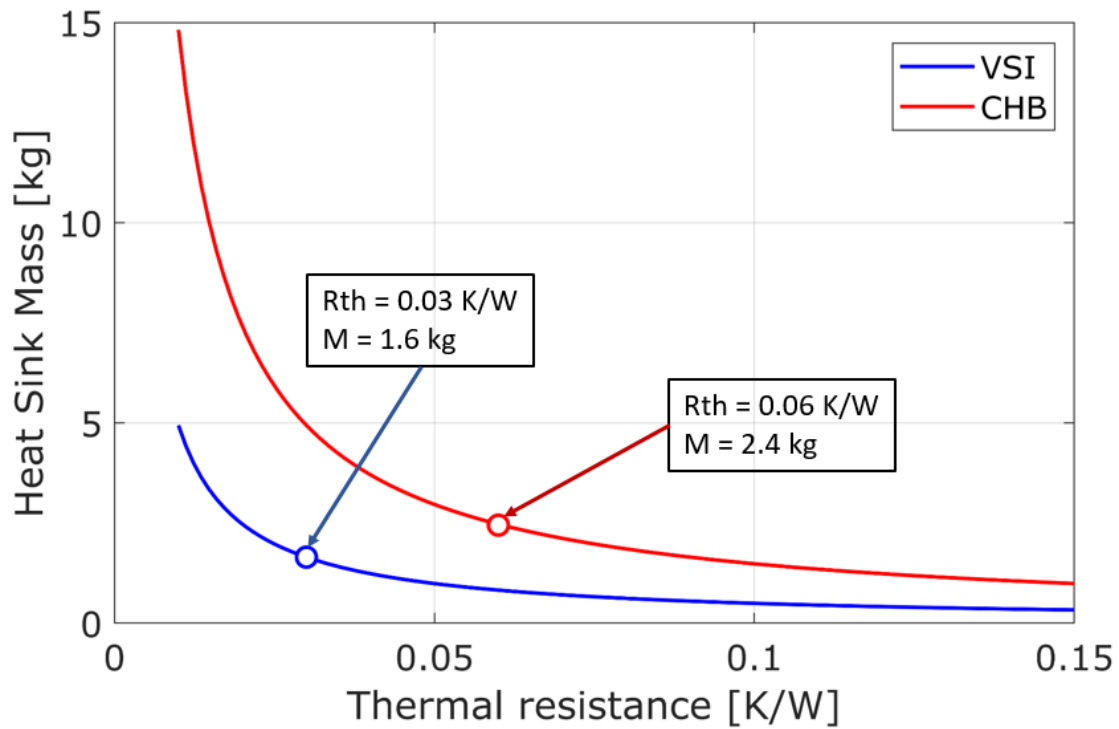


**Fig. 5.17** – Mass of the heat sink as a function of the thermal resistance between sink and ambient. The design points for the two converters are indicated as circle markers on the graph.

### 5.3. Publications

The research work and the results presented in this chapter have been published by the author in [87] and [94].

## Chapter 6 Conclusions and Future Work

In this doctoral thesis, the topic of PWM-fed electric machine insulation fast aging has been covered under various point of views. First, the main physical phenomena that are responsible for the increasing of the electrical stress on the winding insulation system have been reviewed, showing how the impact of modern fast-switching wide bandgap devices is increasing the risk of motor early failure due to partial discharges. Furthermore, some of the most common solutions for the mitigation of transient overvoltage at motor side have been discussed, highlighting their advantages and drawbacks for some particularly critical application areas.

The doctoral research that has been carried over the past years has been devoted to two main goals. The first objective has been the understanding of the observable phenomena and effects that lead to the insulation aging progression, to the twofold purpose of developing a reliable and easy-to-implement aging estimation method and of developing a set of accurate models for the simulation of the high-frequency phenomena occurring in the winding. The second goal of this doctoral work has been investigating the novel concept of actively regulating the converter switching behaviour to the purpose of mitigating the stressing phenomena and thus slowing down the aging of the insulation system. The results that have been obtaining during the last years have been presented and discussed on the main body of this thesis.

The study on the observable effects of aging has been detailed in Chapter 3, where three methods have been compared for the insulation diagnosis showing comparable performance in the estimation. The results of this study have highlighted the randomness in the electrical aging phenomenon. In fact, differently from what has been observed in other studies about the thermal effects where a clear monotonic trend can usually be distinguished after a few hours of aging, in the case of electrical stresses the behaviour of the insulation state indicators has more variability, still showing a increasing trend in the long term. A second result that is worth highlighting is the small deviation between two consecutive aging steps that has been observed, which then pose an accuracy issue for both its practical detection and modelling. Among the three estimation approaches that have been tested, one has been found to be promising for the practical implementation of an on-line aging estimator. This method is based on the measure of the high-frequency components of the motor phase current when a voltage pulse is applied to the motor. From the comparison of the high-frequency current with that previously measured in a certain moment in time chosen as the healthy point, a diagnosis of the insulation condition can be performed. The main advantage of this approach is that it can be performed on-line and with the current sensing equipment that is already part of the drive. One of the future goals in carrying on this research will be the practical implementation of such high-frequency current measuring system, since the issue of currently used sensors is the limited bandwidth with respect to the frequency content of interest for the estimation. Some preliminary simulations have been made to identify some possible techniques of signal reconstruction from multiple measures. The

results are promising, but they have not been presented in this work because they require further validation.

The development of high-accuracy simulation models of the whole drive system in the high-frequency domain that has been discussed in Chapter 4 of this thesis can be of help either during the design phase or to add advanced diagnosis features to the system. In this thesis, an innovative modelling approach for the motor high-frequency behaviour has been proposed, featuring both high fitting accuracy and low identification time with respect to other models proposed in the literature. The use of a genetic optimization algorithm, specifically designed for the automating tuning of the model by minimizing the error between measured and simulated data, greatly reduces the parameter identification time. High modelling accuracy can also be achieved by using an analytical formulation of the model, which can be helpful to consider the aging progression over time in the simulations. This analytical form can then be turned into an equivalent circuit representation and coupled with the high-frequency models of both the cable and the converter.

The last objective of the research was the development of an advanced control system for the mitigation of the overvoltage at the motor terminals based on the advancement of the insulation degradation. Due to the high number of elements required to perform such an action and to the complexity of the topic, the complete development of the active aging control system has not been fulfilled during the three years of this research. However, many steps have been taken in this direction, starting from the estimation of the insulation condition. In Chapter 5 of this thesis, the whole idea of the active aging control has been presented in all its parts: estimator, controller, and active gate drivers. Furthermore, some simulation results have been shown to investigate the possible outcomes of such a control feature. The simulations are based on the proposed high-frequency model of the drive and on a model of the aging phenomenon that has been developed recurring to both statistics presented in the literature and the data acquired during a campaign of aging tests on a group of motors. The proposed control system has been also compared with another possible solution for the mitigation of the overvoltage at the motor terminals, i.e. the use of multilevel converter topologies. In this case, a 5-level cascaded H-bridge converter has been compared with a 2-level voltage source inverter with increased gate resistance, so that the overvoltage on the motor is the same. A thermal model of the converters has been used to benchmark the losses and the efficiency in the two cases when the converters are operated in the same load conditions. The results have shown that the multilevel converter can achieve slightly better efficiency than its 2-level counterpart. However, two aspects should be pointed out. The multilevel solution requires a greater number of semiconductor devices, which reduces the reliability of the system but can increase modularity. Furthermore, the increased gate resistance in the case of an active controlled 2-level inverter is not the base operating condition, but it is only set in advanced aging conditions. Other  $dv/dt$  regulation method can also be used that have been proved to be beneficial for both losses reduction and device control. In future activities, these last aspects will be addressed in detail. The future

research will be conducted following two main paths. On the one hand, different multilevel converter topologies will be taken into consideration for the overvoltage mitigation. On the other hand, the problem of active regulation of the switching times of the devices will be addressed by designing and prototyping different active gate driver solutions that will be then compared and analysed.

## Bibliography

- [1] IPCC, 2014: *Climate Change 2014: Synthesis Report. Contribution of Working Groups I, II and III to the Fifth Assessment Report of the Intergovernmental Panel on Climate Change* [Core Writing Team, R.K. Pachauri and L.A. Meyer (eds.)]. IPCC, Geneva, Switzerland, 151 pp.
- [2] National Research Council. 2006. *Surface Temperature Reconstructions for the Last 2,000 Years*. Washington, DC: The National Academies Press.
- [3] "NASA Global Climate Change and Global Warming: Vital Signs of the Planet," National Aeronautics and Space Administration, NASA, 2008. [Online]. Available: <http://climate.nasa.gov/evidence/>
- [4] Communication from the Commission, "A Clean Planet for all A European strategic long-term vision for a prosperous, modern, competitive and climate neutral economy," 2018, COM/2018/773 final.
- [5] Report from the Commission, "2018 assessment of the progress made by Member States towards the national energy efficiency targets for 2020 and towards the implementation of the Energy Efficiency Directive as required by Article 24(3) of the Energy Efficiency Directive 2012/27/EU," 2019, COM/2019/224 final.
- [6] J. M. Carrasco, L.G. Franquelo, J.T. Bialasiewicz, E. Galvan, R.C. PortilloGuisado, M.A.M. Prats, J. I. Leon and N. M. Alfonso, "Power-electronic systems for the grid integration of renewable energy sources: a survey," in *IEEE Trans. Ind. Electron.*, vol. 53, no. 4, pp. 1002-1016, June 2006.
- [7] L. Ferreira Costa, G. De Carne, G. Buticchi and M. Liserre, "The smart transformer: a solid-state transformer tailored to provide ancillary services to the distribution grid," in *IEEE Power Electron. Mag.*, vol. 4, no. 2, pp. 56-67, June 2017.
- [8] "Key World Energy Statistics: key statistics on the supply, transformation and consumption of all major energy sources," International Energy Agency, IEA, 2016. [Online]. Available: <https://www.iea.org/statistics/kwes/consumption/>
- [9] M. Rashid, "Drives types and specifications," in *Power Electronics Handbook*, 4th ed. Oxford, UK: Elsevier, 2018, ch. 29, pp. 913-916.
- [10] *Technical Guide No. 6, Guide to Harmonics with AC drives*, ABB, 2017.
- [11] "Mobility 2030: "Meeting the challenges of sustainability," World Business Council for Sustainable Development, WBCSD, 2004. [Online]. Available: <https://www.wbcd.org/Programs/Cities-and-Mobility/Transforming-Mobility/SiMPLify/Resources/Mobility-2030-Meeting-the-challenges-to-sustainability-Executive-Summary-2004>
- [12] "Global EV outlook: understanding the electric vehicle landscape to 2020," International Energy Agency, IEA, 2013. [Online]. Available:

[https://www.iea.org/publications/freepublications/publication/GlobalEV\\_Outlook\\_2013.pdf](https://www.iea.org/publications/freepublications/publication/GlobalEV_Outlook_2013.pdf)

- [13] A. Emadi, "Transportation 2.0," in *IEEE Power Energy Mag.*, vol. 9, no. 4, pp. 18-29, July-Aug. 2011.
- [14] D. P. Tuttle and R. Baldick, "The evolution of plug-in electric vehicle-grid interactions," in *IEEE Trans. Smart Grid*, vol. 3, no. 1, pp. 500-505, March 2012.
- [15] A. Emadi, S. S. Williamson and A. Khaligh, "Power electronics intensive solutions for advanced electric, hybrid electric, and fuel cell vehicular power systems," in *IEEE Trans. on Power Electron.*, vol. 21, no. 3, pp. 567-577, May 2006.
- [16] P. Wheeler and S. Bozhko, "The more electric aircraft: technology and challenges.," in *IEEE Electrific. Mag.*, vol. 2, no. 4, pp. 6-12, Dec. 2014.
- [17] B. Sarlioglu and C. T. Morris, "More electric aircraft: review, challenges, and opportunities for commercial transport aircraft," in *IEEE Trans. Transport. Electrific.*, vol. 1, no. 1, pp. 54-64, June 2015.
- [18] W. Cao, B. C. Mecrow, G. J. Atkinson, J. W. Bennett and D. J. Atkinson, "Overview of electric motor technologies used for more electric aircraft (MEA)," in *IEEE Trans. Ind. Electron.*, vol. 59, no. 9, pp. 3523-3531, Sept. 2012.
- [19] R. R. Moghaddam, "High speed operation of electrical machines, a review on technology, benefits and challenges," 2014 IEEE *Energy Conversion Congress and Exposition (ECCE)*, Pittsburgh, PA, 2014, pp. 5539-5546.
- [20] D. Gerada, A. Mebarki, N. L. Brown, C. Gerada, A. Cavagnino and A. Boglietti, "High-speed electrical machines: technologies, trends, and developments," in *IEEE Trans. Ind. Electron.*, vol. 61, no. 6, pp. 2946-2959, June 2014.
- [21] A. Tenconi, S. Vaschetto and A. Vigliani, "Electrical machines for high-speed applications: design considerations and tradeoffs," in *IEEE Trans. Ind. Electron.*, vol. 61, no. 6, pp. 3022-3029, June 2014.
- [22] J. F. Gieras, "High speed machines," in *Advancements in Electric Machines*, 1th ed., Springer, 2008, ch. 4, pp. 81-113.
- [23] H. Kim, M. W. Degner, J. M. Guerrero, F. Briz and R. D. Lorenz, "Discrete-time current regulator design for AC machine drives," in *IEEE Trans. Ind. Appl.*, vol. 46, no. 4, pp. 1425-1435, July-Aug. 2010.
- [24] M. Rashid, "Power electronic devices," in *Power Electronics Handbook*, 4th ed. Oxford, UK: Elsevier, 2018, sec. I, pp. 15-173.
- [25] J.L. Hudgins, "Wide and narrow bandgap semiconductors for power electronics: a new valuation," in *J. of Electron. Materials*, vol. 32, no. 6, pp. 471-477, June, 2003
- [26] B. Baliga, *Power Semiconductor Devices*, PWS Pub. Co., Boston, MA, 1996.
- [27] G. L. Skibinski, R. J. Kerkman and D. Schlegel, "EMI emissions of modern PWM AC drives," in *IEEE Ind. Appl. Mag.*, vol. 5, no. 6, pp. 47-80, Nov.-Dec. 1999.



- [28] D. Han, S. Li, Y. Wu, W. Choi and B. Sarlioglu, "Comparative analysis on conducted CM EMI emission of motor drives: WBG versus Si devices," in *IEEE Trans. Ind. Electron.*, vol. 64, no. 10, pp. 8353-8363, Oct. 2017.
- [29] Jih-Sheng Lai, Xudong Huang, E. Pepa, Shaotang Chen and T. W. Nehl, "Inverter EMI modeling and simulation methodologies," in *IEEE Trans. Ind. Electron.*, vol. 53, no. 3, pp. 736-744, June 2006.
- [30] H. Akagi and T. Shimizu, "Attenuation of conducted EMI emissions from an inverter-driven motor," in *IEEE Trans. Power Electron.*, vol. 23, no. 1, pp. 282-290, Jan. 2008.
- [31] J. M. Erdman, R. J. Kerkman, D. W. Schlegel and G. L. Skibinski, "Effect of PWM inverters on AC motor bearing currents and shaft voltages," in *IEEE Trans. Ind. Appl.*, vol. 32, no. 2, pp. 250-259, March-April 1996.
- [32] O. Magdun and A. Binder, "High-frequency induction machine modeling for common mode current and bearing voltage calculation," in *IEEE Trans. Ind. Appl.*, vol. 50, no. 3, pp. 1780-1790, May-June 2014.
- [33] A. Binder and A. Muetze, "Scaling effects of inverter-induced bearing currents in AC machines," in *IEEE Trans. Ind. Appl.*, vol. 44, no. 3, pp. 769-776, May-June 2008.
- [34] G. C. Stone, I. Culbert, E. A. Boulter, and H. Dhirani, *Electrical Insulation for Rotating Machines: Design, Evaluation, Aging, Testing, and Repair*, 2nd ed. Hoboken, New Jersey: Wiley, 2014.
- [35] B. K. Gupta, B. A. Lloyd, G. C. Stone, D. K. Sharma, N. E. Nilsson and J. P. Fitzgerald, "Turn insulation capability of large AC motors. Part 3 - Insulation coordination," in *IEEE Power Eng. Rev.*, vol. PER-7, no. 12, pp. 43-44, Dec. 1987.
- [36] S. B. Warder, E. Friedlander and A. N. Arman, "The influence of rectifier harmonics in a railway system on the dielectric stability of 33-kV cables," in *Proc. of the IEE - Part II: Power Engineering*, vol. 98, no. 63, pp. 399-411, June 1951.
- [37] E. Persson, "Transient effects in application of PWM inverters to induction motors," in *IEEE Trans. Ind. Appl.*, vol. 28, no. 5, pp. 1095-1101, Sept.-Oct. 1992.
- [38] A. Cavallini, D. Fabiani and G. C. Montanari, "Power electronics and electrical insulation systems - Part I: Phenomenology overview," in *IEEE Elect. Insul. Mag.*, vol. 26, no. 3, pp. 7-15, May-June 2010.
- [39] G. Stone, S. Campbell and S. Tetreault, "Inverter-fed drives: which motor stators are at risk?," in *IEEE Ind. Appl. Mag.*, vol. 6, no. 5, pp. 17-22, Sept.-Oct. 2000.
- [40] M. Melfi, A. M. J. Sung, S. Bell and G. L. Skibinski, "Effect of surge voltage risetime on the insulation of low-voltage machines fed by PWM converters," in *IEEE Trans. Ind. Appl.*, vol. 34, no. 4, pp. 766-775, July-Aug. 1998.
- [41] B. Taghia, B. Cougo, H. Piquet, D. Malec, A. Belinger, and J.P. Carayon, "Overvoltage at motor terminals in SiC-based PWM drives," in *ELECTRIMACS 2017, International Conference on Modeling and Simulation of Electric Machines, Converters and Systems (IMACS TC 1)*, vol. 158, pp. 264-280, Apr. 2019.

- [42] A. Binder, "High frequency effects in inverter-fed AC electric machinery," in *2016 XXII International Conference on Electrical Machines (ICEM)*, Lausanne, Switzerland, Sept. 2016.
- [43] R. J. Kerkman, D. Leggate and G. L. Skibinski, "Interaction of drive modulation and cable parameters on AC motor transients," in *IEEE Trans. Ind. Appl.*, vol. 33, no. 3, pp. 722-731, May-June 1997.
- [44] C. Petrarca, A. Maffucci, V. Tucci and M. Vitelli, "Analysis of the voltage distribution in a motor stator winding subjected to steep-fronted surge voltages by means of a multiconductor lossy transmission line model," in *IEEE Trans. Energy Convers.*, vol. 19, no. 1, pp. 7-17, March 2004.
- [45] L. Niemeyer, "A generalized approach to partial discharge modeling," in *IEEE Trans. Dielectr. Electr. Insul.*, vol. 2, no. 4, pp. 510-528, Aug. 1995.
- [46] F. Gutfleisch and L. Niemeyer, "Measurement and simulation of PD in epoxy voids," in *IEEE Trans. Dielectr. Electr. Insul.*, vol. 2, no. 5, pp. 729-743, Oct. 1995.
- [47] G. C. Montanari, "Bringing an insulation to failure: The role of space charge," *2010 Annual Report Conference on Electrical Insulation and Dielectric Phenomena*, West Lafayette, IN, 2010, pp. 1-25.
- [48] *Rotating Electric Machines - Part 18-41: Qualification and Type Tests for Type I Electrical Insulation Systems Used in Rotating Electrical Machines Fed from Voltage Converters*, IEC 60034-18-41 -TS Ed. 1.0, 2007.
- [49] *Electrical Insulation Systems-Electrical Stressed Produced by Repetitive Impulses - Part 1: General Method of Evaluation of Electrical Endurance*, IEC 62068-1-Ed.1.0, 2003.
- [50] D. Fabiani, A. Cavallini and G. C. Montanari, "A UHF technique for advanced PD measurements on inverter-fed motors," in *IEEE Trans. Power Electron.*, vol. 23, no. 5, pp. 2546-2556, Sept. 2008.
- [51] P. Wang, A. Cavallini, G. C. Montanari and G. Wu, "Effect of rise time on PD pulse features under repetitive square wave voltages," in *IEEE Trans. Dielectr. Electr. Insul.*, vol. 20, no. 1, pp. 245-254, February 2013.
- [52] A. Rodrigo Mor, L.C. Castro Heredia, D.A. Harmsen, F.A. Muñoz, "A new design of a test platform for testing multiple partial discharge sources," in *Electr. Power Energy Syst.*, vol. 94, pp. 374-384, 2018.
- [53] M. Kaufhold, G. Borner, M. Eberhardt and J. Speck, "Failure mechanism of the interturn insulation of low voltage electric machines fed by pulse-controlled inverters," in *IEEE Electr. Insul. Mag.*, vol. 12, no. 5, pp. 9-16, Sept.-Oct. 1996.
- [54] K. Fukunaga, S. Okada, S. Ohtsuka, M. Hikita and K. Kimura, "RPDIV/RPDEV characteristics of twisted-pair under repetitive bipolar impulse condition," *2007 Annual Report - Conference on Electrical Insulation and Dielectric Phenomena*, Vancouver, BC, 2007, pp. 196-199.

- [55] K. Kimura, S. Ushirone, T. Koyanagi and M. Hikita, "PDIV characteristics of twisted-pair of magnet wires with repetitive impulse voltage," in *IEEE Trans. Dielectr. Electr. Insul.*, vol. 14, no. 3, pp. 744-750, June 2007.
- [56] A. Cavallini, E. Lindell, G. C. Montanari and M. Tozzi, "Inception of partial discharges under repetitive square voltages: effect of voltage waveform and repetition rate on PDIV and RPDIV," 2010 Annual Report Conference on Electrical Insulation and Dielectric Phenomena, West Lafayette, IN, 2010, pp. 1-4.
- [57] P. Wang and A. Cavallini, "The influence of repetitive square wave voltage parameters on PD statistical features," 2013 Annual Report Conference on Electrical Insulation and Dielectric Phenomena, Shenzhen, 2013, pp. 1282-1285.
- [58] P. Wang, A. Cavallini and G. C. Montanari, "The influence of repetitive square wave voltage parameters on enameled wire endurance," in *IEEE Trans. Dielectr. Electr. Insul.*, vol. 21, no. 3, pp. 1276-1284, June 2014.
- [59] P. Wang, A. Cavallini and G. C. Montanari, "The influence of square wave voltage duty cycle on PD behavior," 2015 IEEE Conference on Electrical Insulation and Dielectric Phenomena (CEIDP), Ann Arbor, MI, 2015, pp. 338-341.
- [60] P. Wang, A. Cavallini and G. C. Montanari, "Characteristics of PD under square wave voltages and their influence on motor insulation endurance," in *IEEE Trans. Dielectr. Electr. Insul.*, vol. 22, no. 6, pp. 3079-3086, December 2015.
- [61] G. Dong, T. Liu, M. Zhang, Q. Li and Z. Wang, "Effect of voltage waveform on partial discharge characteristics and insulation life," 2018 12th International Conference on the Properties and Applications of Dielectric Materials (ICPADM), Xi'an, 2018, pp. 144-147.
- [62] K. Wu, T. Okamoto and Y. Suzuoki, "Transition of Partial Discharge Behavior with Aging under Square-wave AC Voltage," 2006 IEEE 8th International Conference on Properties & applications of Dielectric Materials, Bali, 2006, pp. 36-39.
- [63] R. Bartnikas and J. P. Novak, "Effect of overvoltage on the risetime and amplitude of PD pulses," in *IEEE Trans. Dielectr. Electr. Insul.*, vol. 2, no. 4, pp. 557-566, Aug. 1995.
- [64] Y. Shakweh and P. Aufleger, "Multi-megawatt, medium voltage, PWM, voltage source, sine-wave-output converter for industrial drive applications," 1998 Seventh International Conference on Power Electronics and Variable Speed Drives (IEE Conf. Publ. No. 456), London, UK, 1998, pp. 632-637.
- [65] C. Hudon, N. Amyot and J. Jean, "Long term behavior of corona resistant insulation compared to standard insulation of magnet wire," Conference Record of the 2000 IEEE International Symposium on Electrical Insulation (Cat. No.00CH37075), Anaheim, CA, USA, 2000, pp. 13-16.
- [66] M. Kaufhold, H. Auinger, M. Berth, J. Speck, and M. Eberhardt, "Electrical stress and failure mechanism of the winding insulation in PWM-inverter-fed low-voltage induction motors," *IEEE Trans. Ind. Electron.*, vol. 47, no. 2, pp. 396-402, Apr. 2000.

- [67] C. Zoeller, M. A. Vogelsberger, R. Fasching, W. Grubelnik, and T. M. Wolbank, "Evaluation and current-response-based identification of insulation degradation for high utilized electrical machines in railway application," *IEEE Trans. Ind. Appl.*, vol. 53, no. 3, pp. 2679-2689, May/June, 2017.
- [68] W. R. Jensen, E. G. Strangas, and S. N. Foster, "A method for online stator insulation prognosis for inverter-driven machines," *IEEE Trans. Ind. Appl.*, vol. 54, no. 6, pp. 5897-5906, Nov./Dec. 2018.
- [69] J. Yang, J. Cho, S. B. Lee, J. Yoo, and H. D. Kim, "An advanced stator winding insulation quality assessment technique for inverter-fed machines," *IEEE Trans. Ind. Appl.*, vol. 44, no. 2, pp. 555-564, Mar./Apr. 2008.
- [70] R. Leuzzi, V. G. Monopoli, L. Rovere, F. Cupertino and P. Zanchetta, "Effects of electrical ageing on winding insulation in high-speed motors: analysis and modelling," *2018 IEEE Energy Conversion Congress and Exposition (ECCE)*, Portland, OR, 2018, pp. 6886-6892.
- [71] R. Leuzzi, V. G. Monopoli, L. Rovere, F. Cupertino and P. Zanchetta, "Analysis and detection of electrical aging effects on high-speed motor insulation," in *IEEE Trans. Ind. Appl.*
- [72] M. Asefi and J. Nazarzadeh, "Survey on high-frequency models of PWM electric drives for shaft voltage and bearing current analysis," in *IET Electr. Syst. Transport.*, vol. 7, no. 3, pp. 179-189, Sept. 2017.
- [73] C. Bi, K. Jia, Y. Wu, L. Dong, H. Li, W. Yao, G. Liu and H. Zhang, "High-frequency electric-motor modelling for conducted CM current prediction in adjustable speed drive system," in *IET Power Electron.*, vol. 11, no. 7, pp. 1257-1265, June 2018.
- [74] A. Boglietti, A. Cavagnino and M. Lazzari, "Experimental high-frequency parameter identification of AC electrical motors," in *IEEE Trans. Ind. Appl.*, vol. 43, no. 1, pp. 23-29, Jan./Feb. 2007.
- [75] G. Vidmar and D. Miljavec, "A universal high-frequency three-phase electric-motor model suitable for the delta- and star-winding connections," in *IEEE Trans. Power Electron.*, vol. 30, no. 8, pp. 4365-4376, Aug. 2015.
- [76] M. Degano, P. Zanchetta, L. Empringham, E. Lavopa and J. Clare, "HF induction motor modeling using automated experimental impedance measurement matching," in *IEEE Trans. Ind. Electron.*, vol. 59, no. 10, pp. 3789-3796, Oct. 2012.
- [77] J. Sun and L. Xing, "Parameterization of three-phase electric machine models for EMI simulation," in *IEEE Trans. Power Electron.*, vol. 29, no. 1, pp. 36-41, Jan. 2014.
- [78] Y. Ryu, B. Park and K. J. Han, "Estimation of high-frequency parameters of AC machine from transmission line model," in *IEEE Trans. Magn.*, vol. 51, no. 3, pp. 1-4, March 2015.
- [79] H. De Gersem and A. Muetze, "Finite-element supported transmission-line models for calculating high-frequency effects in machine windings," in *IEEE Trans. Magn.*, vol. 48, no. 2, pp. 787-790, Feb. 2012.

- [80] A. Boglietti and E. Carpaneto, "Induction motor high frequency model," *Conference Record of the 1999 IEEE Industry Applications Conference. Thirty-Fourth IAS Annual Meeting (Cat. No.99CH36370)*, Phoenix, AZ, USA, 1999, pp. 1551-1558 vol.3.
- [81] A. F. Moreira, T. A. Lipo, G. Venkataramanan and S. Bernet, "High-frequency modeling for cable and induction motor overvoltage studies in long cable drives," in *IEEE Trans. Ind. Appl.*, vol. 38, no. 5, pp. 1297-1306, Sept./Oct. 2002.
- [82] G. Grandi, D. Casadei and U. Reggiani, "Common- and differential-mode HF current components in AC motors supplied by voltage source inverters," in *IEEE Trans. Power Electron.*, vol. 19, no. 1, pp. 16-24, Jan. 2004.
- [83] L. Wang, C. Ngai-Man Ho, F. Canales and J. Jatskevich, "High-Frequency modeling of the long-cable-fed induction motor drive system using TLM approach for predicting overvoltage transients," in *IEEE Trans. Power Electron.*, vol. 25, no. 10, pp. 2653-2664, Oct. 2010.
- [84] O. Magdun and A. Binder, "The high-frequency induction machine parameters and their influence on the common mode stator ground current," *2012 XXth International Conference on Electrical Machines (ICEM)*, Marseille, 2012, pp. 505-511.
- [85] C. Zoeller, M. A. Vogelsberger and T. M. Wolbank, "Assessment of insulation condition parameters of low-voltage random-wound electrical machine," *IECON 2016 - 42nd Annual Conference of the IEEE Industrial Electronics Society*, Florence, 2016, pp. 1470-1475.
- [86] Riccardo Leuzzi, Vito Giuseppe Monopoli, Francesco Cupertino, and Pericle Zanchetta, "Automated HF modelling of induction machines considering the effects of aging," *2018 IEEE Energy Conversion Congress and Exposition (ECCE)*, Baltimore, MD, 2019.
- [87] R. Leuzzi, V. G. Monopoli, F. Cupertino and P. Zanchetta, "Active ageing control of winding insulation in high-frequency electric drives," *2018 IEEE Energy Conversion Congress and Exposition (ECCE)*, Portland, OR, 2018, pp. 1-7.
- [88] Y. Lobsiger and J. W. Kolar, "Closed-Loop di/dt and dv/dt IGBT Gate Driver," in *IEEE Trans. Power Electron.*, vol. 30, no. 6, pp. 3402-3417, June 2015.
- [89] K. Miyazaki, S. Abe, M. Tsukuda, I. Omura, K. Wada, M. Takamiya and T. Sakurai, "General-purpose clocked gate driver IC with programmable 63-level drivability to optimize overshoot and energy loss in switching by a simulated annealing algorithm," in *IEEE Trans. Ind. Appl.*, vol. 53, no. 3, pp. 2350-2357, May/June 2017.
- [90] L. Wang, A. Cavallini, G. C. Montanari and L. Testa, "Evolution of pd patterns in polyethylene insulation cavities under AC voltage," in *IEEE Trans. Dielectr. Electr. Insul.*, vol. 19, no. 2, pp. 533-542, April 2012.
- [91] D. G. Holmes and T. A. Lipo, "Carrier-based PWM of multilevel inverters," in *Pulse Width Modulation for Power Converters: Principles and Practice*, IEEE Press, 2003, ch. 11, pp. 453-530.

- [92] L. D'Errico, A. Lidozzi, V. Serrao and L. Solero, "Multilevel converters for high fundamental frequency application," *2009 13th European Conference on Power Electronics and Applications*, Barcelona, 2009, pp. 1-14.
- [93] A. Tumurbaatar, S. Mochidate, K. Yamaguchi, T. Matsuda and Y. Sato, "Harmonic loss reduction in high speed motor drive systems by flying capacitor multilevel inverter," *2018 International Power Electronics Conference (IPEC-Niigata 2018 -ECCE Asia)*, Niigata, 2018, pp. 1972-1976.
- [94] Riccardo Leuzzi, Vito Giuseppe Monopoli, Francesco Cupertino, and Pericle Zanchetta, "Comparison of two possible solution for reducing over-voltages at the motor terminals in high-speed AC drives," *21st European Conference on Power Electronics and Applications (EPE)*, Genova, 2019.